Human Motor Control and the Design and Control of Backdriveable Actuators for Human-Robot Interaction

by

Dongwon Kim

A dissertation submitted in partial fulfillment
of the requirements for the degree of
Doctor of Philosophy
(Mechanical Engineering)
in The University of Michigan
2016

Doctoral Committee:

Associate Professor Brent Gillespie, Chair
Professor Diann E. Brei
Professor Jessy W. Grizzle
Associate Professor Sile M. O'Modhrain

A mistake.

PREFACE

Acknowledgements

In the end, it is time to write up acknowledgements. I am now putting a period on my PhD journey. It is definitely a good and lucky thing that I had been able to study, research and live in a fantastic environment with various people most of whom are awesome and beautiful and look like they came out of comic strips or movies. I feel like I filled part of my life with great memories with them in a comic strip for last 5 years and 5 months. But it is a regretful thing that my academic aims and dreams were unable to be achieved. I now think it as my big mistake. First, I should appreciate my advisor Professor Brent Gillespie for his advice, help and time. I many times observed his special efforts for me in getting rid of barriers on my PhD journey. As pursuing different values, we had trouble in business. But I will remember him as a great person and friend. Also, I would like to express my heart-felt gratitude to my committee, Professor O'Modhrain, Professor Grizzle and Professor Brei. Their priceless advices and comments help me design my work and my future.

I want to express my gratitude to my lab people including Bo, Jeremy, Brandon, Alex, and Xingjian for their help and words of encouragement. I especially appreciate my good partner Brandon. And I really thank Hongrae, Dongkyoung, Jongsoo, Bungjoo, Gwangmin, Stephanie, Gwangsoo, Jaeho, Byungwoo, Dongyong, Justyna, Khaled, Mooyoung, Eunsoo, and Mary and Leslie. They accompanied my PhD journey. They made it possible to start and end this journey. I would like to express my warm gratitude my parents, sisters, and their families for their constant support. They made it possible to start and end this journey as well.

My second life starts from now on.

TABLE OF CONTENTS

LIST OF FIGURES

Figure

LIST OF TABLES

Table

LIST OF ABBREVIATIONS

ANOVA Analysis of Variance

CNS Central Nervous System

OSCA Origami Structured Compliant Actuator

PD Proportional-Derivative

SD Standard Deviation

SEA Series Elastic Actuator

SRT Serial Reaction Time

TDC Time Delay Control

RT Reaction Time

ABSTRACT

Human Motor Control and the Design and Control of Backdriveable Actuators for Human-Robot Interaction

by

Dongwon Kim

The design of the control and hardware systems for a robot intended for interaction with a human user can profit from a critical analysis of the human neuromotor system and human biomechanics. The primary observation to be made about the human control and "hardware systems is that they work well together, perhaps because they were designed for each other. Despite the limited force production and elasticity of muscle, and despite slow information transmission, the sensorimotor system is adept at an impressive range of motor behaviors. In this thesis I present three explorations on the manners in which the human and hardware systems work together, hoping to inform the design of robots suitable for human-robot interaction.

First, I used the serial reaction time (SRT) task with cuing from lights and motorized keys to assess the relative contribution of visual and haptic stimuli to the formation of motor and perceptual memories. Motorized keys were used to deliver brief pulse-like displacements to the resting fingers, with the expectation that the proximity and similarity of these cues to the response motor actions (finger-activated key-presses) would strengthen the motor memory trace in particular. Error rate results demonstrate that haptic cues promote motor learning over perceptual learning.

The second exploration involves the design of an actuator specialized for human-robot interaction. Like muscle, it features series elasticity and thus displays good backdrivability. The elasticity arises from the use of a compressible fluid while hinged rigid plates are used to convert fluid power into mechanical power. I also propose impedance control with dynamics compensation to further reduce the driving-point impedance. The controller is robust to all kinds of uncertainties.

The third exploration involves human control in interaction with the environment. I propose a framework that accommodates delays and does not require an explicit model of the musculoskeletal system and environment. Instead, loads from the biomechanics and coupled environment are estimated using the relationship between the motor command and its responses. Delays inherent in sensory feedback are accommodated by taking the form of the Smith predictor. Agreements between simulation results and empirical movements suggests that the framework is viable.

CHAPTER I

Introduction

My work is focused on interaction between humans and machines that takes place across a mechanical contact. By carefully considering mechanical interactions, I hope to inform the design of computing machines that are easier to use, and robots that are suitable and safe for human interaction. I am particularly interested in robots to be applied for rehabilitating human motor skill and motor function. I also consider interaction between humans and simple objects in the environment to guide the design of robots intended for physical interaction with humans.

Interaction across a mechanical contact involves exchanges of both mechanical power and pure information between a human and machine. An important feature that is perhaps the most influential in determining the nature of interaction is the mechanical impedance of both the human and the machine (or object). As is well known in engineering design, impedance matching between the two interacting parties promotes maximum exchange of power. It also seems likely that information transfer is maximized when impedances are matched. However, most commercial robots are characterized by very high impedance. Humans have rather modest impedance by comparison. Neither a pure motion source nor a pure force source models human behavior very well. Rather, humans bend under load and behave with restoring forces when they are displaced. Note that muscles are extensible and are invariably modeled with elastic elements in series (and often also in parallel) with motive elements. It makes sense then to explore the design of robots which are impedance matched to humans. Note also that most objects designed and built for human use also feature modest impedance.

In my first body of work, I investigate the design of haptic cues that might be delivered to the fingertips from a computing machine to improve human-machine performance. The domain is in fact very narrow in that performance shall be measured in terms of pressing keys in a particular sequence. Like pressing keys on a computer

keyboard. I adopt a well-known experimental paradigm called the serial reaction time task (SRT task). This is sort of like a game of "Simon Says", where the player must reproduce a sequence of button presses on four buttons that gets ever longer, as cued by a sequence of lights in the buttons. Except in the SRT task buttons are pressed immediately after each light appears or cue is delivered. The reaction time is the chief performance metric in the SRT task rather than the length of sequence achieved as in Simon Says.

I introduce haptic cues to the SRT task, wherein the cues may be delivered as activations of motors attached to each of four keys. By design, the impedance of the motors is roughly matched to that of human fingers. Likewise, the activation of the motor coils is carefully chosen so as to produce discernable displacements in the fingers. The backdriveability of the motors and thereby the keys is also a significant design features, so that actions of the human subject can be recorded even if they potentially occur simultaneously with activations of the motor.

Haptic cues had previously been introduced in the SRT task by [1], but these were only in the form of vibrotactile cues delivered to the proximal interphalangeal region of the fingers. I hypothesize that cues delivered as displacements to the fingertips may engage more of the motor control apparatus of the human, since they also engage proprioceptors (motion sensors). Proprioceptor are naturally also engaged during motor actions and may play a significant role in motor control.

In a second body of work, I take up the topic of designing and controlling backdriveable actuators for use in robots intended for physical human-robot interaction. These include wearable robots and all sorts of human-safe robots. I take inspiration from the burgeoning field of soft robotics (soft actuators in particular), but I take a cold hard look at the field and offer something even better.

I create an actuator that does not store elastic energy but instead functions as close as possible to an ideal transformer (transforming input fluid energy into energy available for doing work on the environment). Note that the environment might be a human user that wears the robot thus actuated. It is desirable to minimize the energy stored and maximize the energy converted into action by the robot on its environment. In addition to the *design* of backdriveable actuators, I look into the *control* of such actuators, noting that control is also often a viable means to achieve backdriveability. Proportional gain realizes a virtual spring of course. But there are limitations to achieving backdriveability by control and tradeoffs between achieving backdriveability by physical device design and by control design. I examine these tradeoffs with an exploratory study that involves both the realization and testing of

hardware, the production of models and associated analyses, and the undertaking of simulation studies.

Finally in my last body of work, I turn the problem around and look at human motor control. Obviously the actuators are already built and deployed and do not require design. But note that muscles are backdriveable. The features of series elasticity that imbue all of my work are also features of biological muscle, interestingly. I take up the topic of whether human motor control is model-based or perhaps model-free. There has been significant controversy in the field of human motor behavior regarding the question of internal models. At the moment model-based control that is known generally in the motor control literature as internal models is very popular. The internal model is the prevailing hypothesis and prevailing explanation for human motor behavior. But I offer an alternative that is in fact completely model-free. However, the challenge in any model-free approach is that feedback must sustain delays that are physiologically realistic, that is on the order of 30-100 ms.

The contributions of this thesis are summarized as follows:

1. Effect of Haptic Cues on the Human Motor System

- Demonstrates implicit learning with haptic cues applied to fingertips
- Shows error rates are improved with haptic cues over visual cues, suggesting motor learning rather than perceptual learning.

2. Design and Control of Backdriveable Actuators

- Shows parallels between SEA and fluidic actuators, including options for control.
- Designs and demonstrates a new actuator that minimizes storage of elastic energy and harnesses singularity to advantage
- Develops controllers that promote backdriveability

3. Computational Model of Human Motor Control

- Proposes a computational model that the relationship between the motor command and its responses in place of internal models
- Demonstrates the reproducibility of the proposed model in the human's fast movements

CHAPTER II

Effect of Haptic Cues on the Human Motor System

Motor learning, especially in its latter phases, often takes place without dedicated attention and without awareness for either the process or the content of what is learned. Fitts and Posner called this phase of motor learning autonomous [33]. Implicit learning describes not just motor but any type of learning, and is similarly characterized by a lack of awareness for the process or the content of what is learned [16, 93]. Implicit learning is often studied using the serial reaction time (SRT) task, which was introduced by Nissen and Bullemer (1987) [86]. In the SRT task, participants respond to stimuli presented in one of four locations by pressing a corresponding key. When a repeating sequence of stimuli structured according to certain rules is presented unbeknownst to participants, reaction times (RTs) and error rates decrease with practice. If the stimuli later appear randomly, the participants do not respond as quickly. Participants are often unaware of the existence of the structure and are unable to express the sequence, implying that learning occurred implicitly [119].

Since the SRT task involves responding with a key press, a portion of RT or error rate improvements may be attributable to motor learning. That is, the sequence is learned in terms of a sequence of motor responses, a view termed R-R (response-to-response) learning. This view contends that the motor systems governing active movement generate a memory trace of successive motor actions. This allows participants to anticipate the next response at a given trial even without perceiving stimuli [49, 83, 118]. In this sense, R-R learning would presumably be a type of motor learning, while the alternative, S-S (stimulus-to-stimulus) learning would be a type of perceptual learning. S-S learning assumes that perceptual memory systems are involved in forming a representation for successive stimuli. Participants use

representations to predict the next stimulus in a sequence based on associations with the previous stimulus even when they are not able to thoroughly recall the sequence [31, 51] .

A fair amount of attention has been dedicated to determining whether and how motor learning and perceptual learning contribute differently to obtaining sequence knowledge in the SRT task [8, 39, 45, 84]. These studies have been performed with a variety of experimental paradigms in an attempt to disentangle the motor and perceptual contributions [48, 95, 118]. Most of these studies have, however, been undertaken exclusively using visual stimuli [76,118]; only a few studies have explored sequence learning using other stimulus modalities [1, 126].

A stimulus modality of particular value in the development of motor skills is the haptic modality. Haptic cues invariably accompany motor actions that involve contact with objects in the environment. Even non-contact motor tasks involve proprioceptive, skin stretch, and inertial force cues. Especially for motor skills that involve sequenced actions, an accompanying sequence of haptic cues might be involved in the development and retention of motor skills. Such cues can signal the successful completion of a motor action. For example, the detent or click-feel and subsequent bedding of a key on a computer keyboard together signal completion of a keypress and possibly play a role in the development of chunked keying sequences.

A number of computer-assisted motor training environments based on haptic technology have been created, hoping to leverage the role of haptic stimuli in motor learning [3, 32, 40, 43, 58, 71, 74, 87, 97, 112] . The idea is to synthesize the appropriate haptic cues using a motorized device and potentially to automate the role of another human who provides manual guidance. Results have been mixed in many studies, but a few studies have demonstrated the benefit of automated guidance for mastering motor skills, especially the studies of [15, 20, 32].

Motivated by these studies, and hoping to introduce some rigor into research involving haptic devices for motor learning, I introduce haptic stimuli to the SRT task. In particular, I introduce haptic cues that produce motion in the fingers. By back-driving the tendons and joints of the fingers, which are associated with kinesthetic receptors, haptic stimuli could enhance motor memory based on their association with the excitation of similar kinesthetic cues that occur during the response key presses. Consequently, it would be expected that a SRT task using haptic stimuli could show enhanced motor-based learning relative to a SRT task using visual stimuli. The vibrotactile stimulus introduced in [1] could also be regarded as a haptic stimulus, but is different in that cues of small amplitude, high frequency (200 Hz) vibration

are presented to the skin on the proximal phalanx of a finger. Note that the haptic stimuli developed in the study present trigger significant movement of the tendons, muscles, and joints in addition to the skin of the fingers.

In this chapter, the main objective is to investigate how haptic cues contribute to the balance of motor and perceptual learning. I adopt the SRT protocol developed by Willingham in [118] to distinguish motor and perceptual components of learning, adding haptic cues alongside the standard visual cues. Many variants of the SRT task have been developed to eliminate certain effects and to even more finely distinguish types of motor learning. In particular, the learning of the correct answer button sequence in the egocentric space (response-based learning) can be distinguished from learning of the finger movement patterns (effector-based learning; e.g., Willingham et al. [120]), Willingham, Willingham et al., and Witt and Willingham showed that sequence knowledge can pertain to sequences of response location [118,120,122], whereas Park and Shea, Bapi et al., Verwey and Wright, and Verwey and Clegg demonstrated the existence of an effector-specific component in sequence learning [4, 88, 116, 117]. However, Deroost et al. and Berner and Hoffmann suggested the contributions of effector-independent (response location) and effector-specific acquisitions to learning can coexist [10, 22]. The contribution of eye movements, termed oculomotor learning, is another type of motor learning. Gheysen et al. and Nemeth et al. devised modified versions of Willingham's SRT design by presenting stimuli at only one location to eliminate the participation of oculomotor learning [39, 84]. In the present study I do not attempt to distinguish effector specific learning and response location learning. I also do not attempt to eliminate oculomotor learning as the co-location of stimuli in the haptic case would involve the coding (and de-coding by our participants) of information in time rather than space. I am interested in a presentation of haptic stimuli that is most natural and ecologically meaningful in the context of the button-pressing task.

In Willingham's protocol, participants perform a SRT task in an incompatible mapping for the training phase and in a compatible mapping for the transfer phase. In the incompatible mapping, participants are asked to press one key to the right of the stimulus (shifted right). If the stimulus was on the far right, participants press the key on the far left (wrapping around). In the compatible mapping, there is a direct spatial correspondence between each stimulus and key. To see whether participants learning is oriented to stimulus-based or response-based sequences, this study investigate transfer to the compatible mapping (without shift) in the following two conditions. In the perceptual condition, the transfer stimulus sequence is identical

to that used during training [but participants would press different keys due to the change from incompatible (shifted) to compatible (unshifted) mapping]. Whereas in the motor condition, the stimulus sequence is shifted left so that response sequences are identical to those in the training phase. Willingham reported better transfer in the motor group compared to the perceptual group, suggesting that participants learn sequences at the motor response level [118]. In contrast to the Willingham's study, which investigated whether perceptual or motor learning is predominant in visual stimuli, the present study focuses on determining whether one modality (haptics or vision) would better facilitate motor learning than perceptual learning. It is expected that the haptic modality is more closely tied to the motor system and would thus favor motor learning.

2.0.1 Materials and Methods

Participants

A total of 32 volunteers (24 male), from the University of Michigan, ranging in age from 19 to 33 years (24.28 ± 3.77 s.d.), participated in the study. All participants reported normal or corrected-to-normal vision, and no neurological or motor deficit. None of the participants had previous experience with SRT tasks and were not made aware of our hypotheses. All gave written informed consent. The experiment was approved under the University of Michigans Behavioral Sciences Institutional Review Board.

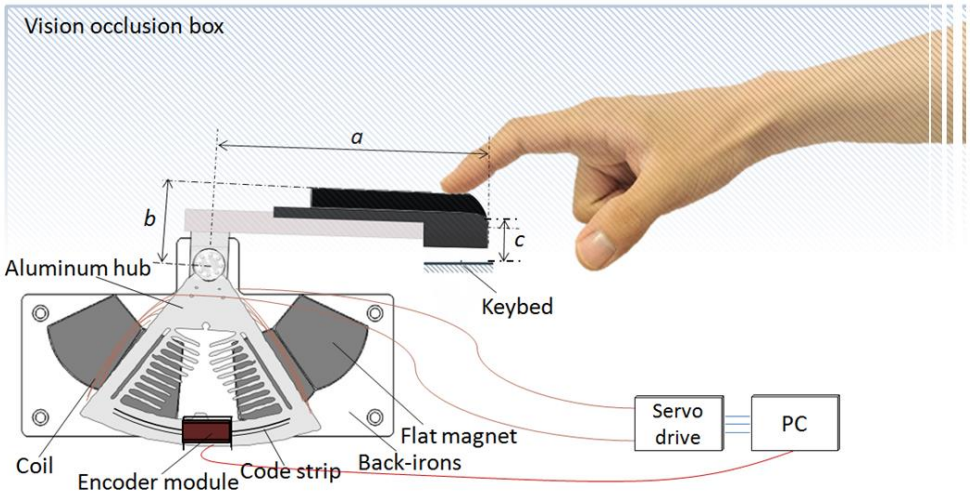

Figure 2.1: A schematic diagram of the experimental apparatus and setup.

Apparatus

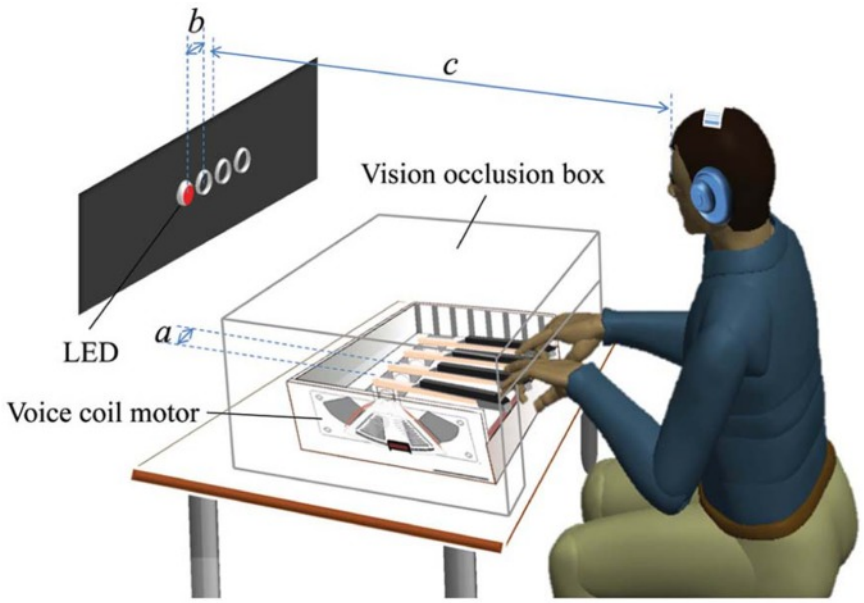

Figure 2.2: A schematic diagram of the experimental apparatus and setup. Four lever-shaped keys were motorized using flat voice coil motors (VCMs) and placed under computer control. The keys were spaced 6.5 cm centerline to centerline (a). Visual stimuli were presented by the lighting of four horizontally positioned red LEDs spaced 5 cm apart (b) and haptic stimuli were provided by the injection of an upward half-sinusoid pulse in the reference position of the key. A participant sat and rested her/his ring and index fingers of both hands on the keys. The center of the four LEDs was about 90 cm away from the participants eyes (c). She/he was allowed to adjust the height of the chair for comfort and the participants view of her/his hands was occluded using a box. White noise was presented through headphones.

A custom keyboard of four motorized keys was fabricated using a custom flat voice coil motor on each key to present the haptic cues (see Fig. 2.1). The four lever-shaped keys were motorized to present haptic stimuli using flat voice coil motors (VCMs) and instrumented to record participants responses. Every VCM consisted of two back-irons each affixed with four magnets. An aluminum hub was wrapped with 28 AWG magnet wire and this subassembly was set in bearings on a steel dowel between the two back-iron/magnet assemblies. Each key was connected to the top of an aluminum hub, and this rotary assembly had a moment of inertia of 4500 kgmm^2 about its axis of rotation. The displacement of each key was measured by an optical encoder with a resolution of 0.18 degrees. The encoder module was fixed to the bottom of a back-iron for reading a code strip attached along the bottom edge of the aluminum hub (see Fig. 2.1). Each of the VCMs was connected and powered by an Advanced Motion Controls® brushless servo drive (California, USA). The servo drives and encoders were interfaced with a Sensoray® 626 Data Acquisition board

(Oregon, USA) installed on a standard PC. Each key was 160 mm long and 48.5 mm high from the axis of rotation to its end and its top, respectively (a and b in Fig. 2.1). The travel at the tip of each key when fully depressed from the unloaded state to a physical keybed was 12 mm (c in Fig. 2.1). The four keys were equally spaced, and the distance between key centers was 65 mm (a in Fig. 2.2). The four keys were controlled by a 2.27 GHz personal computer running Windows® 7.

To indicate to participants when their responses had been registered by the computer, the mechanical behavior of each key included a detent or click-feel. This type of keyswitch provides feedback when a response is captured, and is preferred because it supports fast typing speeds and low error rates [10]. Fig. 2.3 shows the force-displacement curve programmed for each key. Let x denote the displacement of a key from its equilibrium position. The fixed displacement x_A=5 mm was defined as a threshold past which participants would have to press the key to register a response to the computer. The displacement x_A was also used to measure the reaction time (see Fig. 2.4) and define the make-force (the maximum force past which the key would break through to keybed. The force was programmed using simple proportional feedback control with gain K_1 =0.22 N/mm. The commanded force increased in proportion to the displacement x from equilibrium such that the make-force was 1 N. Once the key crossed the threshold x_A, a distinct drop in force occurred during key travel, and a constant force (0.1 N) was applied so that the key would return to the equilibrium position if released. Beyond x_B, an additional force with a higher effective stiffness (K_2 =0.6 N/mm) acted. The physical keybed was located 12 mm below the equilibrium position. Care was taken to ensure that all four keys provided the same sensation when depressed.

Stimuli to elicit participants responses in the SRT task were presented in two ways: visual and haptic. Visual stimuli were provided by the lighting of four horizontally positioned red LEDs spaced 5 cm apart (b in Fig. 2.2) against a black background situated about 90 cm from the participants eyes (c in Fig. 2.2, visual angle: 9.5 degrees). Haptic stimuli were generated by injecting an upward 100 ms half-sinusoid pulse in the reference position of the key, with an amplitude of 7 mm with respect to the tip of the key. Since proportional control was also used with the effective stiffness 0.22 N/mm for haptic stimuli, a corresponding pulse in force and an associated pulse excursion in position would be delivered to a finger.

The haptic stimuli were delivered to the index and ring fingers of both hands resting on the keys. Each finger was mapped to a key (labeled 1-4 from left to right) with the left ring finger responding on key 1, left index finger on key 2 and so on,

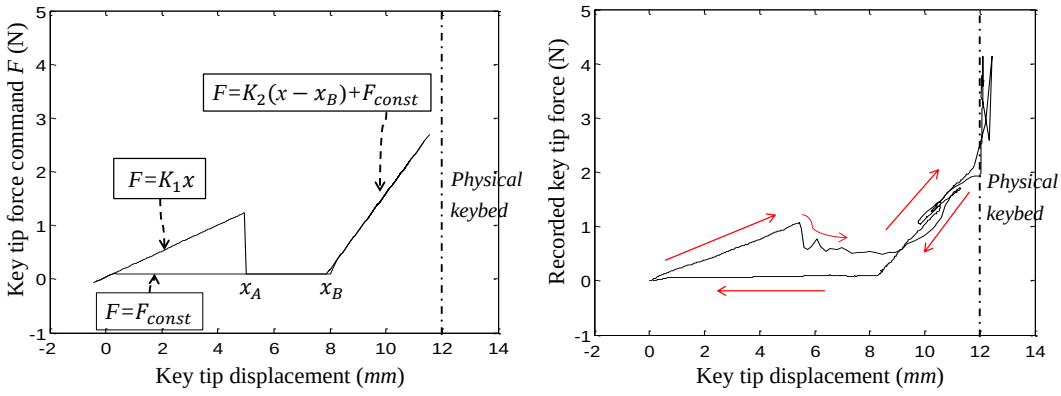

(a) (b)

```
flag =0;

while(...){
if (x > xA)
      {flag =1;}
if (x < 0)
      {flag =0;}

if (!flag)
{
   F=K1x;
}
if (flag)
{
     F=max(Fconst, K2(x − xB)+Fconst);
}
}
```

(c)

Figure 2.3: The force-displacement curve of a buckle spring keyswitch: (a) The command for force versus displacement. F and x denote the force and position at the tip of the key, where positive values for x denote downward motion of the key. Constants K_1 and K_2 denote gains for proportional feedback control, and F_{const} represents a constant force. (b) Force versus displacement recorded by a force sensor and an encoder. (c) Pseudo-code presenting the algorithm for the keyswitch. The variable flag was introduced to manage the time sequence of the key movement.

as illustrated in Fig. 2.2. We followed Abrahamse et al. in presenting stimuli to the index and ring fingers instead of the adjacent fingers in order to enhance the ability to discriminate which finger was being presented with a haptic cue [1].

Reaction time (RT) was defined as the difference between the time at which a stimulus command was initiated and the time at which the threshold x_A was crossed,

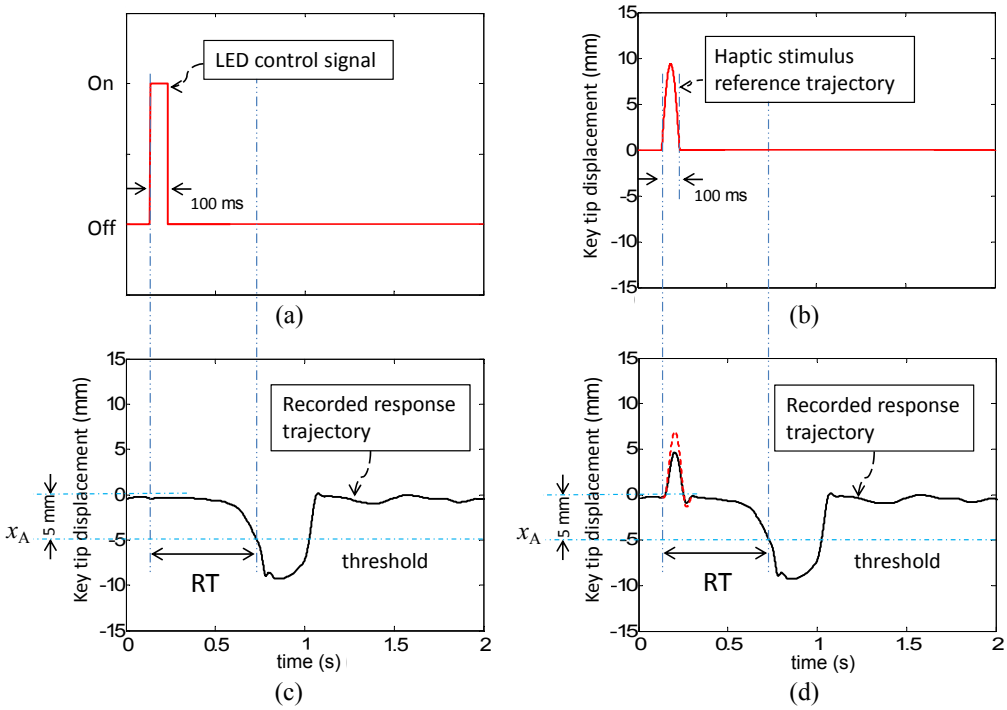

Figure 2.4: The command signals for visual and haptic stimuli and recorded responses: (a) The control signal to turn on/off the LED for visual stimuli. (b) The reference position to be followed by the tip of the key for haptic stimuli. (c) A sample of atypical recorded trajectory responding to a visual stimulus. (d) A sample of typical recorded trajectories in response to a haptic stimulus(dashed line: without the finger resting on the key,solid line: with the finger resting on the key). Reaction time(RT)was defined as the difference between the initial stimulus command and the point at which the key crosses the threshold. Both visual and haptic stimuli were presented for a 100 ms time interval.

as presented in Fig. 2.4. The participants view of their hands was blocked using a box and white noise was presented via headphones in order to eliminate spurious audio cues.

Procedure

All participants were randomly and evenly divided into two groups: one group (N = 16) responded to visual stimuli (the visual group), while the other group (N = 16) responded to haptic stimuli (the haptic group). Each of these two groups was randomly and evenly divided into two subgroups. One of the two subgroups (N = 8) was assigned to the transfer condition that preserved stimulus sequence across transfer (perceptual condition), whereas the other subgroup (N = 8) was assigned to the transfer condition that preserved response sequence across transfer (motor condition). For convenience, the four subgroups will be named visual-perceptual, visual-motor, haptic-perceptual, and haptic-motor subgroups, respectively. The motor and

perceptual conditions will be further explained below. The motor and perceptual conditions were different only in name up until the transfer phase, at which point different sequences (one of them shifted) were presented to the two subgroups.

Responses to stimuli were made either in the so-called "incompatible" or "compatible" stimulus-response mappings. In the incompatible mapping, participants were instructed to press the key one position to the right of the position at which the stimulus appeared. If the stimulus on the far right appeared, they were to press the key on the far left.

The experiments unfolded in three stages: the familiarization, training, and transfer phases. Before the SRT task began, the familiarization phase was introduced to allow participants to practice making responses on the keyboard apparatus. This phase provided an opportunity to teach participants how to press the keys properly and to ensure they understood the incompatible and compatible stimulus-response mappings. Participants were allowed to view their hands during this exercise to facilitate this learning process. When participants were able to demonstrate proper key pressing and stimulus-response mappings, the familiarization phase was stopped, and the SRT task began.

In the training phase, all participants performed the SRT task in the incompatible stimulus-response mapping, regardless of whether visual or haptic stimuli were presented. All four subgroups experienced the same stimulus sequences during this phase. Shortly afterward, the transfer phase followed, to test whether or not the sequence knowledge acquired during the training phase appeared in the compatible mapping and whether it appeared to differing degree according to the stimulus type (haptic/visual) or presentation mode (perceptual/motor).

Now I define the perceptual and motor presentation modes after transfer in detail. In the transfer phase, the visual-perceptual and the haptic-perceptual subgroups responded using the compatible mapping to cues delivered in sequences that were not altered from those delivered during the training phase (under the perceptual condition). However, the visual-motor and haptic-motor subgroups responded during transfer using the compatible mapping to cues delivered in sequences that were shifted so that the sequence of responses (key presses) would turn out identical to those made in the training phase. That is, in the perceptual condition, the sequence of responses was shifted since cue delivery (perceived sequences) was the same across the training and transfer phases, while under the motor condition, the sequence of responses remained consistent (unshifted, with motor responses the same across training and transfer phases), since cue delivery was shifted across the training and transfer phases.

Both visual and haptic stimuli were presented for a 100 ms time interval and then turned off, as described in Fig. 2.4. The response-to-stimulus interval (RSI) was 250 ms for correct responses. All participants were asked to respond as fast as possible without making errors in a manner that corresponded to the incompatible mapping in the training phase and compatible mapping in the transfer phase. Responses were declared erroneous when participants failed to press the appropriate key or make a response within 1.5 s of stimulus presentation. Errors were signaled to participants via audio tones and an extended RSI of 1 s. Thirty second breaks were provided between blocks.

Stimulus events (cues) were organized into sequences of 12 and were constructed according to the rules of second-order conditional (SOC) sequences. In a SOC sequence, each event can be predicted only by a unique combination of two preceding events and each pairwise association is equally likely so that pairwise association cannot be used to predict subsequent stimuli [94]. These sequences were then organized into blocks of 108 events. Two types of blocks were presented: sequence blocks that consisted of one SOC (242134123143) repeated nine times, and pseudorandom blocks which consisted of nine distinct, successively presented SOCs picked from a pool of 12. Sequences were presented seamlessly such that participants were only aware of a set of 108 events, and each SOC sequence presented was initiated at the beginning.

The training phase comprised one pseudorandom block succeeded by seven sequence blocks, a pseudorandom block (block 9) and a final sequence block (block 10). The first pseudorandom block acclimated participants with the task and established a baseline RT while the final pseudorandom block allowed us to differentiate sequence learning from general practice effects. Transfer consisted of two pseudorandom blocks (blocks 11 and 12) for adjusting to the new mapping; one sequence block (block 13) and a final pseudorandom block (block 14). A given participant never experienced the same pseudorandom block twice. Median RT and error percentage were displayed for participants between blocks.

Awareness survey

After the experiment, a 6-question survey was conducted to determine how much explicit knowledge participants had gained. Question 1 asked participants to choose from a list of four alternatives the statement that best described the task carried out: (1) Stimulus presentation was completely random, (2) Some fingers had to respond more often than others, (3) Sometimes I wanted to respond before stimulus presentation, and (4) Stimulus presentation was mostly structured [1]. Questions 2 and 3 were adapted from the process dissociation procedure (PDP) introduced in

[24]. Question 2 required participants to generate the 12-event sequence experienced (inclusion) while Question 3 asked participants to generate another 12-event sequence that completely avoided the first (exclusion). Participants were told to recall the sequence as experienced in the training phase [8]. During these exercises, populating the sequence with repeating smaller patterns was not allowed (e.g., 123412341234 would not be a valid response). Therefore chance level was 0.33. In Question 4, six different SOC sequences were presented through the apparatus in whichever modality participants trained and the participants were asked to identify the correct one (the sequence experienced during training). Questions 5 and 6 asked the participants to rank their engagement in the task and the tasks difficulty on a scale of 1 to 5 (5 being very engaged and very difficult, respectively).

Training scores, transfer scores, and awareness scores

Median RTs were obtained for each participant and block of data (nominally 108 responses), though RTs from erroneous responses and trials immediately following erroneous responses were excluded. We chose median RT over mean RT for its robustness to outliers. The median was then averaged across the participants within a group (subgroup) to determine an overall RT value for each block and group (subgroup). Two learning scores were computed in terms of RT: a Training RT Score and a Transfer RT Score. The Training RT Score was determined by subtracting the average of the RT values in blocks 8 and 10 (sequence blocks) from the RT value in block 9 (a random block). The Transfer RT Score was determined by subtracting the RT value in block 13 (a sequence block) from the average of the RT values in blocks 12 and 14 (random blocks).

For Error Scores, error rates were first obtained for each participant and block of data. I then averaged them across the participants within a group (subgroup) to determine an overall error value for each block and group (subgroup). Two Error Scores were computed: a Training Error Score and Transfer Error Score. The Training Error Score was determined by subtracting the average of the error rates in blocks 8 and 10 (sequence blocks) from the error rate in block 9 (a random block). The Transfer Error Score was determined by subtracting the error rate in block 13 (a sequence block) from the average of the error rates in blocks 12 and 14 (random blocks).

We computed Training RT Scores and Training Error Scores for each group (visual/haptic) but not condition (no subgroups) since there were no differences in the cues presented to the subgroups in the training phase.

To obtain Awareness Scores, the sequences generated by participants in response

to Questions 2 and 3 were broken into 3-element chunks. The actual sequence used in that participants sequence blocks was likewise divided. Chunks from the generated sequences were compared against those in the actual sequence and the number of correct chunks was divided by 12 (the maximum possible number of correct chunks) resulting in an awareness score between zero and one. The awareness scores were calculated for each participant in both inclusion and exclusion recall tasks.

Data analysis

I employed ANOVA and t-tests for statistical analysis as elaborated below. Statistical analyses were performed with SPSS (Windows v.21, SPSS Inc.). Significance level was set at 0.05. I used a mixed-design ANOVA and repeated-measure ANOVA to investigate performance change across repeated measurements and to assess how stimulus (visual/haptic) or/and condition (perceptual/motor) influenced these changes. Two-way ANOVAs were used to test for significant differences in mean across the four subgroups. If the sphericity assumption in ANOVAs was violated, GreenhouseGeisser adjusted p-values were used.

Independent-sample t-tests were carried out to test whether the two groups were significantly different in means. I used one-tailed t-tests to determine whether learning scores were greater than zero. Paired-sample t-tests were employed in cases where data were paired.

2.0.2 Results

Reaction times improved with practice regardless of whether the cues were delivered in the visual or the haptic modality. Fig. 2.5 shows the means of individual median RTs computed for both the visual and haptic groups in the training phase and for each of the four subgroups in the transfer phase. Downward trends in RT appeared as participants practiced in the training phase in blocks 2 through 8. Since a pseudorandom block followed sequence block 8, increases in RT occurred at block 9. But RTs decreased again for sequence block 10. Notable drops in RT occurred at the transition from the training phase to the transfer phase (between blocks 10 and 11), which could be expected since the compatible mapping is easier than the incompatible mapping. Also, as expected, decreases in RT appeared at sequence block 13, because participants benefited from knowledge of the sequence acquired during the training phase.

Trends in the training phase (blocks 2-8)

Because all subgroups experienced the same sequences in the training phase, I did not differentiate the groups by Condition; we partitioned participants into the visual

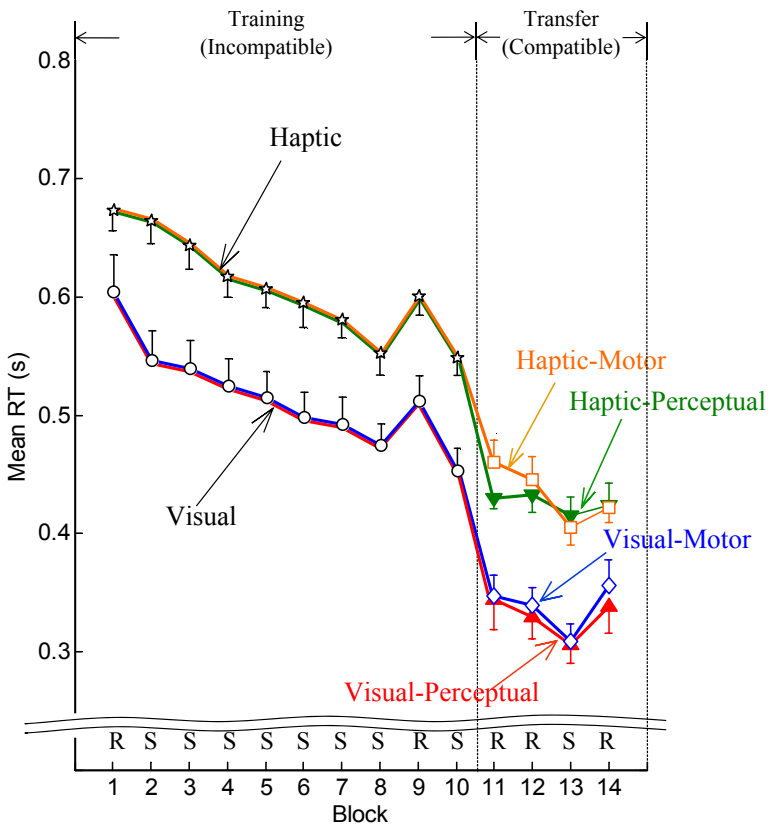

Figure 2.5: Mean by group and subgroup of individual median RTs for the training phase (blocks 1-10) and transfer phase (blocks 11-14). Error bars are ± 1 standard error of the mean. R and S stand for pseudorandom and sequenced stimuli, respectively.

and haptic groups regardless of the perceptual and motor conditions.

Repeated-measure ANOVAs were performed on median RTs and error rates from block 2 to block 8 to evaluate participants performance with Block (seven levels: blocks 28) as a within-subject variable and Stimulus (two levels: visual and haptic) as a between-subject variable. RTs for the haptic group were in general longer in comparison to the visual group (see Fig. 2.5). ANOVA produced a significant main effect of Stimulus [$F(1,30) = 12.463$, MSE = 0.515, $p < 0.001$, $\eta_p^2 = 0.294$]. A main effect of Block [$F(4.128,123.839) = 32.381$, MSE = 0.048, $p < 0.001$, $\eta_p^2 = 0.519$] was also significant. Polynomial contrasts reported a linear trend in Block [$F(1,30) = 104.388$, MSE = 0.197, $p < 0.001$, $\eta_p^2 = 0.777$]. The other main and interaction effects were not significant (all $p > 0.1$). Likewise, error rates were generally higher in the haptic group than in the visual group regardless of Condition (see Fig. 2.6). ANOVA reported a significant main effect of Stimulus (visual/haptic) [$F(1,30) =$

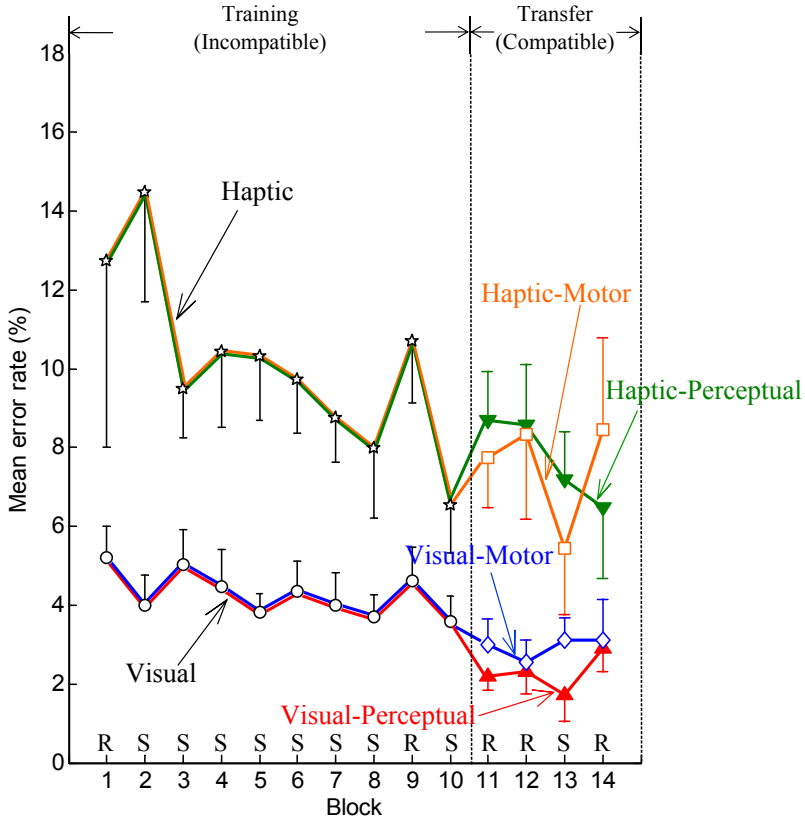

Figure 2.6: Mean by group and subgroup of individual error rates for the training phase (blocks 1-10) and transfer phase (blocks 11-14). Error bars are ± 1 standard error of the mean. R and S stand for pseudorandom and sequenced stimuli, respectively.

17.458, MSE = 1800.506, $p < 0.001$, $\eta_p^2 = 0.368$]. The other main and interaction effects did not reach significance (all $p > 0.1$).

Sequence-unspecific learning

I investigated sequence-unspecific learning in the visual and haptic groups in the training phase by comparing pseudorandom blocks 1 and 9. A repeated measures ANOVA was performed on RT with Block (two levels: blocks 1 and 9) as a within-subject variable and Stimulus (two levels: visual and haptic) as a between-subject variable. A main effect of Stimulus [$F(1,30) = 8.291$, MSE = 0.101, $p < 0.01$, $\eta_p^2 = 0.217$] reached significance, implying that the haptic group showed higher RTs at the pseudorandom blocks than the visual group. A main effect of Block [$F(1,30) = 30.234$, MSE = 0.110, $p < 0.005$, $\eta_p^2 = 0.502$] was significant, indicating that sequence-unspecific learning occurred in both the visual and haptic groups. The interaction (Stimulus Block) was not significant ($p = 0.533$).

Similarly, a repeated measures ANOVA was used to analyze error rate with Block (two levels: blocks 1 and 9) as a within-subject variable and Stimulus (two levels: visual and haptic) as a between-subject variable. A main effect of Stimulus [$F(1,30) = 7.431$, MSE = 739.79, $p < 0.05$, $\eta_p^2 = 0.751$] was significant, indicating that the haptic group exhibited higher error rates at the pseudorandom blocks than the visual group. The ANOVA on error rate reported no other main or interaction effects (all $p > 0.1$).

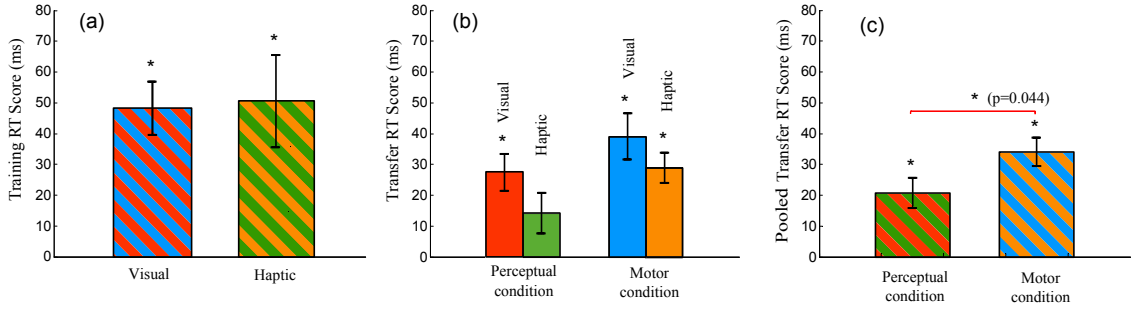

Figure 2.7: Training RT Score and Transfer RT Score. The Training RT Score is defined as a difference in RT between the means of blocks 8 and 10 and block 9, and the Transfer RT score is defined as a difference in RT between the means of blocks 12 and 14 and block 13. (a) Training RT Scores of the visual and haptic groups (no differences in the cues presented to the subgroups in the training phase). (b) Transfer RT Score of the visual-perceptual, haptic-perceptual, visual-motor, and haptic-motor subgroups. (c) Pooled Transfer RT Score (averaged across the visual and haptic groups) in each condition. The motor group shows a significantly greater pooled Transfer RT Score than the perceptual group (ANOVA, $p = 0.044$). Error bars are $\pm$ 1 standard error of the mean. An asterisk on a line linking bars indicates a significant difference between two groups (subgroups) while an asterisk above a bar indicates a significant difference from zero.

Training RT scores and training error scores

Each Training RT Score quantifies the increase in RT of pseudorandom block 9 over the average RT of sequence blocks 8 and 10. One-tailed t-tests revealed that the Training RT Scores were significantly greater than zero in the visual and haptic groups, as indicated with asterisks over the bars in Fig. 2.7(a). However, independent-sample t-tests comparing between groups reported that there was no significant difference between the visual and haptic groups in Training RT Scores [$t(30) = 0.139$, $p = 0.89$].

While there was no difference in Training RT Scores across the visual and haptic groups, the difference in Training Error Scores reached significance [$t(30) = 2.117$, $p = 0.043$], as displayed in Fig. 2.8(a). Each Training Error Score quantifies the increase in error rate of pseudorandom block 9 over the average error rate of sequence blocks

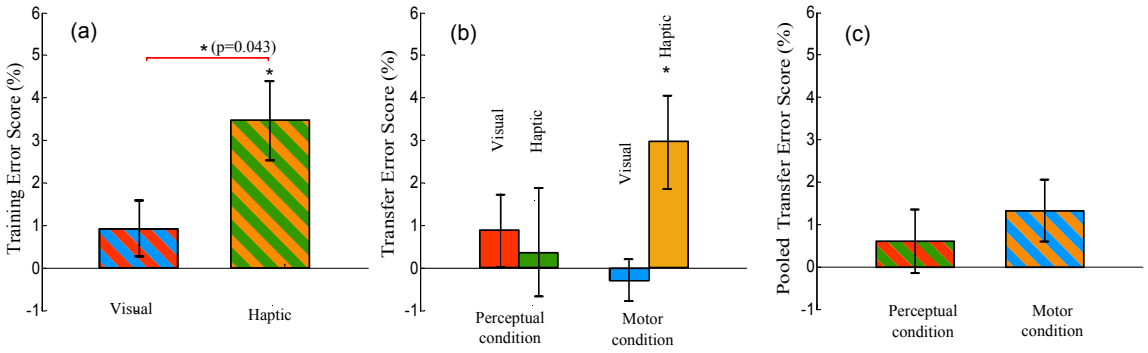

Figure 2.8: Training Error Score and Transfer Error Score. The Training Error Score is defined as a difference in error rate between the means of blocks 8 and 10 and block 9, and the Transfer Error score is defined as a difference in error rate between the means of blocks 12 and 14 and block 13. (a) Training Error Scores of the visual and haptic groups. There is a significant difference between the two groups (t-test, $p = 0.043$). (b) Transfer Error Score of the visual-perceptual, haptic-perceptual, visual-motor, and haptic-motor subgroups. (c) Pooled Transfer Error Score (averaged across the visual and haptic groups) in each condition. Error bars are $\pm$ 1 standard error of the mean. An asterisk on a line linking bars indicates a significant difference between two groups (subgroups) while an asterisk above a bar indicates a significant difference from zero.

8 and 10.

Transfer RT scores and transfer error scores

In the transfer phase (blocks 11 through 14) all participants responded to cues using a compatible mapping. The cues were delivered during the transfer phase such that the visual-perceptual and haptic-perceptual subgroups experienced cues that preserved the stimulus sequence across blocks 10 and 11, while the visual-motor and haptic-motor subgroups experienced cues that preserved the motor response sequence across blocks 10 and 11. Thus there were four Transfer RT Scores and four Training Error Scores computed, one each for each of the four subgroups.

One-tailed t-tests revealed that the Transfer RT Scores were significantly greater than zero in all the subgroups with the exception of the haptic-perceptual subgroup which was close as well (the haptic-perceptual subgroup: $p = 0.068$). Asterisks over the bars indicate the significant differences from zero in Fig. 2.7(b). These significant differences from zero imply that all the subgroups other than the haptic-perceptual subgroup utilized the advantage of their skills gained during the training phase in reducing RTs at sequence block 13.

Meanwhile, one-tailed t-tests revealed that the Transfer Error Scores were significantly greater than zero in only the haptic-motor subgroup: $t(7) = 2.710$, $p = 0.006$, as indicated in Figs. 1.8(a) and 1.8(b). The other three subgroups did not show

significant differences from zero (the visual-perceptual: $p = 0.346$, the visual-motor: $p = 0.551$, the haptic-perceptual: $p = 0.788$)

Two-way ANOVAs across the four subgroups were used to test for differences among subgroups, with Stimulus and Condition as between-subject variables. For the Transfer RT Scores (the increase in the average RT of pseudorandom blocks 12 and 14 over the RT of sequence block 13), the main effect of Stimulus and Stimulus $\times$ Condition interaction were not significant (all $p > 0.1$, Fig. 2.7(b)). However, ANOVA revealed a significant main effect of Condition [$F(1,28) = 4.43$, MSE $= 0.001$, $p = 0.044$, $\eta_p^2 = 0.137$], implying that the knowledge was transferred better in the motor condition than in the perceptual condition, as exhibited in Fig. 2.7(c).

For the Transfer Error Scores (the increase in the average error rate of pseudorandom blocks 12 and 14 over the error rate of sequence block 13), the ANOVA reported no significant main effects of Stimulus and Condition and no Stimulus$\times$Condition interaction (see Figs. 1.8(b) and 1.8(c)).

In sum, I had participants practice a SRT sequence task in which responses were cued either visually or haptically. Responses were prolonged when haptically cued, but the two groups exhibited parallel slopes of improvement during sequence repetition. Though both the visual and haptic groups showed a similar amount of sequence learning in terms of RTs, the haptic group gained more sequence learning than the visual group in terms of the number of errors made. I note that the SRT task resulted in a greater amount of motor learning than perceptual learning, irrespective of the stimuli (visual or haptic).

Awareness

It is noteworthy that the awareness survey revealed that the sequence knowledge participants had gained during the SRT task was "implicit". Also, the awareness survey showed that participants in the haptic group perceived more difficulty in performing the SRT task than participants in the visual group.

Table 1.1 summarizes the results of the awareness survey. For analysis of Questions 2 and 3, inclusion, and exclusion scores were calculated for each participant and averaged per subgroup (see Table 1.1). However, since the participants were told to recall the sequence experienced in the training phase (the same sequence was presented regardless of Condition), we considered only the visual and haptic groups, which were distinguished strictly by Stimulus. One-tailed t-tests were used to compare the mean inclusion and exclusion scores (collapsed by modality as there were no reliable group differences) to chance level (0.33). This revealed that both inclusion [$t(15) = 2.763$, $p = 0.007$] and exclusion [$t(15) = 3.201$, $p < 0.005$] scores in the

haptic group are reliably greater than chance. The visual groups inclusion scores were greater than chance [$t(15) = 3.844$, $p < 0.005$] but the exclusion scores were not [$t(15) = 1.069$, $p = 0.151$], which would traditionally indicate explicit knowledge. However, paired-sample t-tests between inclusion and exclusion scores for the visual [$t(15) = 1.438$, $p = 0.171$] and haptic [$t(15) = 0.115$, $p = 0.910$] groups show that neither group's means were significantly different, suggesting that participants did not recognize the sequence they experienced. The idea that such recognition should exhibit itself among participants with explicit knowledge is central to the application of the PDP in the SRT task along with the notion that comparing scores to chance level is not, by itself, an accurate indicator of awareness. As a significant difference was not observed in the visual group nor the haptic group, we could assert that sequence knowledge was largely implicit.

In Question 4, all subgroups except for the haptic-perceptual subgroup had only two members recognize the correct sequence. Four members of the haptic-perceptual subgroup identified the correct sequence. One member of the visual-perceptual subgroup was not able to complete this question.

Table 1.1 also presents participants average scores for Questions 5 and 6. For analysis of Questions 5 and 6, two-way ANOVAs were conducted with Stimulus and Condition as between-subject variables and Awareness Score as a within-subject variable. For Question 5 (how engaged participants were in the task), ANOVA revealed no significant main effects or interactions. For Question 6 (about the difficulty of the task), ANOVA reported a significant main effect of Stimulus [$F(1,28) = 9.9$, MSE = 7.031, $p < 0.005$, $\eta_p^2 = 0.261$], with the haptic group showing higher scores than the visual group. The main effect of Condition and interaction of Stimulus by Condition were not significant.

2.0.3 Discussion

We set out to determine whether haptic cues delivered to the fingertips would favor motor-based learning over perceptual learning, thinking that the effect would be even stronger with haptic cues than with visual cues. Willingham showed that sequence learning with visual cues favors motor learning over perceptual learning [118]. Thus we expected a change in the cueing across the transition from incompatible to compatible mapping that preserved the sequence of motor responses would enable our participants to respond more quickly and with fewer errors than a change in cueing that preserved the sequence of stimuli. But further, we expected this effect to be stronger for a participant group that received haptic cues delivered to the fingers than a participant

		Visual-perceptual	Visual-motor	Haptic-perceptual	Haptic-motor
Question 1	Option 1	n=0	n=2	n=1	n=1
	Option 2	n=0	n=0	n=0	n=2
	Option 3	n=3	n=2	n=2	n=4
	Option 4	n=5	n=4	n=5	n=1
Question 2		0.468 ± 0.099	0.417 ± 0.126	0.469 ± 0.117	0.417 ± 0.204
Question 3		0.364 ± 0.133	0.375 ± 0.173	0.448 ± 0.133	0.427 ± 0.144
Question 4		n=2	n=2	n=4	n=2
Question 5		4.5 ± 0.534	4.625 ± 0.518	4.5 ± 0.534	4.875 ± 0.354
Question 6		3.0 ± 0.534	2.625 ± 0.744	4.0 ± 0.756	3.5 ± 1.195

Table 2.1: A summary of awareness survey results. The rows for Questions 1 present how many participants chose each option. The row for Questions 4 presents how many participants chose the correct answer. The remaining rows present the averaged values by subgroup with standard deviations.

group that received visual cues. We hypothesized that cues delivered directly to the fingers would have a closer relationship to the responses produced by the fingers than cues delivered to the eyes. Roughly, we thought that haptic cues might engage motor memory by virtue of being delivered to the body site of the motor apparatus involved in responding to the cues.

Implicit learning in the training phase

In general, participants responded more slowly to haptic cues than to visual cues. This result is consistent with the study of Abrahamse et al., which reported that response times were noticeably longer with vibrotactile stimuli than with visual stimuli [1]. These results are likely due to distinct processing of visual and haptic cues and perhaps distinct pathways between processing centers or centers that mediate learning [17, 42, 60]. Another factor may be the longer pathway to the brain from the manual haptic receptors than from the retina. Nonetheless, the rates of RT improvement through blocks 28 were not significantly different between the visual and haptic groups (parallel downward slopes can be noted in Fig. 2.5).

While the RTs for the haptic group were longer, the savings in RT enabled by the presence of the sequence once the sequence was learned (encapsulated in the Training RT Score) indicate a similar degree of learning during training between the visual and haptic groups. This contrasts with the result in the study of Abrahamse et al. that showed that visual cues produce better sequence learning than vibrotactile cues [1]. We attribute these differences to the greater salience of haptic cues delivered to the fingertips in the current study than the vibrotactile cues delivered to the proximal phalanx in [1].

The haptic group also demonstrated a significantly better Training Error Score than the visual group ($p = 0.043$, Fig. 2.6(a)), indicating a stronger reliance on the presence of the sequence in the haptic group at the end of the training phase. Note that the lack of significant difference in Training RT Score between the visual and haptic groups indicates that the participants were not trading off error rate for RT performance. The difference in Training Error Score but lack of significant difference in Training RT Score may indicate that haptic cues favor response-response learning [1] or that learning for our haptic group was encoded in the "what" of sequence execution and not so much in the "how". We will discuss this distinction at greater length in light of the Transfer Result below.

Implicit learning in the transfer phase

Our central hypothesis, that haptic cues would favor motor learning even more than visual cues, was not supported by the differences in RT across our participant subgroups. There were no significant differences in the Transfer RT Score across the four subgroups (see Fig. 2.7(b)). Only when the subgroups were pooled together into a motor group and a perceptual group, differences in RT Score across condition were significant ($p = 0.044$), as shown in Fig. 2.7(c).

It is curious that our visual-motor subgroup did not outperform our visual-perceptual subgroup, as the experimental conditions experienced by these subgroups were by design essentially equivalent to those found in Experiment 3 in [118], which established that sequence learning transfers better in the motor condition under visual cueing. Differences in our experiment design did exist, however; we used the index and ring fingers in each hand rather than the index and middle fingers of each hand. We would expect an elevated motor-based learning versus perceptual learning with the use of the index and ring fingers instead of the adjacent fingers, because it would facilitate the ability to discriminate the locations of responding fingers when coded in the egocentric space, a spatial frame that codes the locations of objects relative to part of the body. But our result does not duplicate Willingham's result. Perhaps the design of our buttons (which required a throw of more than 5 mm) or other features of our arrangement are responsible for the difference. Our result is, however, consistent with his following study [8]. Bischoff-Grethe et al. also employed the same experimental protocol [8]. This study reported that there was no significant difference between the perceptual and motor groups regardless of the extent of knowledge about sequences, although four fingers of one hand were used to respond to visual stimuli.

In terms of error rates, our central hypothesis did receive some support from our experiment. Participants in the haptic-motor subgroup made on average 3% fewer

errors when the sequence was present in the transfer phase while the other three subgroups did not show a reduction in errors. That is, the haptic-motor subgroup realized a 3% increase in Transfer Error Score (significantly different from zero, $p = 0.006$) while the other three subgroups had Transfer Error Scores that were not significantly different from zero. Taken together, the support our central hypothesis received from the Transfer Error Scores and lack of support our central hypothesis received from the Transfer RT Scores may indicate that haptic cues favor only certain aspects of motor learning. That is, perhaps motor learning must be defined more narrowly in the context of sequence learning. It has been suggested that higher error rates indicate that sequence execution is influenced not so much by the stimuli but by the previously learned motor or movement patterns. In this sense, increased error rates at a pseudorandom block relative to surrounding sequence blocks could be interpreted as an indication that movement patterns were guided by the preceding movements rather than the cues. Evidently only the haptic-motor subgroup profited from the involvement of this type of association in learning (Fig. 2.8(b)). This pattern of exhibiting sequence-specific knowledge in terms of accuracy has also been interpreted as participants knowing "what" to do for sequence execution. The lack of a comparable effect size in RT suggests that they cannot translate this into how to perform the sequence quickly [47, 103]. It is perhaps reasonable to assume that "what" and "where" is a kind of embodied knowledge, relying on motor memory or a motor program that is cued by reafferent proprioceptive stimuli, while "how" is more central, relying on stimuli collected from various external sources and assembled centrally into a pattern and program. It is possible that haptic cues are in fact more readily associated with a motor response in the sense of a motor program that governs positioning in the allocentric space, a spatial frame that codes the locations of objects relative to the environment. Note, however, that our current experiment did not test this hypothesis explicitly. The association is worth further exploration.

The lack of a significant interaction effect on Transfer Error Score, an indicator of whether haptic cues contribute differently than visual cues to the balance of motor and perceptual learning, might be due to the sample size. The partial eta squared (η_p^2) for the interaction effect was reported as 0.121. We found through a power analysis that 17 participants per subgroup would be needed to detect significance with power of 0.80 and alpha of 0.05. It may be that, with larger sample sizes, the Transfer Error Score interaction would have been significant. This should be explored in future studies.

The results of the awareness survey also indicated that the haptic group developed

a stronger motor representation than the visual group. Four participants in the haptic-motor subgroup responded "Sometimes I wanted to respond before stimulus presentation," which is greater than in the other subgroups.

In sum, we had participants practice a SRT task in which responses were cued either visually or haptically. Responses were prolonged when haptically cued, but the two groups exhibited parallel slopes of improvement during sequence repetition. Though both the visual and haptic groups showed a similar amount of sequence learning in terms of RTs, the haptic group gained more sequence learning than the visual group in terms of the number of errors made. We found that irrespective of the stimuli (visual or haptic) the SRT task leads to a greater amount of motor learning than perceptual learning. Moreover, transfer tests revealed that the haptic group acquired a stronger motor-based representation than the visual group in terms of the number of errors made.

CHAPTER III

Design and Control of Backdriveable Actuators

We live in an era in which robotic systems assist us or collaborate with us in our work and generally seep into our daily lives. Such collaboration involves mechanical interactions between the human and robot. Backdriaveability, during interaction with humans, should not have to be compromised for safety.

Series elastic actuators (SEAs) are used in robot designs because of its safety feature to humans interacting with robots [91,113]. In SEAs, compliance is purposefully introduced between an actuator and robot end-effector. The compliance masks the high impedance of the actuator from humans or environments. The high-frequency behavior of SEAs is that of the compliant element. SEAs are able to maintain low impedance (a very compliant spring) at high frequencies. Furthermore, they offer an ability to shape the impedance within their operational bandwidths. Actuation that employs compressible fluid takes over the advantages of series elastic actuation in that the fluid compressibility provides elasticity between a bulky and heavy actuator and end-effector. In this chapter, I shed light on the advantages of fluidic actuation that covers many features of SEAs.

Soft robotics is a burgeoning field that is attracting attention due to its high compliance and backdriveability during contact. A compliant structure together with a fluid pressure or flow source and some flexible conduits can elegantly fit the needs of numerous applications (see [63] for a review). For example, soft actuators can be form-fitting and accommodating in wearable robot designs and can be highly tolerant to off-axis loading and thus resilient to falling or crushing as needed for search and rescue robots. Conventional robots with rigid links are usually driven by electromagnetic actuators that are necessarily stiff in off-axis directions to hold magnetic gaps. In contrast, soft actuators often lack bearings altogether. Indeed, the dividing line between actuator and linkage is often blurred in soft robotics, enabling solutions that avoid structural complexity and bulkiness.

A chamber with compliant walls will expand in response to an increase in internal pressure, induced for example when additional fluid is pushed into the chamber. If the walls are uniformly compliant, then the chamber will maintain its basic shape as it expands, like a balloon (Fig. 3.1(a)). If the walls have nonuniform compliance, then expansion will be accompanied by a change in shape. One means to produce a non-uniform distribution in compliance is the use of variable wall thickness as in the eye-popping Martian squeeze toy (Fig. 3.1(b)). Alternatively, compliant structures with strategically chosen resting shapes can be incorporated into the chamber walls to produce interesting shape changes, as in the party blower (Fig. 3.1(c)). The incorporation of inextensible fibers into the chamber walls is another important means for controlling the changes in shape as the internal pressure increases. The McKibben artificial muscle (Fig. 3.1(d)) is an example wherein two families of fibers wound helically around a cylinder cause a change in length in response to a change in volume. The McKibben artificial muscle with its symmetrically wound fibers has much in common with certain soft-bodied animals, including worms, octopus arms, and elephant trunks. The McKibben muscle can be generalized to an actuator capable of twisting about its long axis if the two families of helically wound fibers are wound with different angles. The available motions from soft actuators include longitudinal expanding, radial expanding, bending, and twisting [9, 67, 82, 89, 107].

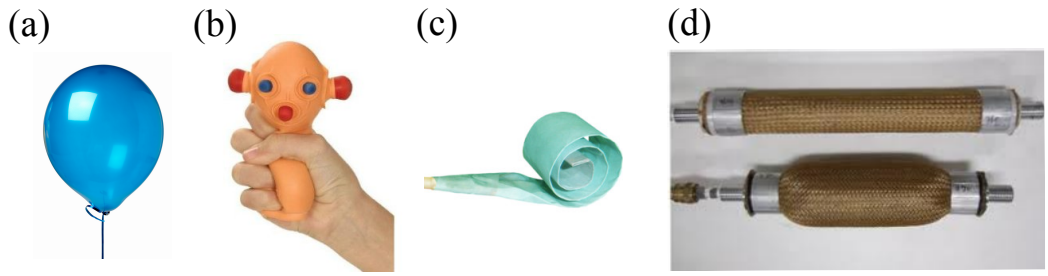

Figure 3.1: Fluidic Actuators: (a) Balloon. (b) Alien pop-eye squeeze toy. (c) Party favor whistle. (d) McKibben artificial muscle.

Soft actuator designs, however, must cope with certain limitations. Most soft robotic actuator designs to date are elastic structures that store elastic energy at the same time that they actuate. The mechanical work supplied to the actuator must include both the work available to be imposed on the environment and work stored as elastic energy as the actuator moves. If the application within which the actuator is to be used involves a limited supply of fluid power, and the means to recover work stored as elastic energy is not available, then traditional soft robotic actuators may not be appropriate. Moreover, elastomeric chambers tend to expand in all directions

even when only a certain direction is targeted. Inextensible fiber or fabric may not fully restrict expansion to the target direction. That is, energy supplied may be wasted on expansion in off-axis directions.

Figure 3.2: The three-banded armadillo rolling into a sphere.

The armadillo is a mammal with armor-like rigid shells covering its upper body including shoulder and hip while its underside is covered with soft skin and fur. The three-banded armadillo shown in Fig. 3.2 retracts its body to a spherical shape by pivoting its two rigid shells about the skin-separated flexible bands across its back. Though the rigid shells exist for protection and the animal uses muscles for retraction, I can take inspiration from the armadillo. Rigid shells incorporated into chamber walls may be used to constrain and guide the shape change in a soft actuator. The goal is to use rigid shells to guide the transmission of fluid power into mechanical power in the target axes of motion. Forces transmitted across and between shells or plates may even be used to re-direct expansion in off-axis directions into on-axis forces or torques.

In this thesis, I propose a soft actuator design called the Origami Structured Compliant Actuator (OSCA). This actuator incorporates hinge-connected shells or plates arranged in a rigid origami structure. The plates contain, constrain, and guide fluid expansion into the target motion, which in this study is bending. Origami is the art and more recently science of paper folding that provides solutions for the design of closed 3D structures that can be folded and unfolded. Rigid Origami restricts all motion to the creases or hinge joints, disallowing bending or rolling of the paper between creases. Thus the paper between creases may be replaced with plates. It is possible to mechanically program the desired folding/unfolding trajectory of a rigid origami structure by rearranging the array of hinge joints between plates. Like conventional robots, these actuators are able to produce motion in predefined directions. But unlike conventional robots, these actuators maintain backdriveability (low back-drive impedance) and high force output capability. Power transmission can even be enhanced as rigid plates transfer forces that arise from pressurization to the target motion output. Moreover, kinematic singularities in the design may be used to

produce high mechanical advantages within certain ranges of motion. OSCA utilizes this singularity to advantage to create high mechanical advantages when desired.

Nishioka et al. [85] and Martinez et al. [75] adopted a bellows structure to create pneumatic actuators. The pattern of folds in the bellows determined the motions of their soft actuators on pressurization. But their bellows structures are are made of film and paper and were subject to bulging in off-axis directions, leading to energy losses.

In addition, I present control strategies for fluidic or SEA systems, putting an emphasis on the driving-point impedance. The system dynamics involving nonlinearities could be canceled out and the desired dynamics shaped with a desired impedance. This is the strategy that was used in the impedance controller presented by Hogan (1985) in [50]. He achieved dynamics compensation by using the identified system model. Once nonlinearities are compensated, high gain control is not needed for counteracting nonlinear dynamic behavior. Also, because the desired inertia is replaced with the system inertia, a lower impedance can be maintained over frequencies up to the actuator's controllable bandwidth. Achieving the desired inertia leads to the increase of the closed-loop bandwidth, which is inversely proportional to the square root of the effective inertia. As a result,the programmed stiffness dominates the behavior rather than the system dynamics.

In the study presented here, a comparative analysis of impedance control of SEA systems versus position control of SEA systems is carried out. I add impedance control (with dynamics compensation) of a rigid robot system to the comparative study. This makes evident the merit of SEA systems. Note that several impedance controllers can be seen as a position controller (e.g., [113]). But for the sake of convenience throughout this paper, I distinguish the term impedance control from the term position control using the term impedance control to describe the case that includes dynamics cancellation and substitution of desired dynamics.

Also, I propose a model-free and robust impedance controller incorporated with time delay estimation (TDE) for the proposed pneumatic exoskeleton. It is well known that pneumatic systems' main drawback is the difficulty in control due to the nonlinearity of air compression behavior [81]. In addition to the nonlinearity, it would be nearly impossible to identify the system model precisely. Unknown disturbances would get involved in the system. The TDE technique makes it possible to estimate all uncertainties including disturbances as well as system dynamics without a significant computational load. This enables the controller to cancel the system dynamics and include the desired dynamics and impedance. While efforts toward the combination

of impedance control and SEA systems (or flexible-joint systems) have been made in some studies [2, 13, 26, 80, 92], these controllers require a precise system model or high control gains to overcome uncertainties, or learning algorithms to estimate the system dynamics and unknown factors.

3.1 Backdrivability with compressible fluid

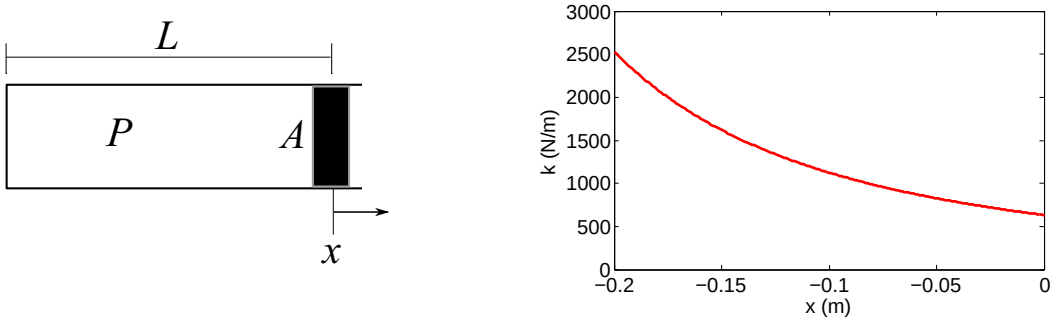

(a) (b)

Figure 3.3: (a) Cylinder and piston. (b) Stiffness of air of 0.001 m^3 with piston area $A = 0.0025$ m^2 at 20 ^{o}C (T=293 K). The parameters are selected as $L = 0.4$ m, $m = 0.0012$ kg, and $R = 287$ J/kgK.

It is well known that fluid is typically compressible [35]. A container filled with fluid such as air changes volume when it is pressed. If the applied force is removed, the container tends to return to its original state. The compressibility of fluid is often described using bulk modulus, but if the volume of air is allowed to expand or shrink in only one direction, the compressibility can be regarded as stiffness and the fluid as a spring. In this section, I elaborate on the idea that fluid compressibility can be described as a spring, taking a cylinder filled with 1 l (0.001 m^3) of air for example, which is depicted in Fig. 3.3(a). The force F applied to the piston by fluid is the product of the pressure inside the chamber P and the area of the piston A:

$$F = PA. \tag{3.1}$$

The stiffness effect of the fluid in the chamber can be obtained as follows, differ-

entiating force F with respect to position x:

$$k \triangleq -\frac{\partial F}{\partial x} = -\frac{\partial P}{\partial x} A. \tag{3.2}$$

With the following relationship coming from the assumption that the fluid in the cylinder is an ideal gas undergoing an isothermal process ($\Delta T = 0$),

$$P = \frac{mRT}{V} = \frac{mRT}{A(L+x)}, \tag{3.3}$$

where m, V are the mass and volume of the entrapped fluid, respectively; R the universal gas constant; T the absolute temperature and L the length of the cylinder.

The partial derivative of P with respect to x may be obtained as

$$\frac{\partial P}{\partial x} = -\frac{mRT}{A(L+x)^2} \tag{3.4}$$

Substituting Eq. (3.4) into Eq. (3.2) yields

$$k = \frac{mRT}{(L+x)^2}. \tag{3.5}$$

From Eq. (3.5), the fluid contained in the cylinder acts as a nonlinear spring. The stiffness k increases nonlinearly as the piston is pushed in, as shown in Fig. 3.3(b) (in the case of air). A further finding is that the stiffness of fluid depends on the cylinder length L; a longer L leads to a lower stiffness. This is analogous to the fact that the equivalent stiffness depends on the deployment of multiple springs; the equivalent stiffness of springs in series is lower than that of of springs in parallel.

Using compressible fluid in actuation, that is, including a container filled with compressible fluid between the actuator and end-effector provides several advantages in addition to flexible transmission and high force-to-weight ratios in fluidic systems (Fig. 3.4(a)). Fist, the fluid in the container masks the actuator's impedance including inertia and friction to the end-effector. As well, impact forces on the end-effector are absorbed by the fluid compressibility; it protects the actuator. But as a mediator, still, the fluid transmits energy from the actuator to the end-effector. These characteristics of fluidic systems are common to the primary features of a series elastic actuator (SEA, Fig. 3.4(b)), a concept of actuation that purposely introduces compliance between an actuator and end-effector. The compliance that is typically realized with a spring significantly reduces the backdrive impedance of the device. The actuator and

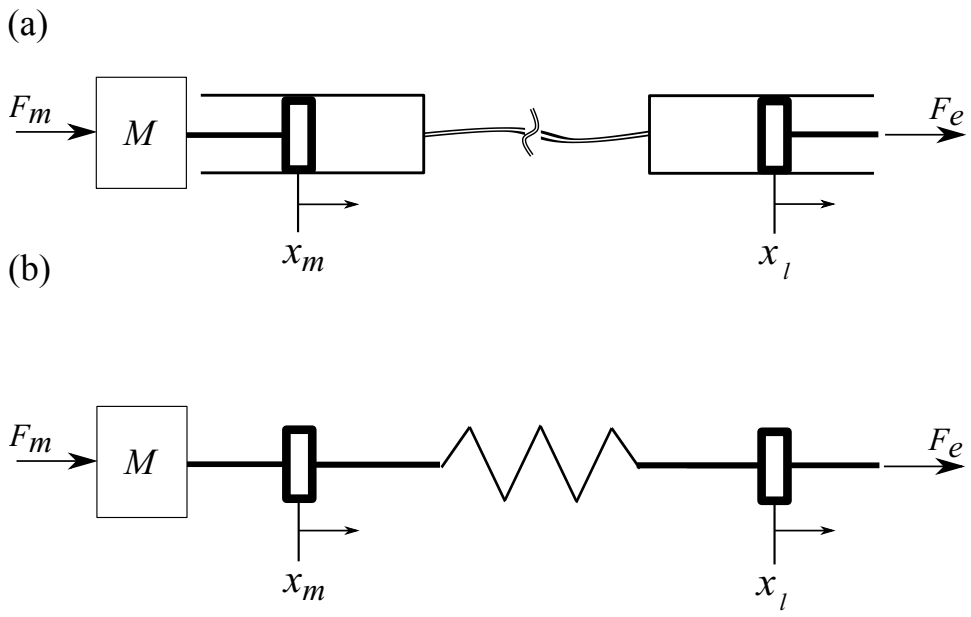

Figure 3.4: (a) Fluidic actuation with no fluid in and out, and (b) series elastic actuation.

transmission (including their equivalent mass and nonsmooth dynamics) are hidden behind the elastic element when viewed from the environment. Also, with a reduced apparent mass and intervening spring, impact forces are attenuated. This provides a safety feature to persons interacting with the robot and by the same taken the robot actuators and transmissions are protected. Fluidic systems with compressibility share these characteristics with SEA. These fluidic systems share the advantages and disadvantages of SEA. Table 2.1 summarizes the characteristics of fluidic actuation.

Advantages	Disadvantages
Decoupled actuator impedance	Limited stiffness
Reduced friction effects	Limited bandwidth
Inherent safety	High power requirement
Impact absorption	
Energy storage	
Flexible transmission	
High force-to-weight ratios	

Table 3.1: Characteristics of fluidic actuation.

Not only systems with fluid flow entrapped (no fluid in-and-out), but also systems that are controlled with fluid flow in and out can be regarded as a SEA system, as described in Fig. 3.5. I demonstrate this fact in the following. The output force F_l

that is generated by the piston in Fig. 3.5(a) may be expressed as

$$F_l = PA - P_{atm}A_r, \tag{3.6}$$

where P denotes the absolute pressure inside the chamber of the pneumatic circuit; P_{atm} the atmospheric pressure; A, A_r the piston areas.

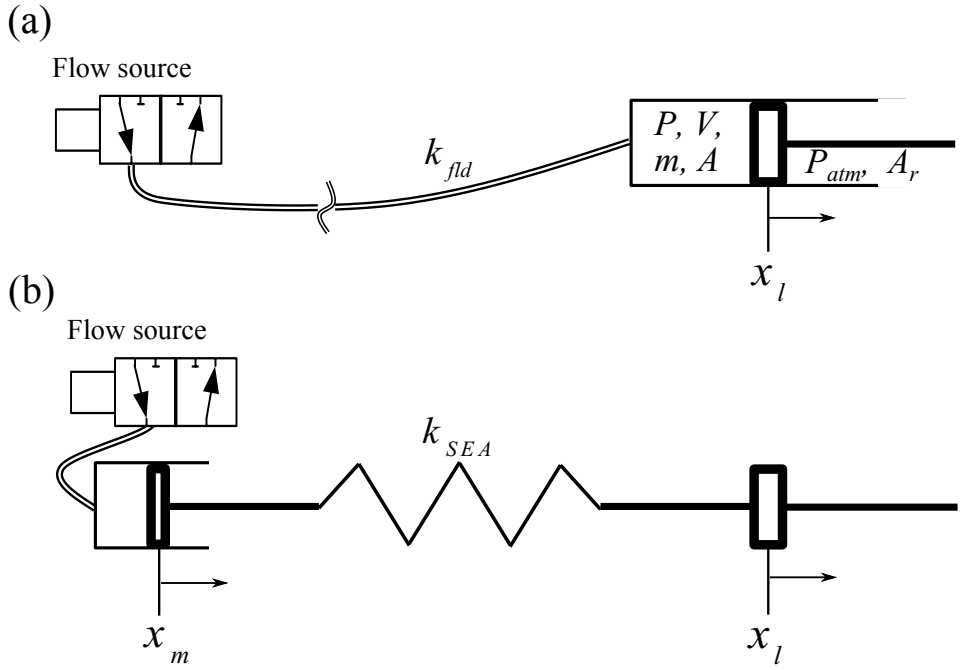

Figure 3.5: (a) Fluidic actuation with fluid in and out, and (b) its equivalent series elastic actuation.

Differentiating Eq. (3.6) with respect to time yields

$$\dot{F}_l = \frac{\partial F_l}{\partial m}\dot{m} + \frac{\partial F_l}{\partial x_l}\dot{x}_l. \tag{3.7}$$

Using the ideal gas law

$$P = \frac{mRT}{V} = \frac{mRT}{V_0 + Ax_l}, \tag{3.8}$$

where V_0 denotes the initial volume of the fluidic circuit,

the partial derivatives of F_l with respect to m and x_l are calculated as follows, respectively:

$$\frac{\partial F_l}{\partial m} = \frac{\partial PA}{\partial x_l} = \frac{RTA}{V_0 + Ax_l}. \tag{3.9}$$

$$\frac{\partial F_l}{\partial x_l} = \frac{\partial PA}{\partial x_l} = -\frac{mRTA^2}{(V_0 + Ax_l)^2}, \tag{3.10}$$

Then, Eq. (3.7) can be rewritten as

$$\dot{F}_l = \frac{RTA}{V_0 + Ax_l}\dot{m} - \frac{mRTA^2}{(V_0 + Ax_l)^2}\dot{x}_l. \tag{3.11}$$

The mass flow rate $\dot{m}$ is a control input to the pneumatic system. A servo valve connected to the chamber commands fluid mass flow $\dot{m}$ based on a current signal i, as described in Fig. 3.5(a).

Additionally, the stiffness of fluid is derived as

$$k_{fld} = -\frac{\partial F_l}{\partial x_l} = \frac{mRTA^2}{(V_0 + Ax_l)^2}. \tag{3.12}$$

Now, I convert the fluidic system (Fig. 3.5(a)) to an SEA system (Fig. 3.5(b)).

Uncompressed inflow Q from a pressure source actuates the piston, which position is denoted as z_m, and leads to the velocity of the piston, expressed as, in terms of flow Q,

$$\dot{x}_m = \frac{Q}{A} = \frac{\dot{m}}{\rho A}. \tag{3.13}$$

where ρ is density.

However, if the fluid entrapped in the circuit is compressed, elasticity occurs. The piston position in the compressed state is different from that in the uncompressed state (x_m). With the piston position in the compressed state denoted as x_l, the compression and elasticity (stiffness k_{SEA}) can be related with the output force $F_{l,SEA}$, as follows:

$$F_{l,SEA} = k_{SEA}(x_m - x_l). \tag{3.14}$$

And its derivative is given as,

$$\dot{F}_{l,SEA} = \dot{k}_{SEA}(x_m - x_l) + k_{SEA}(\dot{x}_m - \dot{x}_l). \tag{3.15}$$

If k_{fld} (3.12) is substituted into k_{SEA}, the derivative of the output force of the

SEA system $\dot{F}_{l.SEA}$ can be expressed as follows:

$$\begin{aligned}
&\dot{F}_{l.SEA} \\
=&\left(\frac{RTA^2}{(V_0+Ax_l)^2}\dot{m}-\frac{2mRTA^3}{(V_0+Ax_l)^3}\dot{x}_l\right)(x_m-x_l)+\frac{mRTA^2}{(V_0+Ax_l)^2}\dot{x}_m-\frac{mRTA^2}{(V_0+Ax_l)^2}\dot{x}_l \\
=&\left(\frac{RTA^3}{(V_0+Ax_l)^2}\dot{m}-\frac{2mRTA^3}{(V_0+Ax_l)^3}\dot{x}_l\right)(x_m-x_l)+\frac{RTA}{V_0+Ax_l}\dot{m}-\frac{mRTA^2}{(V_0+Ax_l)^2}\dot{x}_l.
\end{aligned} \tag{3.16}$$

I assume that so long as the compression is small, the change of the fluid stiffness $\dot{k}_{fld}$ is small; the product of them is accordingly small. Then the derivative of the output force of the SEA system $\dot{F}_{l.SEA}$ can be approximated to that of the fluidic system $\dot{F}_l$. It could be concluded that a fluidic actuator controlled through flow by a servo valve can be modeled as a simple series elastic actuator (SEA) as presented above.

3.1.1 Driving-point impedance

To investigate the characteristics of fluidic actuation, I look into the driving-point impedance of the actuator, especially the open-loop impedance (I do not consider the effect of the motor command for now). As discussed above, fluidic actuation can be equivalent to series elastic actuation. As exhibited in Fig. 3.4, while position x_m is in control of an actuator of inertia M based on motor command F_m, position x_l determines the extension of a spring of stiffness k between the actuator and end-effector. I assume that the end-effector inertia is 0 at this moment. In practice, the end-effector inertia would appear to be dominant at high frequencies. As long as the end-effector inertia is small relative to the actuator inertia, the frequency at which its effect appears would be high. I express the external force F_e as the product of stiffness k and the compression of the spring in the frequency domain:

$$F_e = k(X_m(s) - X_l(s)). \tag{3.17}$$

With the expression for $X_m(s)$ obtained from the actuator dynamics

$$(Ms^2 + Bs)X_m(s) = F_m - F_e, \tag{3.18}$$

where B denotes viscosity of the actuator (not shown in Fig. 3.4),

Eq.(3.17) is reexpressed as

$$F_e = k(\frac{F_m - F_e}{Ms^2 + Bs} - X_l(s)) = \frac{k}{Ms^2 + Bs + k}F_m - \frac{k(Ms^2 + Bs)}{Ms^2 + Bs + k}X_l(s). \quad (3.19)$$

The driving-point impedance is defined as the displacement of the piston x_l at the effector against the external force F_e exerted on the piston. That is, the definition is,

$$Z \triangleq \frac{F_e(s)}{X_l(s)}. \quad (3.20)$$

Finally, I reach the open-loop impedance by setting $F_m = 0$ in impedance Z (the actuator is turned off)

$$Z_{OL} = -\frac{k(Ms^2 + Bs)}{Ms^2 + Bs + k}. \quad (3.21)$$

Note that impedance Z_{OL} is near 0 at low frequencies $s \to 0$, whereas the impedance saturates to k at high frequencies ($s \to \infty$).

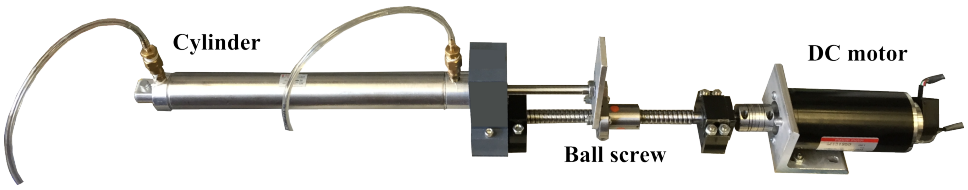

Figure 3.6: Driving part of a pneumatic system.

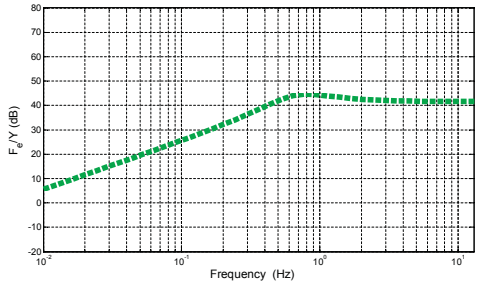

Figure 3.7: Simulation results of the open-loop impedance of a pneumatic system.

Further, numerical and experimental examination on impendence is conducted with a physical pneumatic system consisting of two custom cylinders. The driving part is composed of an Aircylinder RLF10A-DAP-NA00 1.5in bore double acting cylinder (Norgren® , Brookville OH) and this cylinder is actuated through a 5 mm pitch ball screw by a Maxon RE65 motor, as shown in Fig. 3.6. The driven cylinder

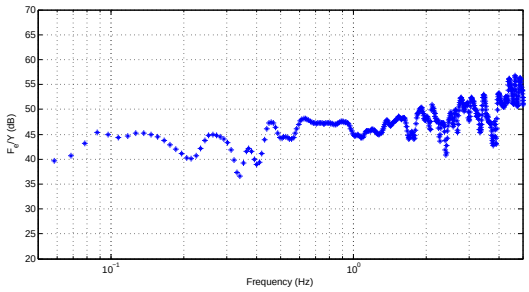

Figure 3.8: Experimental results of the open-loop impedance of a pneumatic system.

is an Airpel E16D5.0U 16 mm bore antistiction double acting cylinder (Airpot Corp., Norwalk CT). The mass M is an equivalent mass representing the lumped mass of the cylinder rod, items that translate, and the moment of inertia of the motor, ball screw and other items. Mass M is estimated as 6.56 kg. And viscosity B and stiffness k are assumed to be 30 Ns/m and 120 N/m for simulation, respectively. Note that the stiffness is assumed constant. Fig. 3.7 shows numerical results of the driving-point impedance. As Eq.(3.21) indicates, as frequency approaches 0, the impedance approaches 0 as well. The rate of the impedance in this frequency range is 40 dB/decade (the impedance is regarded as a mass $Z_O L = Ms^2$). The end-effector is decoupled from the actuator dynamics except this mass. At high frequencies, the impedance stays at $20\log k$ (≈ 41.6) dB, meaning that the high-frequency behavior of the pneumatic system is that of a spring. Shock loads and other high frequency forces are filtered by the elasticity. Fig. 3.8 shows numerical results of the driving-point impedance. As frequency increases, the open-loop impedance converges to a value corresponding closely to an experimentally identified stiffness $k = 120$ N/m. Since the dynamics of the driving part involving M and B has a high impedance (the device is stationary), the impedance magnitude is seen relatively flat even at low frequencies. Also, in opposition to the numerical prediction, the impedance diverges at high frequencies mainly due to a small mass at the end-effector not accounted for in the model.

3.2 Design of backdriveable actuators

So far, I have explored the advantages of actuation with compressible fluid. Fluid actuation can be realized employing custom cylinders. But in this thesis, I present several actuators designed with backdriveability in mind that employ pneumatics for active control. As mentioned in the Introduction, soft robotics is a burgeoning field and promises to replace hard robotics in many applications because of its inherent

low impedance and safety. Riding on the surge of interest in soft robotics, I present several soft actuators. Featured among these is the Origami Structured Compliant Actuator (OSCA) that makes up for certain weaknesses in soft robotic actuators.

3.2.1 Soft actuators

In soft robotics, robots are typically created out of elastomeric materials. If an elastomeric chamber is air-tight, it can be expanded and contracted based on the pressure inside. By outfitting various areas of the otherwise extensible surface of the actuator with inextensible fiber or fabric, various motions like bending, stretching, or twisting can be achieved. The representative examples are McKibben actuators and the Fiber Reinforced Elastomeric Enclosures (FREEs) presented in [9, 67].

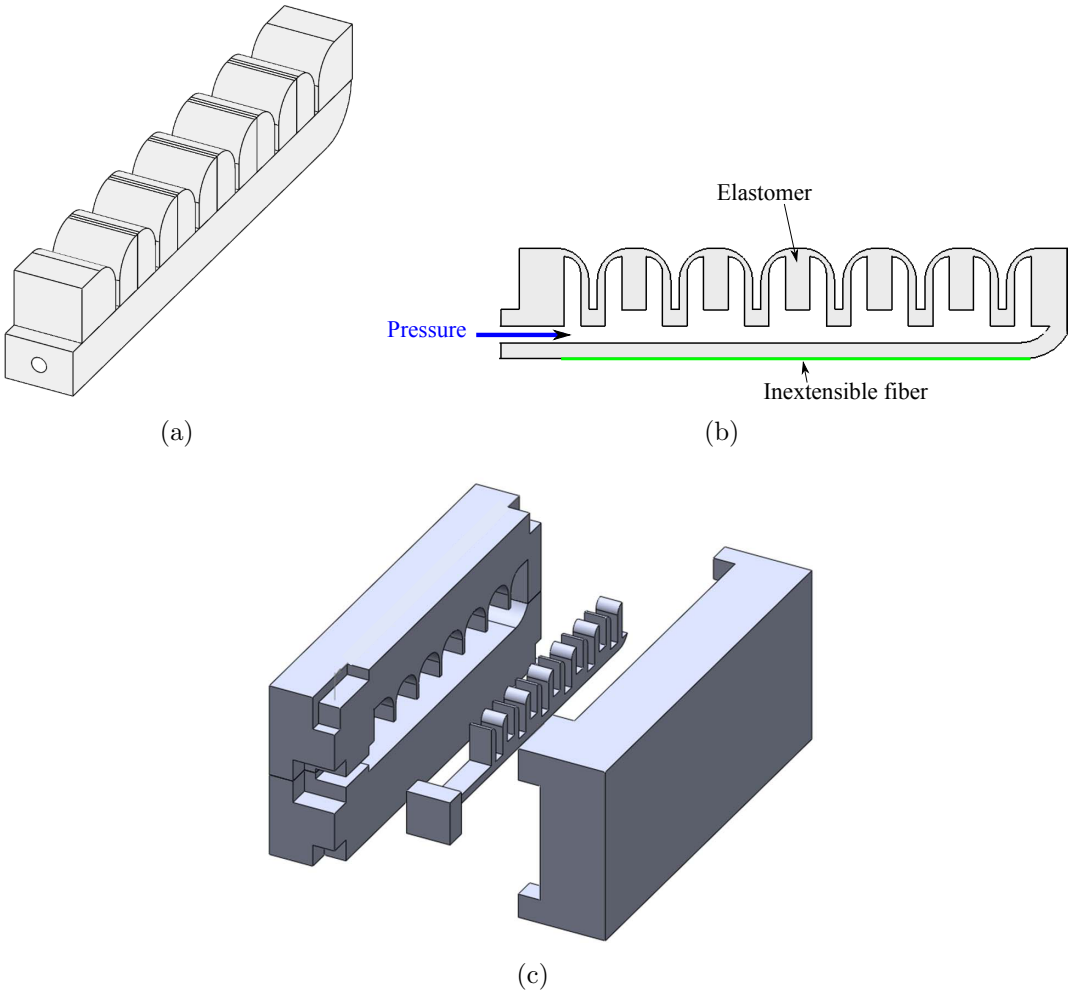

Figure 3.9: (a) The trimetric view and (b) side view of a bending actuator design using an elastomeric material, and (c) the CAD rendering of the mold.

Figure 3.10: Bending motions when pressured.

Actuator A

Fig. 3.9 presents a bending actuator made of an elastomer material for the purpose of motor rehabilitation. Our body joints typically produce extension and flexion. The bending actuator can help produce flexion about a paralyzed or impaired joint. The actuator has multiple chambers on its top side, while it has a piece of inextensible fabric on its bottom surface that restricts expansion of the surface. It is a similar structure to the actuator presented in [89]. The actuator is molded in a 3D-printed ABS plastic mold using an elastomer, Ecoflex® (00-30, Smooth-On, Inc., tensile modulus of 69 kPa), as exhibited in Fig. 3.13(a). Then, a piece of inextensible fabric is bonded to the bottom side using Ecoflex® again. Fig. 3.10 shows snap-shots of the actuator under various pressures.

This kind of actuator, however, requires a portion of supplied power to expand the elastic material. This supplied power is stored in the actuator and not imposed on the environment (or a human who wears the device). Also, energy supplied may be wasted on expansion in off-axis directions.

Actuator B

To increase the energy efficiency, the elastomeric material can be replaced with materials that do not store energy. Inextensible but flexible materials such as vinyl are good candidates. Fig. 3.11 shows schematics of a bending actuator that consists of a frame and an inextensible yet flexible (compliant in bending) cover. The cover allows the frame for expansion to bend toward one direction but it still contains fluid (extension on the bottom side is restricted). The membranes that form multiple chambers inside the hose play a role in enlarging the area to be fluid forced in in the on-axis direction versus that in the off-axis direction in a chamber. This idea is for promoting bending motion in the on-axis direction. The hole on a membrane is for aeration between chambers.

This actuator stores less energy relative to elastomeric actuators. This actuator also can reduce energy loss to expansion in off-axis directions.

I manufactured this bending actuator using hose. With vinyl, the hose increases

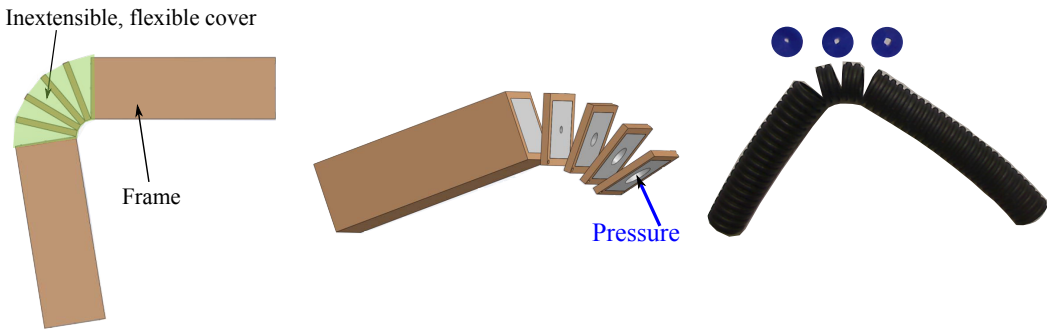

(a) (b) (c)

Figure 3.11: (a), (b) Schematics of a bending actuator design with inextensible and flexible materials, and (c) an actuator made with vinyl hose.

Figure 3.12: Bending motions when pressured.

flexibility toward one direction. Rubber membranes are injected into the inside hose to form multiple chambers. Bending is produced in the hose when extension on one side is restricted by an inextensible fiber. Fig. 3.12 shows snap-shots of the actuator under various applied pressures.

Actuator C

Another type of actuator designed constrains expansion in off-axis directions and guides fluid expansion into the target motion. One example is a pneumatic rotary transmission with multiple air chambers, presented in Fig. 3.13. The frames of 10 cm outer diameter, along with a pair of "cup" and "cap" frames, were CAD drawn and 3D printed out of ABS plastic. Each of the cup and cap frames has three walls with an angle of 120 degrees between them in the radial direction. A ball bearing enables these frames to rotate against each other. A total of six air silicone-rubber bellows-type chambers (Ecoflex® 00-30, Smooth-On, Inc., tensile modulus of 69 kPa) were created using 3D-printed ABS plastic molds. The bellows-type design allows the chambers to expand their volumes without requiring extension on the surfaces. Half of the chambers generate a clockwise moment, whereas the other half creates a counter-clockwise moment. Guiding the chamber expansion enables the mechanical

work supplied to be used in the work imposed on the environment, as long as the air chambers do not spend energy in expansion.

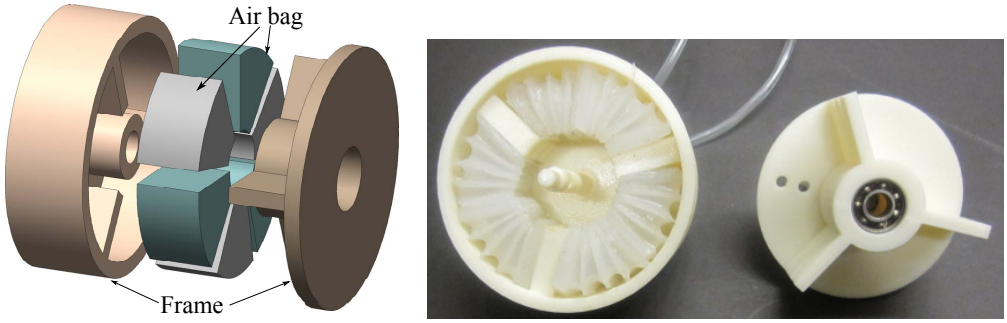

(a) (b)

Figure 3.13: (a) Schematic and (b) a picture of pneumatic rotary transmission.

3.2.2 OSCA

The OSCA features a chamber surrounded with rigid faces connected through hinges. The actuator does not store energy as elastic energy as the actuator moves. The rigid faces guide the expansion of fluid. This design compensates for the weakness of soft actuators in that expansion in off-axis directions is in fact converted to useful on-axis forces or torques. The OSCA utilizes a kinematic singularity that gives rise to a significant mechanical advantage over certain ranges of motion.

Rigid chamber in 2 Dimensions

To gain insight into the advantages of combining soft bending actuators with rigid plates, we undertake a comparative study using simple 2D models. Fig. 3.14 presents a pair of 2D models which may be considered cross-sections of 3D chambers. The upper model features two plates connected along their bottom edge by a hinge with an elastomeric material functioning as a cap. The lower model features the same two hinge-connected plates to either side but these are hinge-connected to two additional smaller plates that create a top cap. The hinges may be realized with compliant material or pin-bushings.

Considering for now only the effect of fluid pressure in the plane of the cross section, pressure on the side plates produces a moment about the lowest hinge joint in both models. Pressure against the elastomeric cap in the upper model, however, only produces expansion in off-axis directions and little or negative moment about the lowest hinge. Fluid pressure on the cap of two hinged plates in the lower model produces a change in configuration of what might be considered a four-bar mechanism,

converting upward pressure into outward moment about the lowest hinge until the two cap plates are co-planar. The configuration in which the two cap plates are co-planar is a singularity in the mechanism.

The plates making up the cap in the lower model in fact transmit compressive loads to the side plates, something that is not possible in a thin-walled elastomeric structure.

The contribution of the top plates to the expansion moment about the lowest hinge can be quantified in a simple kinetostatic model. Neglecting unbalanced loads and assuming that the pressure is uniformly distributed inside the chamber, we may consider only motions that maintain symmetry about the vertical centerline, as depicted in Fig. 3.15. Link 1 models a side plate and link 2 models one of the two cap plates. Link 2 is pin-connected to a slider whose motion is constrained to the centerline. The angles ϕ_A and ϕ_C depicted in Fig. 3.15 may be expressed as functions of the half-angle θ that describes expansion about the bottom hinge B (the actuator's bending angle):

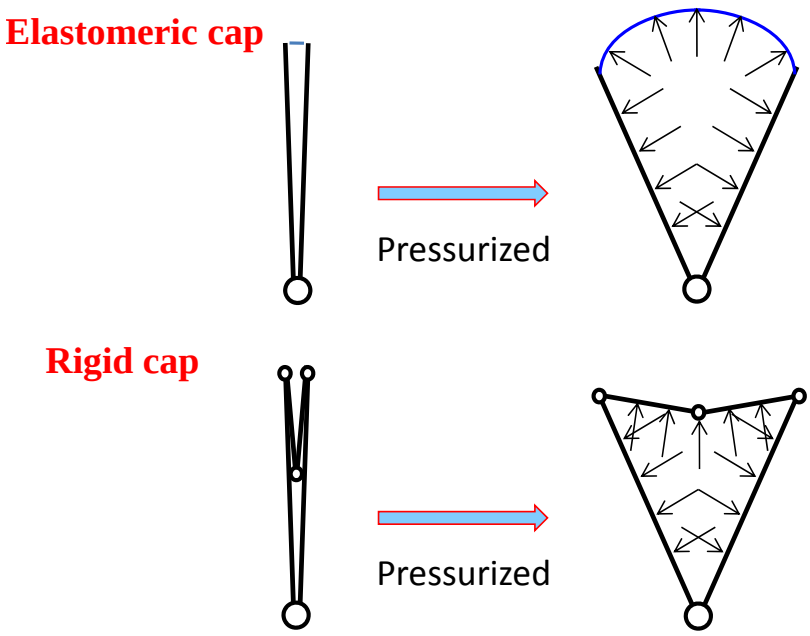

Figure 3.14: Elastomeric chamber and rigid chamber.

$$\phi_A = s^{-1}(\frac{as\theta}{b}), \quad (\phi_A \geq \frac{\pi}{2}) \tag{3.22}$$

$$\phi_C = \pi - \theta - \phi_A, \tag{3.23}$$

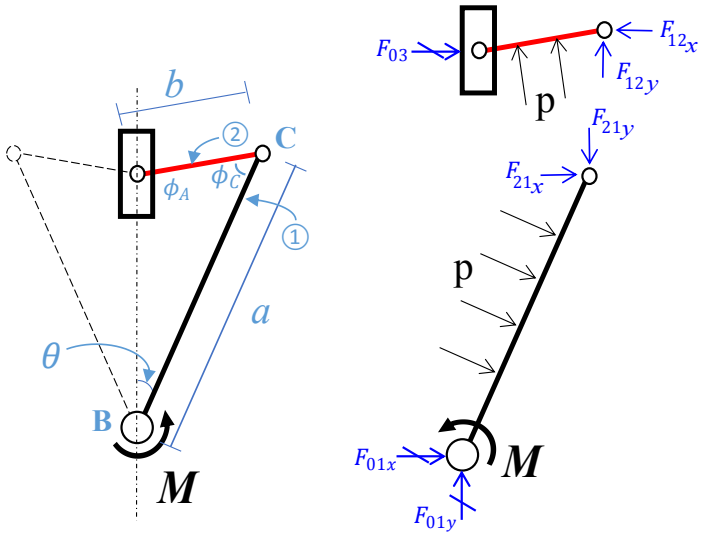

Figure 3.15: Free body diagram of half of a rigid chamber.

$s\theta$ denotes $\sin\theta$, $c\phi_A$ denotes $\cos\phi_A$ and so on.

An analysis enforcing static equilibrium produces the following expression for $M(\theta)$:

$$M(\theta) = \frac{pa^2}{2} + pab\Big(- s\phi_A s\theta - \frac{s^2\phi_A c\theta}{c\phi_A} + \frac{c\theta}{2c\phi_A}\Big), \tag{3.24}$$

where p denotes the pressure injected into the chamber.

The moment M in (3.24) can be expressed as, using the definition G,

$$M = Gp, \tag{3.25}$$

where $G \triangleq \frac{a^2}{2} + ab(\frac{c\theta}{2c\phi_A} - s\phi_A s\theta - \frac{s^2\phi_A c\theta}{c\phi_A})$.

The moment is related with the pressure in the chamber, defining G.

Equation (3.24) expresses the output moment $M(\theta)$ as a sum of four terms: the first term is a moment contributed by pressure acting on link 1 while the remaining terms capture the contribution of pressure acting on link 2 pushing link 1 outward while the chamber is inflated. The singular configuration is evident in that the expression for F_{03} approaches infinity as ϕ_A approaches 90^o.

Plots of the moment output considering various ratios of the lengths a and b of the the side and top plates are presented in Fig. 3.16. We set the pressure p and length a to be 1 and 2 with the appropriate units,

respectively. The blue solid area applicable regardless of the $a : b$ ratio indicates

the contribution of the side plates. The red shaded area above the blue area indicates the moment contributed by link 1 and thus the advantage of the upper cap plates. The chamber with the elastomeric cap lacks this advantage. We would predict that chambers with elastomeric or film caps generate smaller moments than the moment produced by the side plate (link 1). Further, elastomeric caps can begin to pull the side walls inward when sufficiently expanded, thereby counteracting the moment produced by the side plates.

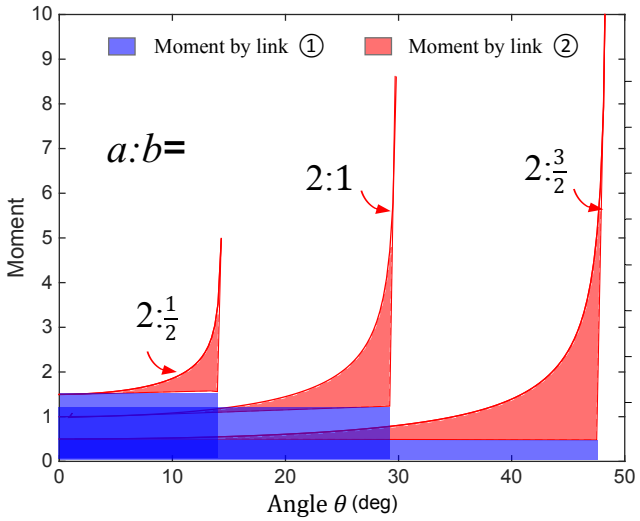

Figure 3.16: Moment generated by half of the rigid chamber with ratios of $a : b = 2{:}\frac{1}{2}$, 2:1, and $2{:}\frac{3}{2}$.

Let us calculate the volume of the chamber. We have the volume of half of the chamber as

$$V = \frac{1}{2} abs\phi_C. \tag{3.26}$$

Differentiating volume V with respect to time leads to

$$
\begin{aligned}
\frac{dV}{dt} =& \frac{a^2 b}{2} c\phi_C \dot{\phi}_C \\
=& = \frac{a^2 b}{2} c(\pi - \theta - \phi_A)(-\dot{\theta} - \dot{\phi}_A) \\
=& \frac{ab}{2} c(\theta + \phi_A)(\dot{\theta} + \dot{\phi}_A) \\
=& \frac{ab}{2} c(\theta + \phi_A)\left(\dot{\theta} + \frac{d}{dt}\big(s^{-1}(\frac{as\theta}{b})\big)\right) \\
=& \frac{ab}{2}(c\theta c\phi_A - s\theta s\phi_A)(\dot{\theta} + \frac{a}{b}\frac{c\theta}{c\phi_A}\dot{\theta}) \\
=& \frac{ab}{2}(c\theta c\phi_A + \frac{a}{b}c^2\theta - \frac{a}{b}s^2\theta - \frac{a^2}{b^2}\frac{s^2\theta.c\theta}{c\phi_A})\dot{\theta} \\
=& \frac{ab}{2}(c\theta c\phi_A + \frac{a}{b} - \frac{2a}{b}s^2\theta - \frac{a^2}{b^2}\frac{s^2\theta c\theta}{c\phi_A})\dot{\theta} \\
=& \big(\frac{a^2}{2} + \frac{ab}{2}(c\theta c\phi_A - \frac{2a}{b}s^2\theta - \frac{a^2}{b^2}\frac{s^2\theta c\theta}{c\phi_A})\big)\dot{\theta}. \qquad (3.27)
\end{aligned}
$$

With the relationships $s\theta = bs\phi_A/a$ and $s^2\phi_A + c^2\phi_A = 1$, we further rearrange $\dot{V}$ as

$$
\frac{dV}{dt} = \big(\frac{a^2}{2} + ab(\frac{c\theta}{2c\phi_A} - s\phi_A s\theta - \frac{s^2\phi_A c\theta}{c\phi_A})\big)\dot{\theta}. \qquad (3.28)
$$

I note that the relationship between the change of the volume and the rate of the opening angle, using G, defined in (3.25), as

$$
\dot{V} = G\dot{\theta}. \qquad (3.29)
$$

This analogy of the relationships between moment and pressure and between the change of the volume and the rate of the opening angle originates from the fact that the power is conserved. That is, the fluidic power is converted into the mechanical power as follows:

$$
\dot{V}p = G\dot{\theta}p = Gp\dot{\theta} = M\dot{\theta}. \qquad (3.30)
$$

Chamber with rigid origami structure

Now it is time to convert the rigid structure developed in 2D into a 3D chamber. Side plates composed of fold-able plates are required to close both sides of the chamber. The science of Rigid Origami considers 3D structures that may be created by folding

paper or other materials at fixed creases without bending or otherwise deforming the material between the creases. Thus all the faces are rigid and remain remain rigid while flexing the creases. I have designed side plates based on the reverse fold [28]. Unfortunately, it is impossible to construct a 3D structure with rigid faces and flexible hinges that is entirely closed in volume according to the following theorem previously known as the *Bellows theorem* [19].

The Bellows Theorem *The volume of a polyhedron remains constant under flexing.*

This theorem suggests that an articulated rigid origami structure cannot be fully closed; the structure must include slits or must include certain faces that are flexible. We have designed two types of origami-structured actuators, as depicted in CAD renderings in Fig. 3.17. Actuator I is a structure with slits. In this design an air bag is tailored to fit inside the origami structure so that fluid is entrapped. The top plates (named Plate B) are fashioned as trapezoids so as to not touch the side plates (Plate Cs) at the folded state, thereby accommodating a wider range of bending motion, as shown in Fig. 3.18. In addition, certain edges are filleted to protect the air bag inside. Actuator II has flexible faces included in the side plates. A flexible material such as Mylar is applied to create all the hinge edges as well as the flexible faces. For convenience in manufacturing, Actuator II was produced from plastic material using a 3D printer with thin breakable walls initially linking adjacent rigid faces or plates. The breakable walls are taped with a flexible material before being broken free.

Moment generation advantage

The kinetostatic analysis in 2D presented above may be extended to 3D. I analyze the moment generated by the prototype designs of the proposed actuators to evaluate their advantages. I quantify the moments with and without top and side plates to evaluate the various contributions to the actuator output moment. Again I may consider half of the actuator design for simplicity, considering symmetry, as shown in Fig. 3.18.

Concentrated forces are depicted instead of distributed forces applied to each plate. I compute moments as a function of the angle θ between the vertical plane and the side plate. Firstly, the relationships between the angle θ and the dihedral angles $\phi_{0C2}, \phi_{0B}, \phi_{AC2}$, ϕ_{AB}, and the angle θ_{0C2} may be described using:

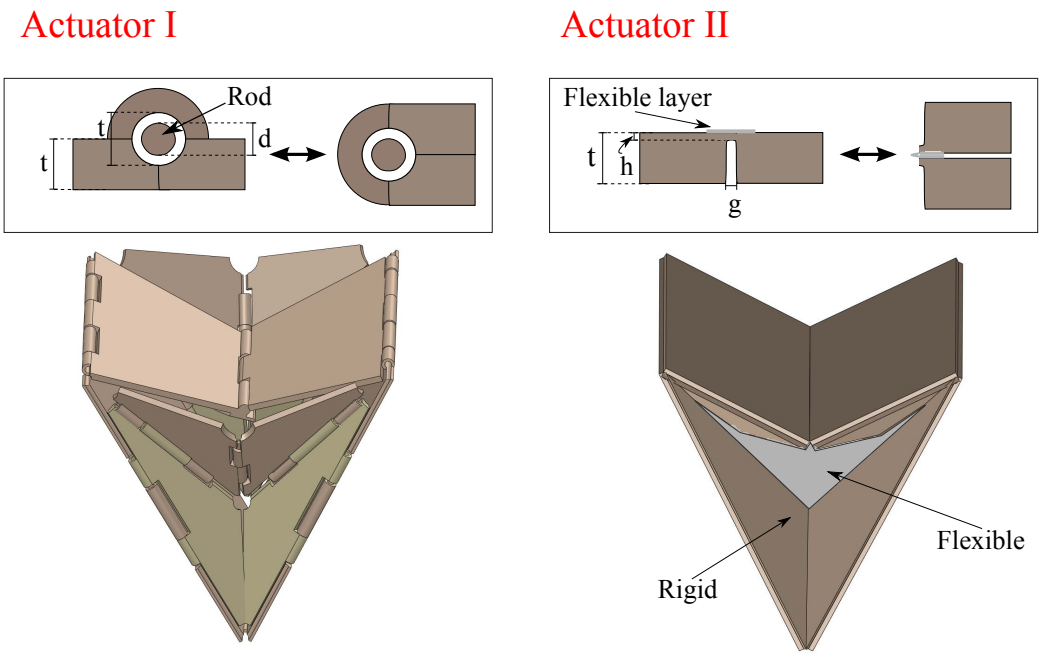

Figure 3.17: CAD renderings of two types of rigid origami structure and the side views of their hinge joints for a bending actuator. t: thickness of the rigid plate, d: diameter of a rod, h: thickness of a thin layer at a hinge edge between rigid plates, g: gap between rigid plates at a hinge edge.

$$\phi_{0C2} = s^{-1}(\frac{as\theta}{b}), (\leq \frac{\pi}{2}), \tag{3.31}$$

$$\phi_{0B} = s^{-1}(\frac{as\theta}{b}), (\geq \frac{\pi}{2}), \tag{3.32}$$

$$\phi_{AC2} = s^{-1}(\frac{as\theta}{b}), (\leq \frac{\pi}{2}), \tag{3.33}$$

$$\phi_{AB} = \pi - \theta - s^{-1}(\frac{as\theta}{b}), \tag{3.34}$$

$$\theta_{0C2} = c^{-1}\frac{\sqrt{a^2-b^2}}{a} - c^{-1}\big(a(1-(\frac{a}{b}-\frac{\sqrt{a^2-b^2}}{b})s\theta)\big). \tag{3.35}$$

Next, I carry out a static force analysis, neglecting the effects of the weights and accelerations of the plates during actuation. Plate C1 (shown in Fig. 3.18) is excluded considering that the force transmission of Plate C1 from the force led by the supplied pressure to the resultant moment is negligible. Rather, Plate C1 has a role of compressing the air bag as the actuator approaches its fully unfolded state. In a similar way to the 2D structure, a static force analysis gives the following resultant moment that is generated by half of the Actuator I as

$$M(\theta) = \frac{a}{2}F_A + aF_B\Big(- s\phi_{0B}s\theta - \frac{s^2\phi_{0B}c\theta}{c\phi_{0B}} + \frac{c\theta}{2c\phi_{0B}}\Big)$$
$$+ 2\frac{a}{2}F_{C2}\left(\frac{\frac{2}{3} + c\phi_{AC2}s\phi_{0C2}s\theta_{0C2}s\theta}{c\phi_{0C2}}s\phi_{AB} + c\phi_{AC2}s^2\theta\right). \tag{3.36}$$

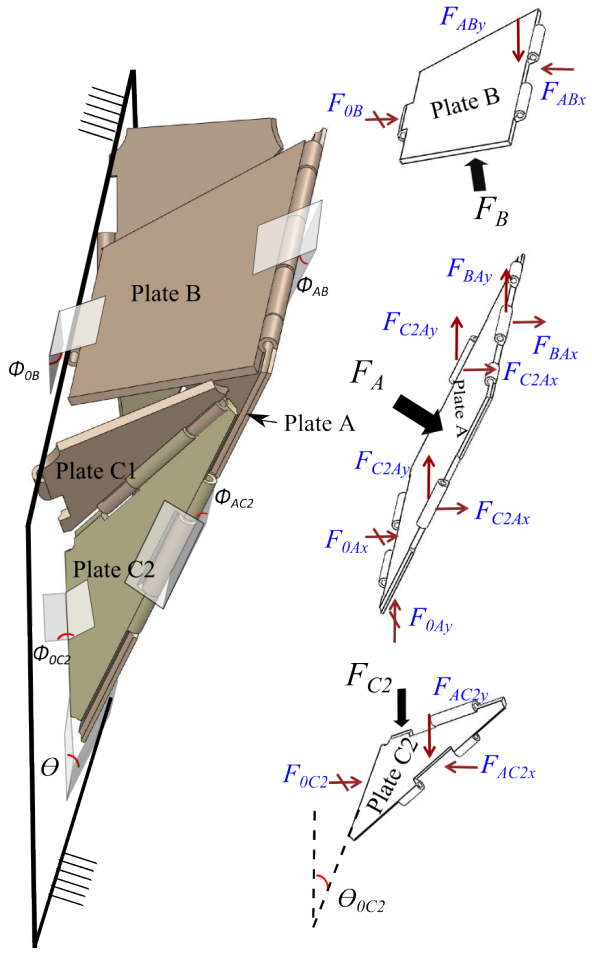

Figure 3.18: Free body diagram of half of Actuator I. Black thick arrows indicate concentrated forces which are generated by air pressure; black thin arrows indicate forces that are applied between two rigid plates. The symbol θ denotes the angle between the vertical plane and Plate A; θ_{0C2} denotes the angle between the line of Plate C2 contacting with the vertical plane and vertical line; ϕs denote dihedral angles between plates or between the vertical plane and plates.

Note that half of the bending OSCA has two Plate C2s (on the left and right sides). This obtained moment is applicable to Actuator II as well. The moment $M(\theta)$ is the summation of the three components: a moment by Plate A, a moment by Plate B that pushes Plate A, and a moment by Plate C2 that pushes Plate A while

the actuator is inflated. Plots of the moment outputs with several ratios between Plate A length a and the Plate B length b are presented in Fig. 3.19. The length a is set at 2 units. I simply calculated F_A, F_B, F_{C2} as pa^2, pab, and $pab/4$, respectively, where p is the input pressure which is selected as 1 unit of pressure. The first thing to note is, as with 2D rigid chamber (Fig. 3.16), the singularity effect is also apparent in the 3D case. The singularity is approached when Plate B and Plate C2 become coplanar with those of the other side of the actuator structure. Fig. 3.19 shows the proportion between the contributions of each plate to the resultant moment. Plate B has a more significant effect in increasing the moment than the two Plate C2s (left and right). Without Plate B and Plate C2s, we would predict that the moment falls down to the blue area in the graph Fig. 3.19.

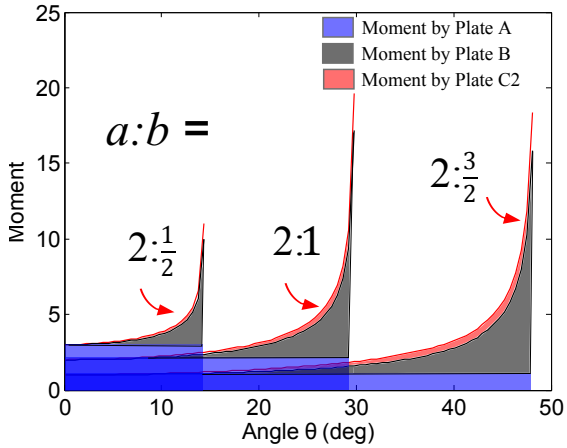

Figure 3.19: Moment generated by half of the bending OSCA with ratios of $a : b = 2{:}\frac{1}{2}$, 2:1, and $2{:}\frac{3}{2}$. The values are stacked in an order of moments by Plate A, Plate B and two Plate C2s (left and right)

Experimental validation

To validate the design and models of the OSCA bending actuator, CAD models of the two types of rigid structures (Actuator I, Actuator II) in Fig. 3.17 were 3D printed out of ABS plastic. Also, I printed two structures with Plate A length a versus Plate B length b of 10:5 and 10:7.5 in cm, respectively, for each type. The design parameters depicted in Fig. 3.17 were set as t=2 mm, d=1.8 mm, h=0.2 mm, and g=0.2 mm. Air bags were created using Mylar with a thickness of 0.05 mm which were tailored to the inside shape of Actuator I. Also, I used the Mylar for the flexible faces of Actuator II and to coat the thin layers by which the hinge edges were realized. Fig. 3.21A shows pictures of the two prototypes of Actuator I. To evaluate the performance of the bending OSCA in terms of the moment versus the opening

angle, a sensing apparatus was equipped with a 5-kg rated beam load cell (Transducer Techniques LSP-5) and an optical encoder (US Digital EM1-1-1250) (see Fig. 3.21B). Since the rotation axes of the sensing device and actuators were not exactly aligned, the moment and motion of actuators were obtained through additional computation. The supplied pressure was controlled by an electro-pneumatic proportional regulator (SMC ITV0010-3BL). Control of the regulator and data acquisition were carried out using a Sensoray 626 PCI card installed in a PC running Matlab R2013a Real-Time Windows Target. Fig. 3.20 illustrates the experimental setup.

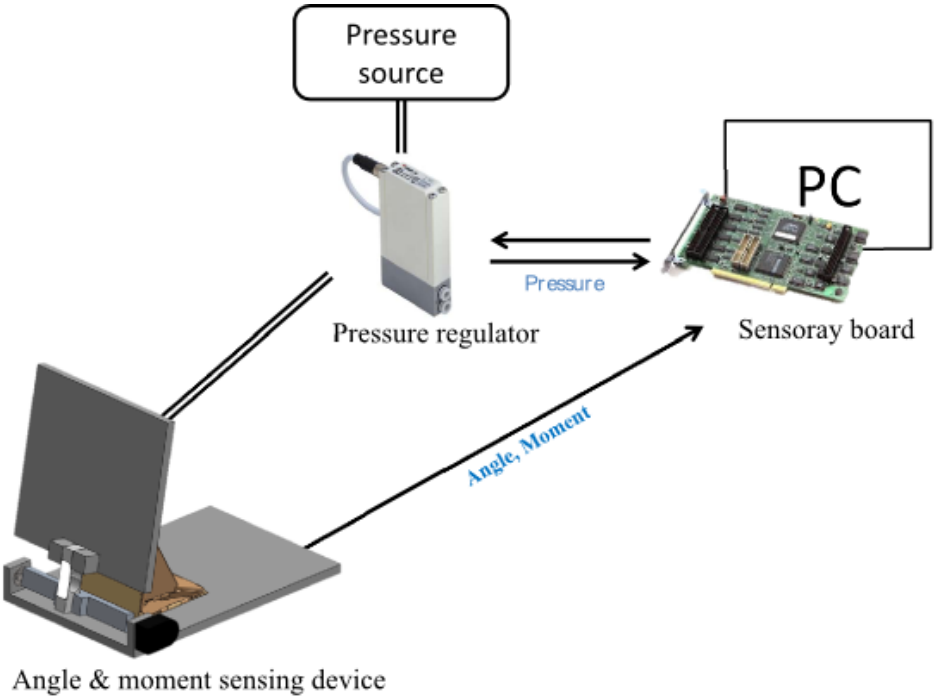

Figure 3.20: Experimental setup.

Fig. 3.22 shows the moment of the Actuator I prototype with a ratio of $a : b =$ 2:1 under a pressure of 0.1 Mpa. I investigated the contribution of each plate to the resultant moment of the actuator: the moments when inflating the Mylar air bag with only Plate C2s, with Plate C2s and Plate Bs, and with all plates (including end plates), respectively. Note that with Plate B, the actuator did not open beyond 60 degrees where the actuator was fully unfolded as I limited the range of the hinges mechanically. The actuator with only Plate As opened beyond 60 degrees to the state where the air bag was fully expanded. The experiment result is in good agreement with the numerical prediction (Fig. 3.19). I see a sharp increase in moment as the opening angle approaches 60 degrees in the case including Plate Bs and case including Plate B and end plates. This increase is due to the singularity in the OSCA design.

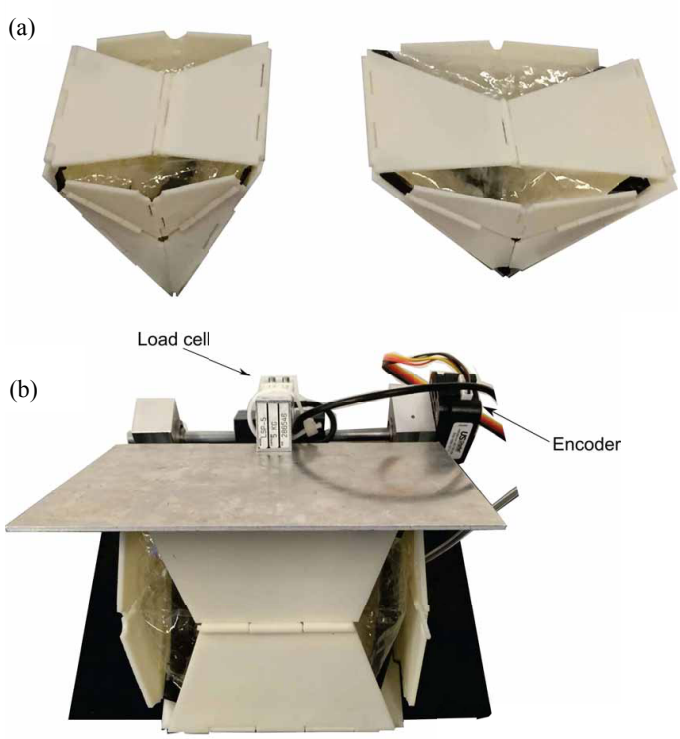

Figure 3.21: Two prototypes of Actuator I with Mylar airbags inside (a) and measurement of the moment of the prototype versus the opening angle (b).

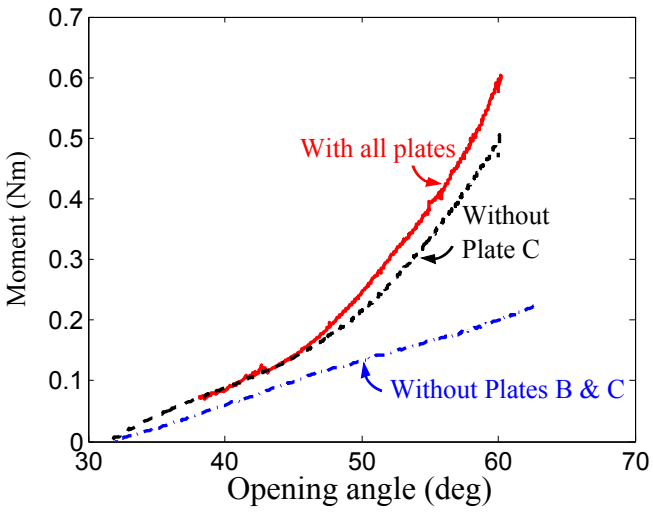

Figure 3.22: Proportion of the moment generated by an Actuator I prototype with a ratio of $a : b = 2{:}1$.

The Mylar air bag in the case of the actuator without Plate B first expanded outward before pushing the side plates in the desired direction. This led to a longer time to reach a given opening angle.

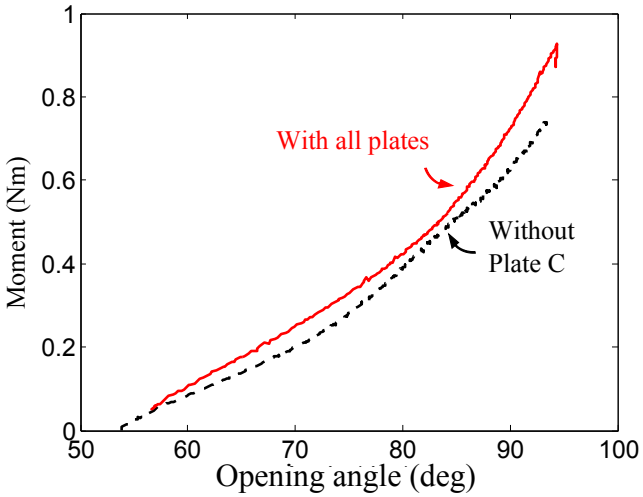

Figure 3.23: Proportion of the moment generated by an Actuator I prototype with a ratio of $a : b = 2{:}\frac{3}{2}$.

Fig. 3.23 shows the moment of another prototype with a ratio of $a : b = 2{:}\frac{3}{2}$, which has a wider range of working angle. It is revealed that this OSCA, which is surrounded by all plates, creates a higher moment than when it is with only Plate Bs but the contribution of Plate Bs to the output is significant. Both the cases exhibit the singularity advantage. Without even Plate Bs, the actuator cannot generate positive output all the way due to the predominant expansion in off-axis directions (not shown in the graph).

Application I

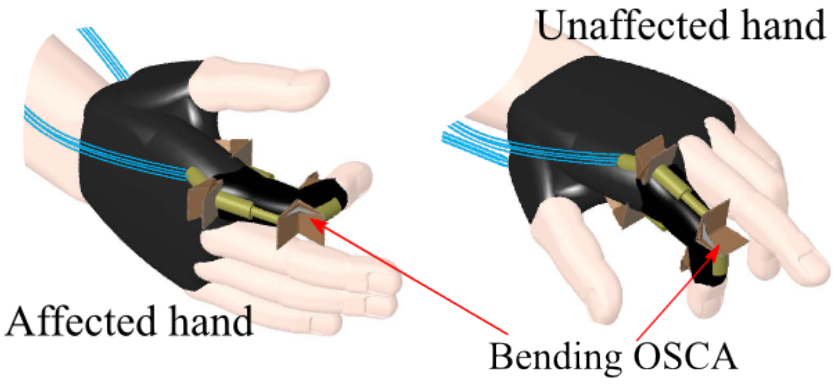

Figure 3.24: Use of bending OSCAs to transmit body power from the joints of an unaffected hand to the joints of a motor-impaired hand. The body-powered application demands a transmission and actuator design that transmits power with minimal loss and minimal elastic or inertial energy storage in a lightweight package.

OSCAs could be applicable to needs for compliant motions including robot manipulators and exoskeletons for rehabilitation. A target application is the transmission of body-power from the less affected joints of a person with neurological injury to their own affected or weaker joints. A passive exoskeleton that routes body power among joints would enable an individual to assist themselves. Regardless of the type of coupling, the user is in control of speed, power, and timing of motions. Exoskeletons incorporated with OSCA would attain portability, safety, and compliant backdriveability, all with the ability to scale assistance and maintain the engagement of the patient. Fig. 3.24 presents bending OSCAs designed for eventual use in body-powered hand rehabilitation. The bending actuators are designed to assist the expanding and flexing motions of the hand.

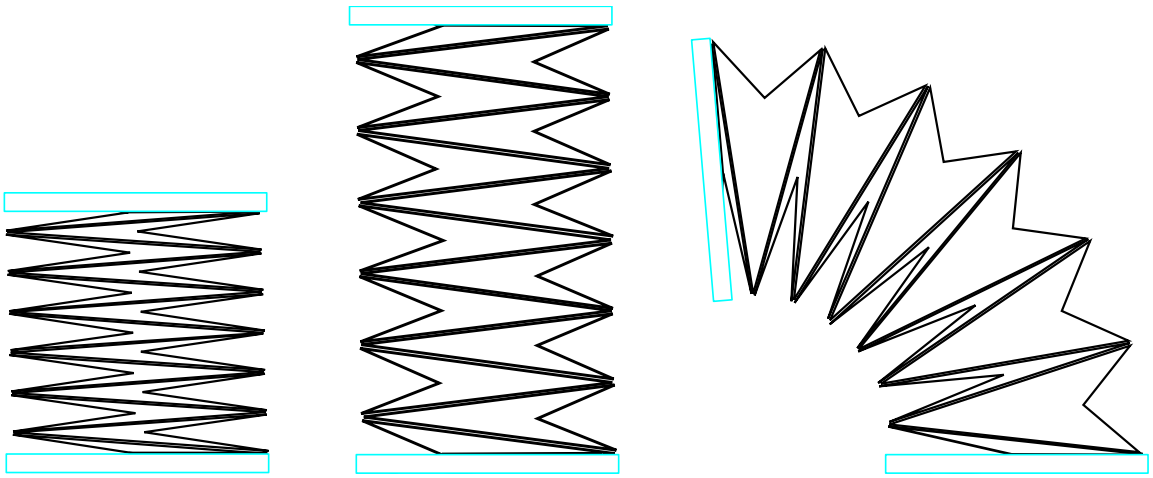

Figure 3.25: A schematic of an OSCA manipulator with OSCAs deployed in a zig-zag way.

Application II

A robot manipulator can be created by engaging an OSCA with the next repeatedly in a zig-zag way, sharing one face of each OSCA, as depicted in Fig. 3.25. The manipulator produces longitudinal expanding and bending motions according to the opening angle of each chamber which can be controlled by pressure sources. More independent pressure inputs leads to a larger variety of possible configurations; it makes possible positioning the end-effector to the same position with various postures of this highly redundant manipulator.

I consider a simple planar manipulator consisting of multiple OSCAs ($2n$) with only 2 pressure sources, as presented in Fig. 3.26. Each half of the $2n$ OSCAs (n) rotates α clockwise under the pressure input p_α, while each of the other half (n) rotates β counterclockwise under the pressure input p_β. The manipulator produces

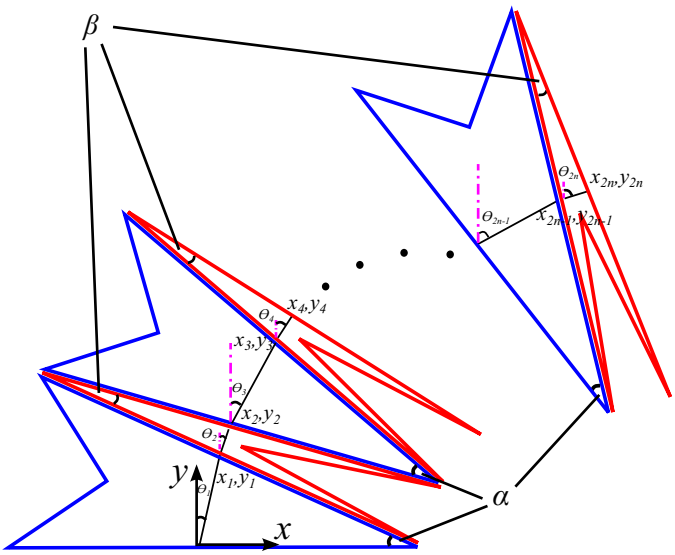

Figure 3.26: A schematic of an OSCA manipulator with $2n$ OSCAs and a mass at the end-effector controlled by 2 pressure sources.

planar motions depending on angles α and β. It is assumed that the end-effector (mass m_e) is placed at the middle of the plate of the outermost OSCA (x_{2n}, y_{2n}) and the inertias of the plates are negligible.

- Kinematics

I map angles α and β to point (x_{2n}, y_{2n}). The distances between the middle points of the plates that form angles α and β are calculated as

$$l_\alpha = \frac{asin\alpha}{2\sin\frac{\pi-\alpha}{2}} = asin\frac{\alpha}{2}, l_\beta = \frac{asin\beta}{2\sin\frac{\pi-\beta}{2}} = asin\frac{\beta}{2}, \tag{3.37}$$

where a is the length of plate.

Also, the angles of the lines connecting the middle points of the plates of each chamber versus the vertical lines are obtained as

$$\theta_1 = \frac{\alpha}{2}, \tag{3.38}$$

$$\theta_2 = \alpha - \frac{\beta}{2}, \tag{3.39}$$

$$\theta_3 = \alpha - \beta + \frac{\alpha}{2}, \tag{3.40}$$

$$\theta_4 = 2\alpha - \beta - \frac{\beta}{2}, \tag{3.41}$$

$$\vdots$$

$$\theta_{2n-1} = (n-1)(\alpha - \beta) + \frac{\alpha}{2}, \tag{3.42}$$

$$\theta_{2n} = n\alpha - (n-1)\beta - \frac{\beta}{2}. \tag{3.43}$$

Then I express points (x_{2n}, y_{2n}) in terms of angles α and β in turn as follows:

$$x_1 = l_\alpha sin\theta_1, y_1 = l_\alpha cos\theta_1, \tag{3.44}$$

$$x_2 = l_\beta sin\theta_2 + x_1, y_2 = l_\beta cos\theta_2 + y_1, \tag{3.45}$$

$$x_3 = l_\alpha sin\theta_3 + x_2, y_3 = l_\alpha cos\theta_3 + y_2, \tag{3.46}$$

$$x_4 = l_\beta sin\theta_4 + x_3, y_4 = l_\beta cos\theta_4 + y_3, \tag{3.47}$$

$$\vdots$$

$$x_{2n} = l_\beta sin\theta_{2n} + x_{2n-1}, y_{2n} = l_\beta cos\theta_{2n} + y_{2n-1}. \tag{3.48}$$

A more general form of position can be given as

$$\begin{aligned} x_{2n} &= l_\alpha \sum_{k=1}^{n} (sin\theta_{2k-1}) + l_\beta \sum_{k=1}^{n} (sin\theta_{2k}), \\ y_{2n} &= l_\alpha \sum_{k=1}^{n} (cos\theta_{2k-1}) + l_\beta \sum_{k=1}^{n} (cos\theta_{2k}). \end{aligned} \tag{3.49}$$

The velocity may be expressed as

$$\begin{aligned}
\dot{x}_{2n} =& \dot{l}_\alpha \sum_{k=1}^{n}(sin\theta_{2k-1}) + l_\alpha \sum_{k=1}^{n}((k-\frac{1}{2})cos\theta_{2k-1})\dot{\alpha} - l_\alpha \sum_{k=1}^{n}((k-1)cos\theta_{2k-1})\dot{\beta} \\
&+ \dot{l}_\beta \sum_{k=1}^{n}(sin\theta_{2k}) + l_\beta \sum_{k=1}^{n}(kcos\theta_{2k})\dot{\alpha} - l_\beta \sum_{k=1}^{n}((k-\frac{1}{2})cos\theta_{2k})\dot{\beta}, \\
\dot{y}_{2n} =& \dot{l}_\alpha \sum_{k=1}^{n}(cos\theta_{2k-1}) - l_\alpha \sum_{k=1}^{n}((k-\frac{1}{2})sin\theta_{2k-1})\dot{\alpha} + l_\alpha \sum_{k=1}^{n}((k-1)sin\theta_{2k-1})\dot{\beta} \\
&+ \dot{l}_\beta \sum_{k=1}^{n}(cos\theta_{2k}) - l_\beta \sum_{k=1}^{n}(ksin\theta_{2k})\dot{\alpha} + l_\beta \sum_{k=1}^{n}((k-\frac{1}{2})sin\theta_{2k})\dot{\beta}. \qquad (3.50)
\end{aligned}$$

Differentiating l_α, l_β in (3.37) with regard to time, I have $\dot{l}_\alpha$ and $\dot{l}_\beta$ as, respectively,

$$\dot{l}_\alpha = \frac{a}{2}cos\frac{\alpha}{2}\dot{\alpha}, \dot{l}_\beta = \frac{a}{2}cos\frac{\beta}{2}\dot{\beta}. \qquad (3.51)$$

Eq.(3.50) and Eq.(3.51) can be rearranged as follows after defining the Jacobian J that relates the opening angular velocities of chambers to the linear velocity of the end-effector:

$$\begin{bmatrix} \dot{x}_{2n} \\ \dot{y}_{2n} \end{bmatrix} = J \begin{bmatrix} \dot{\alpha} \\ \dot{\beta} \end{bmatrix},$$

where

$$J \triangleq \begin{bmatrix} j_{11} & j_{12} \\ j_{21} & j_{22} \end{bmatrix}, \qquad (3.52)$$

$$j_{11} = \frac{a}{2}cos\frac{\alpha}{2}\sum_{k=1}^{n}(sin\theta_{2k-1}) + l_\alpha \sum_{k=1}^{n}((k-\frac{1}{2})cos\theta_{2k-1}) + l_\beta \sum_{k=1}^{n}(kcos\theta_{2k}), \qquad (3.53)$$

$$j_{12} = \frac{a}{2} cos\frac{\beta}{2} \sum_{k=1}^{n} (sin\theta_{2k}) - l_\alpha \sum_{k=1}^{n} ((k-1)cos\theta_{2k-1}) - l_\beta \sum_{k=1}^{n} ((k-\frac{1}{2})cos\theta_{2k}), \quad (3.54)$$

$$j_{21} = \frac{a}{2} cos\frac{\alpha}{2} \sum_{k=1}^{n} (cos\theta_{2k-1}) - l_\alpha \sum_{k=1}^{n} ((k-\frac{1}{2})sin\theta_{2k-1}) - l_\beta \sum_{k=1}^{n} (ksin\theta_{2k}), \quad (3.55)$$

$$j_{22} = \frac{a}{2} cos\frac{\beta}{2} \sum_{k=1}^{n} (cos\theta_{2k}) + l_\alpha \sum_{k=1}^{n} ((k-1)sin\theta_{2k-1}) + l_\beta \sum_{k=1}^{n} ((k-\frac{1}{2})sin\theta_{2k}), \quad (3.56)$$

- Kinetics

Next, I proceed to the dynamics of the end-effector by the pressure inputs to the chambers. With the Lagrangian L defined considering the kinetic energy of the system,

$$L = \frac{m_e}{2}(x_{2n}^2 + y_{2n}^2), \quad (3.57)$$

the following two Euler-Lagrange equations describe the dynamics of the end-effector:

$$M_\alpha = \frac{d}{dt}\frac{dL}{d\dot{\alpha}} - \frac{dL}{d\alpha}, \quad (3.58)$$

$$M_\beta = \frac{d}{dt}\frac{dL}{d\dot{\beta}} - \frac{dL}{d\beta}, \quad (3.59)$$

where M_α, M_β denote torques generated by chambers with opening angles of α and β, respectively. Note that I do not elaborate and present the equations of motion here. The torques by chambers are produced by pressure inputs. The pressure inputs are calculated using (3.25) as follows:

$$p_\alpha = G^{-1}(\frac{\alpha}{2})M_\alpha, \quad (3.60)$$

$$p_\beta = G^{-1}(\frac{\beta}{2})M_\beta. \quad (3.61)$$

I conduct a simulation study in which the end-effector is loaded with 0.1 kg in a gravity field and driven to various target positions, investigating the resulting opening angles and pressures inside each group of OSCAs. I design a simple position controller that pushes the end-effector to a desired position (x_d, y_d) with virtual springs of stiffnesses K_x, K_y in the x-direction and y-direction, respectively. I do not focus on control performance in this position control. The products of stiffnesses K_x, K_y

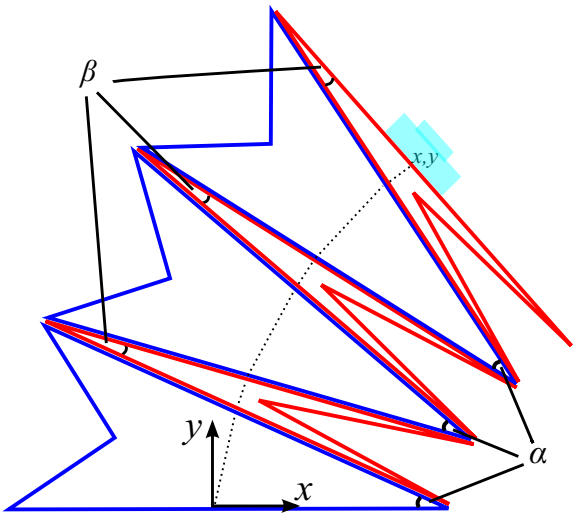

Figure 3.27: A schematic of an OSCA manipulator with 6 OSCAs controlled by 2 pressure sources.

and the difference between the desired and actual positions in each direction are the forces, defined as F_x, F_y, that the OSCA manipulator needs to generate. Using the Jacobian J in Eq. (3.52), moments M_α, M_β can be obtained from forces F_x, F_y. And the pressure inputs p_α, p_β are obtained using Eq. (3.61). A procedure of positioning the end-effector to the desired position is expressed in the following equations and depicted in Fig. 3.28.

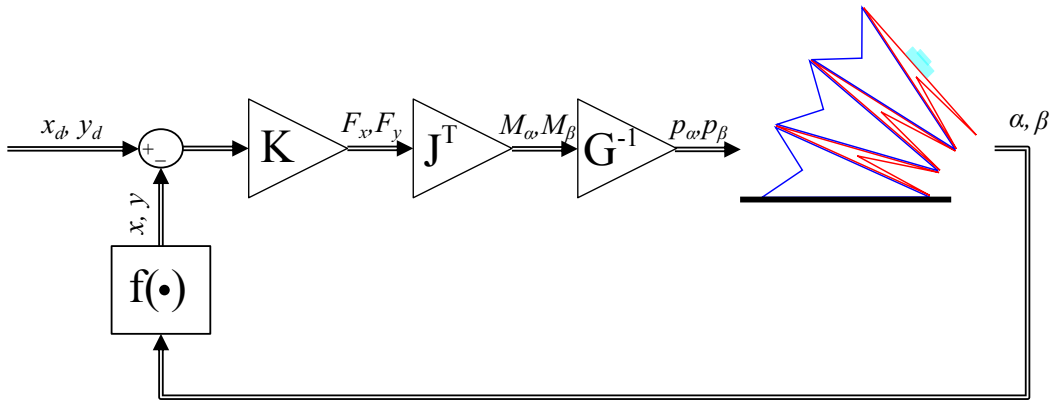

Figure 3.28: Position control of the OSCA manipulator with ideal pressure sources.

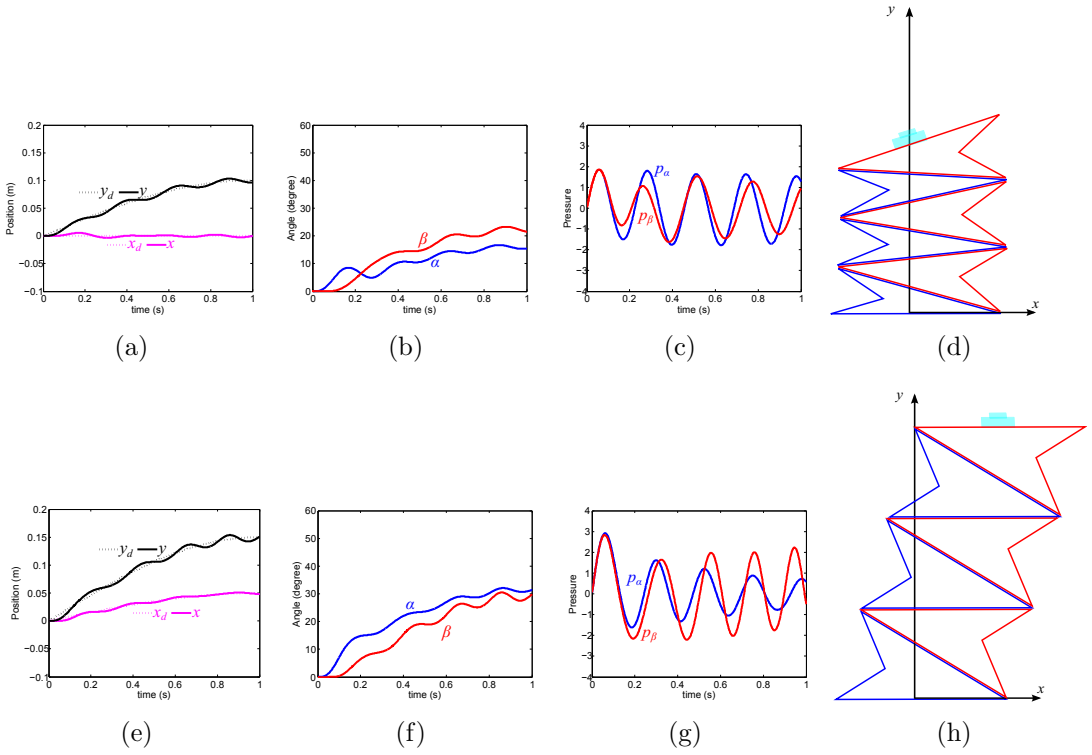

Figure 3.29: Positioning the end-effector and its accompanying opening angles and pressures inside each group of OSCAs: (a), (e) the end-effector position, (b), (f) the opening angle, (c), (g) the pressure, and (d), (h) a depiction of the end-effector positioned to the target positions.

$$\begin{bmatrix} F_x \\ F_y \end{bmatrix} = \begin{bmatrix} K_x(x_d - x) \\ F_y(y_d - y) \end{bmatrix}, \tag{3.62}$$

$$\begin{bmatrix} M_\alpha \\ M_\alpha \end{bmatrix} = J^T \begin{bmatrix} F_x \\ F_y \end{bmatrix}. \tag{3.63}$$

Fig. 3.29 presents the results with the desired positions $(0,\ 0.1\sin(2\pi t))$ and $(0.05\sin(2\pi t),\ 0.15\sin(2\pi t))$ for 1 second. The dimensions of the identical OSCAs a, b are set to 0.1 m and 0.03 m, respectively. The stiffnesses K_x, K_y are both set to 150. Integration is performed using ODE45 with time step 0.5 ms.

3.3 Control of backdriveable actuators

In this section, I present several control strategies for force control and impedance control of fluidic systems. One of the proposed force controllers decreases the driving-

point impedance while increasing the operational bandwidth. The proposed impedance controller cancels system dynamics without a precise system model.

3.3.1 Force control

Fluidic systems can be controlled by fluid flow through servo valves (Fig. 3.5). And I showed in Section 3.1 that fluidic actuation controlled by flow can be reduced to a SEA system (Fig. 3.5(b)). The dynamics of the servo valve that generates fluid flow rate Q based on a control current i, assumed as a first-order system, shall be described in the frequency domain as

$$Q(s) = \frac{K_v}{\tau_v s + 1} I(s), \tag{3.64}$$

where s is the Laplace variable; K_v a valve gain; τ_v a time constant.

Cylinder displacement X_m may be expressed in terms of fluid flow rate Q and control current I as follows:

$$X_m(s) = \frac{V_l(s)}{s} = \frac{Q(s)}{As} = \frac{K_v}{As(\tau_v s + 1)} I(s). \tag{3.65}$$

I assume that the first-order dynamics accurately describes behaviors of the system in the frequency range of interest as in [96]. Also, no flow and pressure limits are assumed. I analyze the pneumatic system in terms of bandwidth and output impedance. However, as investigated in the previous section, the compressibility of the air entrapped in the fluidic circuit leads to elasticity. I simply convert the system controlled by the servo valve to an SEA system that includes elasticity (Fig. 3.5(b)). It is reasonable to virtually map the position controlled by fluid flow to position x_m and the position controlled by elasticity to position x_l in the SEA system. Position x_m can be regarded as position x_l in Eq. (3.65) With the elasticity lumped as a constant k_s, the output force F_l can be expressed as

$$F_l(s) = k_s(X_m(s) - X_l(s)) = k_s(\frac{K_v}{As(\tau_v s + 1)} I(s) - X_l(s)). \tag{3.66}$$

Force control I

For control of the output force F_l, I design the control signal i, introducing a controller $C_f(s)$, as follows (Fig. 3.30):

$$I(s) = C_f(s)(F_d(s) - F_l(s)), \tag{3.67}$$

where F_d is a desired force.

Substituting Eq. (3.67) into Eq. (3.66) yields the closed-loop output force:

$$F_l(s) = \frac{k_s K_v C_f(s) F_d(s) - k_s A s(\tau_v s + 1) X_l(s)}{A s(\tau_v s + 1) + k_s K_v C_f(s)}. \tag{3.68}$$

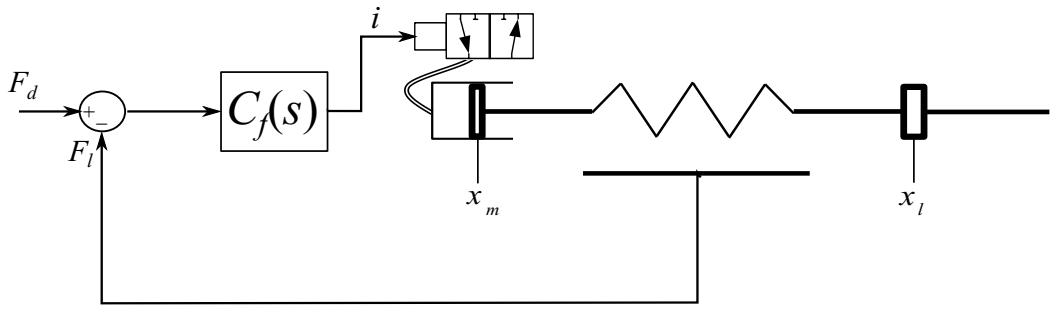

Figure 3.30: Force control I of a fluidic system

According to Eq. (3.68), the closed-loop output force F_l involves two inputs F_d and x_l. The characteristics of interest are the closed-loop bandwidth and output impedance. By eliminating the dynamics due to desired force, setting F_d to 0, I take a look at the two characteristics. The closed-loop output impedance Z_{clI} is expressed as

$$Z_{clI} = -\frac{F_l(s)}{X_l(s)} = \frac{k_s A s(\tau_v s + 1)}{A s(\tau_v s + 1) + k_s K_v C_f(s)}. \tag{3.69}$$

At low frequencies, it is possible that the impedance depends on controller C_f. As the Lapalce variable s approaches 0, Z_{clI} converges to $\frac{As}{K_v C_f}$. If gains of controller C_f are tuned high, the impedance at low frequencies decreases accordingly. At high frequencies (complex variable s goes to infinity), the impedance saturates to the value of k_s, the stiffness of fluid compressibility.

Force control II

In Force control I (Eq.(3.67)), though it can decrease the impedance to almost zero at low frequencies, controller C_f cannot manipulate the impedance at frequencies beyond the closed-loop bandwidth. An increase in the gains of the controller lead to broadening the bandwidth, but it raises up the impendence at low frequencies. Force control II would be a solution to this issue. I add an inner loop to Force control I so that position x_m is forced to track to a desired position x_{md} that leads to a

desired output force F_d through the relative distance with position x_l. The outer loop calculates x_{md} through a comparison between the desired output force F_d and actual output force F_l. This strategy, depicted in Fig. 3.31, gives the following control law:

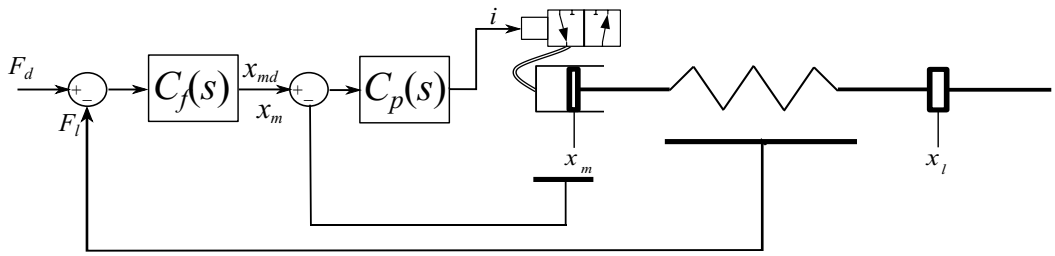

Figure 3.31: Force control II of a fluidic system

$$\begin{aligned} I(s) &= C_p(s)(X_{md}(s) - X_m(s)) = C_p(s)(C_f(s)(F_d(s) - F_l(s)) - X_m(s)) \\ &= C_p(s)(C_f(s)(F_d(s) - F_l(s)) - \frac{F_l}{k_s} - X_l(s)), \end{aligned} \tag{3.70}$$

where C_p is a controller of the inner loop.

I derive the closed-loop output force from the control input (3.70) as

$$F_l(s) = \frac{k_s K_v C_f(s) C_p(s) F_d(s) - (k_s K_v C_p(s) + k_s A s(\tau_v s + 1)) X_l(s)}{A s(\tau_v s + 1) + k_s K_v C_f(s) C_p(s) + K_v C_p(s)}, \tag{3.71}$$

and the output impendence as

$$Z_{clII} = -\frac{F_l(s)}{X_l(s)} = \frac{k_s K_v C_p(s) + k_s A s(\tau_v s + 1)}{A s(\tau_v s + 1) + k_s K_v C_f(s) C_p(s) + K_v C_p(s)}. \tag{3.72}$$

Assume that controllers C_p and C_f are constructed as, respectively,

$$C_p = k_{dp} s + k_{pp}, C_f = k_{df} s + k_{pf}, \tag{3.73}$$

where k_{dp}, k_{pp}, k_{df}, and k_{pf} are gains of controllers C_p and C_f.

At low frequencies ($s \to 0$), the impedance reduces to

$$Z_{clII} \approx \frac{k_s K_v k_{pp}}{k_s K_v k_{pf} k_{pp} + K_v k_{pp}} = \frac{k_s}{k_s k_{pf} + 1}. \tag{3.74}$$

I see that the impedance is near 0 if gain k_{pf} is set high. Meanwhile, at high frequencies ($s \to \infty$), the impedance approaches to

$$Z_{clII} \approx \frac{k_s A \tau_v s^2}{A\tau_v s^2 + k_s K_v k_{df} k_{dp} s^2} = \frac{k_s A \tau_v}{A\tau_v + k_s K_v k_{df} k_{dp}}. \tag{3.75}$$

A low impedance can be achieved over all frequencies by Force control II within flow and pressure limits by setting appropriate gains.

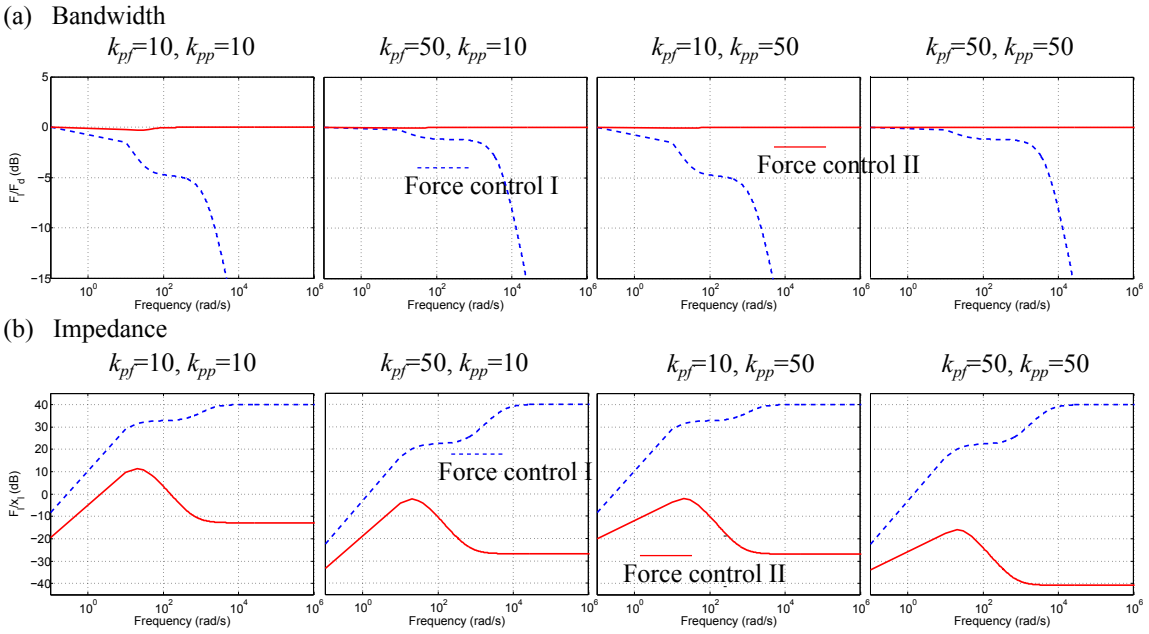

Figure 3.32: Closed-loop bandwidth (a) and impedance (b) of Force control I and Force control II with gains varying.

Fig. 3.32 shows a comparative study of Force control I and Force control II in terms of the closed-loop bandwidth and impedance with control gains varying. For this numerical investigation, I set the piston area A to 0.03 m^2 and the valve gain K_v to 2.38×10^{-5} [38]. The stiffness k_s is selected as 100. I adopt a value of τ_v in [96] as 0.0015. To primarily examine the effects of proportional gains k_{pf}, k_{pp} on bandwidth and impedance, I fix the ratio of the derivative gain versus the proportional gain of controllers C_f, C_p as 0.05, respectively. As for Force control I, a higher control gain produces a broader operational bandwidth and lower impedance within the bandwidth. As for Force control II, the operational bandwidth can be infinite as long as derivative gains of controllers C_p and C_f are nonzero. Also, as predicted in Eqs.(3.74) and (3.75), gains k_{df} and k_{dp} determine impedances at low and high frequencies. Overall, Force control II shows broader bandwidths and lower impedances in comparison with Force control I.

3.3.2 Position vs. Impedance control for backdriveable systems

In this section, I show how advantageous impedance control is for backdriveable systems in comparison with position control in terms of compliance and the closed-loop bandwidth. In addition, I also analyze impedance control of a system without series elasticity to reveal the role of the elastic element in lowering the driving-point impedance.

Firstly, let us consider the following simplified system with no distinction between joint-space and task-space, which is depicted in Fig. 3.33(a) and Fig. 3.33(b). The lumped masses M and B indicate the distal device including the exoskeleton and proximal device, respectively. A force F_e is applied to the lumped end-effector mass M from the user, while the motor applies a force F_m directly to the mass B to control the position of M. The compressibility of the air is lumped as stiffness k. Damping effects on the device are not considered here. The transmission dynamics is neglected. With x_l and x_m denoting the end-effector and proximal device positions, respectively, the equation of motion for the system can be expressed as

$$\begin{aligned} M\ddot{x}_l &= k(x_m - x_l) + F_e, \\ B\ddot{x}_m + k(x_m - x_l) &= F_m. \end{aligned} \tag{3.76}$$

Here, position and impedance control of the system is acheived through the back-stepping control technique. The technique breaks the whole system into a sequence of lower-order systems and starts constructing virtual inputs from the first lower-order system toward the control input in the last lower-order system. This technique therefore enables us to design straightforward position and impedance control laws for the end-effector. Using the backstepping approach, I design position and impedance controllers for the target system (3.76) that drives the end-effector position x_l to track a desired trajectory x_d.

Defining the state variables as $x_1 = x_l, x_2 = \dot{x}_l, x_3 = x_m$, and $x_4 = \dot{x}_m$, the system dynamics (3.76) can be rewritten in state-space form as

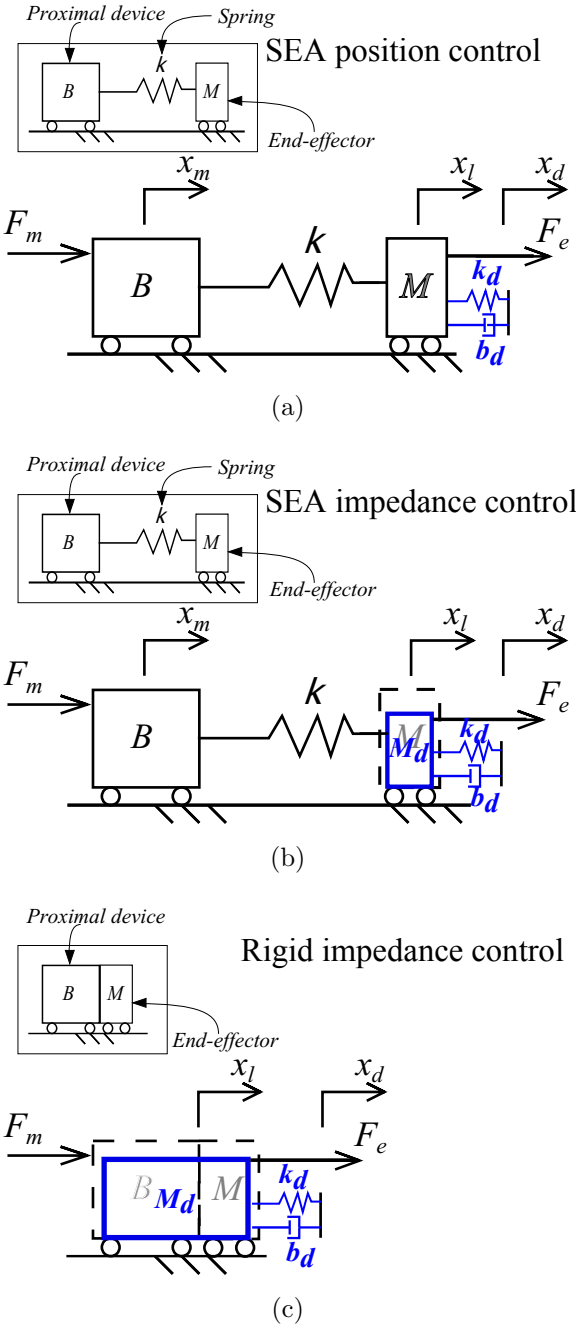

Figure 3.33: Schematic of (a) position control and (b) impedance control for SEA system, and (c) impedance control for a system without series elasticity.

$$\begin{aligned}
\dot{x}_1 &= x_2, \\
\dot{x}_2 &= (k(x_3 - x_1) + F_e)/M, \\
\dot{x}_3 &= x_4, \\
\dot{x}_4 &= (k(x_1 - x_3) + F_m)/B.
\end{aligned} \tag{3.77}$$

With an error and a Lyapunov function candidate V_1 defined as $e_1 \triangleq x_{1,d} - x_1$, $V_1 \triangleq \frac{1}{2}e_1^2$, respectively, the derivative of V_1 is obtained as

$$\dot{V}_1 = e_1\dot{e}_1 = e_1(\dot{x}_{1,d} - \dot{x}_1) = e_1(\dot{x}_{1,d} - x_2). \tag{3.78}$$

To cause the error e_1 to converge to zero using the Lyapunov theory, state x_2 in the first line of the system (3.76), called a virtual input, needs to be equal to value $\dot{x}_{1,d} + C_1e_1(\triangleq x_{2,d})$. C_1 is a control gain that should be positive so that the derivative of V_1 becomes negative as $-C_1e_1^2$. With $e_2 \triangleq x_{2,d} - x_2$, I construct another Lyapunov function candidate $V_2 \triangleq \frac{1}{2}e_2^2$. The negative definite derivative of V_2 gives a virtual input x_3 for the error e_2 to go to zero as follows:

$$\begin{aligned}\dot{V}_2 &= e_2\dot{e}_2 = e_2(\dot{x}_{2,d} - \dot{x}_2) \\ &= e_2(\ddot{x}_{1,d} + C_1\dot{e}_1 - (k(x_3 - x_1)/M) = -e_2C_2e_2, \qquad (3.79)\\ x_3 &= x_1 + M/k(\ddot{x}_{1,d} + C_1\dot{e}_1 + C_2e_2), \qquad (3.80)\end{aligned}$$

where C_2 denotes a positive control gain. The external force F_e is not taken into account in control design.

Using the relationship $e_2 = \dot{e}_1 + C_1e_1$, Eq. (3.80) can be rewritten as

$$x_3 = x_1 + M/k(\ddot{x}_{1,d} + (C_1 + C_2)\dot{e}_1 + C_1C_2e_1). \tag{3.81}$$

Note that Eq. (3.81) is a (virtual) control input for position control. Here, I attempt to construct an impedance control law that ejects the real impedance (e.g., link mass) and injects a desired impedance. The virtual impedance control law for the link is (it also guarantees boundedness of states with the Lyapunov function)

$$x_{3(IMP)} = x_1 + M/k(\ddot{x}_{1,d} - \ddot{e}_1 + m_d\ddot{e}_1 + (C_1 + C_2)\dot{e}_1 + C_1C_2e_1), \tag{3.82}$$

where m_d denotes the desired end-effector inertia to the user.

By looking at the link error dynamics, I gain the insight into the link impedance against the external force if it is applied:

$$m_d\ddot{e}_1 + (C_1 + C_2)\dot{e}_1 + C_1C_2e_1 + F_e = 0. \tag{3.83}$$

Combinations of C_1 and C_2 can set the desired damping $b_d(\triangleq C_1 + C_2)$ and desired

stiffness $k_d(\triangleq C_1C_2)$.

From here, I construct a virtual input (x_4) in the third line of the system (3.77) for x_3 and the actual control input F_m so that the link is under the position control or impedance control I designed above.

As for the virtual input x_4, I follow the procedure again:

$$e_3 \triangleq x_{3,d} - x_3, \tag{3.84}$$

$$\dot{V}_3 = e_3\dot{e}_3 = e_3(\dot{x}_{3,d} - \dot{x}_3) = e_3(\dot{x}_{3,d} - x_4) = -e_3C_3e_3, \tag{3.85}$$

$$x_4 = \dot{x}_{3,d} + C_3e_3 \tag{3.86}$$

where C_3 denotes a positive control gain and $\dot{x}_{3,d}$ is the derivative of x_3 in (3.81) or the derivative of $x_{3(IMP)}$ in (3.82).

The actual control input can be obtained through one more repetition; the objective is to force state x_4 to track the virtual control input obtained in (3.86). Letting x_4 in (3.86) be $x_{4,d}$, I define an error e_4 and a Lyapunov function candidate V_4 as follows:

$$e_4 \triangleq x_{4,d} - x_4, \tag{3.87}$$

$$\dot{V}_4 = e_4\dot{e}_4 = e_4(\dot{x}_{4,d} - \dot{x}_4) = -e_4C_4e_4, \tag{3.88}$$

and the actual control inputs I have are

$$F_m = -k(x_1 - x_3) + B\ddot{x}_{3,d} + BC_3\dot{e}_3 + BC_4\dot{e}_4, \tag{3.89}$$

where C_4 denotes a positive control gain.

The final control laws are arranged as, with the relationship $e_4 = \dot{e}_3 + C_3e_3$:

- SEA Position control

$$\begin{aligned} F_m = &- k(x_1 - x_3) + B(\ddot{x}_1 + M/k({x^{(4)}}_{1,d} + (C_1 + C_2)\dddot{e}_1 + C_1C_2\ddot{e}_1) + B(C_3 + C_4)\dot{e}_3 + \\ &BC_3C_4e_3, \end{aligned} \tag{3.90}$$

- SEA Impedance control

$$\begin{aligned} F_m = &- k(x_1 - x_3) + B(\ddot{x}_1 + M/k(x^{(4)}_{1,d} - e_1^{(4)} + m_de_1^{(4)} + (C_1 + C_2)\dddot{e}_1 + C_1C_2\ddot{e}_1) \\ &+ B(C_3 + C_4)\dot{e}_3 + BC_3C_4e_3. \end{aligned} \tag{3.91}$$

Note that only the two terms $-e_1^{(4)} + m_d e_1^{(4)}$ are added to the impedance control law from the position control law. These two terms are needed to replace the desire inertia with the end-effector inertia (see Eq. 3.83).

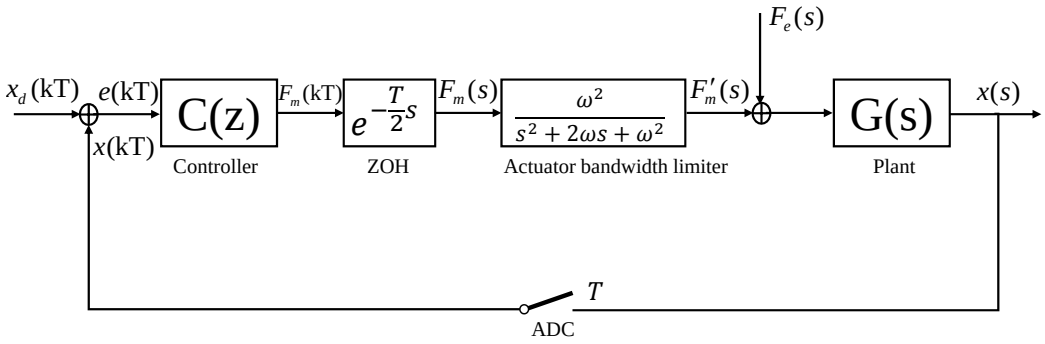

Figure 3.34: Digital control implementation.

Impedances

To emulate the digital control environment, two limitations are taken into account: the limited bandwidth of the actuator and a time delay from zero-order hold (ZOH), as depicted in Fig. 3.34. The delay of half the sample time T results from the digital computer using A/D and D/A converters [18]. I equate these two factors as

$$D(s) \triangleq \frac{\omega^2}{s^2 + 2\omega s + \omega^2} e^{(-\frac{T}{2}s)}, \tag{3.92}$$

where ω denotes the actuator bandwidth.

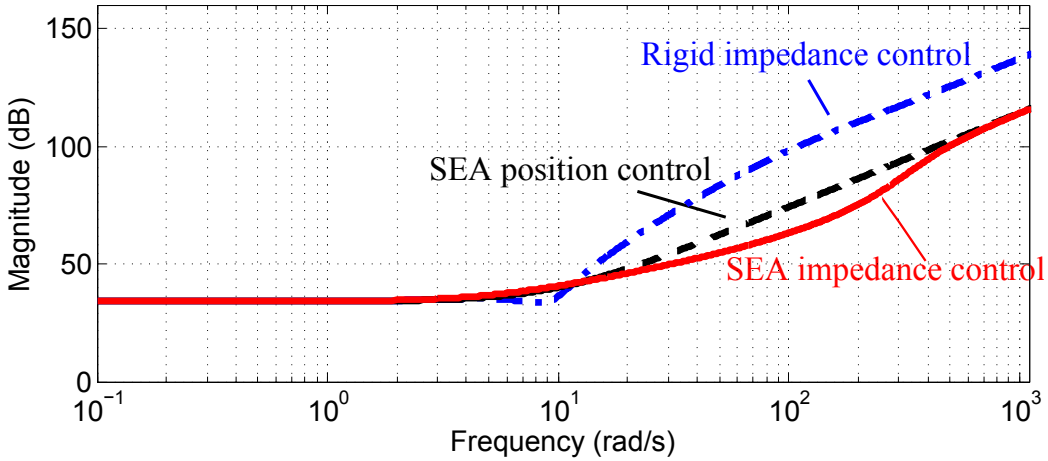

Figure 3.35: Driving-point impedance.

By applying the position (3.90) and impedance (3.91) control inputs to the system (3.76), the closed-loop driving-point impedances defined as the interaction force F_e

over the end-effector position q_l are obtained as follows:

$$Z(s) \triangleq \frac{F_e}{q_l} = Ms^2 + k - k\frac{k + D(s)(k + QB(s^2 + (c_3 + c_4)s + c_3c_4 - k))}{Bs23 + k + D(s)(B(c_3 + c_4)s + Bc_3c_4 - k)}, \quad (3.93)$$

where $Q = (k - M((c_1 + c_2)s + c_1c_2))/k$ for SEA position control and $Q = (k - M(m_d/M - 1)s^2 + (c_1 + c_2)s + c_1c_2)/k$ for SEA impedance control.

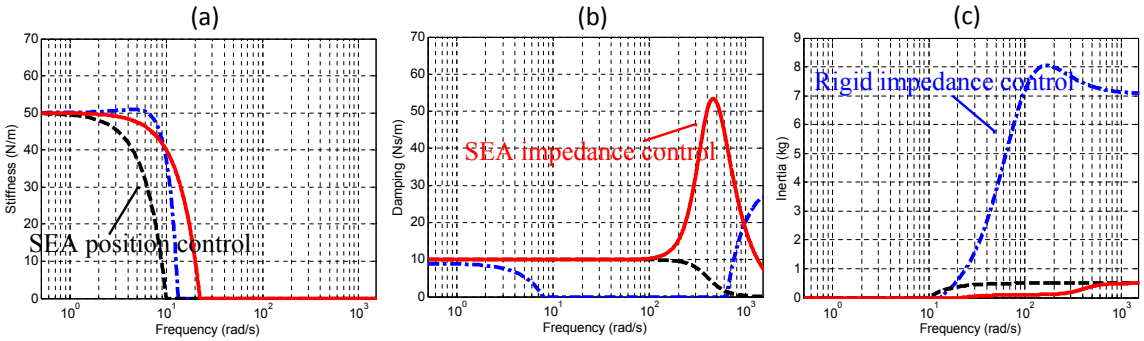

Figure 3.36: Effective impedance components: (a) stiffness, (b) damping, and (c) inertia.

For impedance control of the plant that does not include the elastic element (Fig. 3.33(c)), the impedance is given as

$$Z(s) = (M + B)s^2 + D(s)\big((-M - B + m_d)s^2 + (c_1 + c_2)s + c_1c_2\big). \quad (3.94)$$

Based on the driving part developed in Section 3.1, the value of parameter B is selected as 6.56 kg. The mass M is estimated as 0.5 kg. The stiffness k is 120 approximately. The desired damping b_d $(=c_1 + c_2)$ and stiffness k_d $(=c_1c_2)$ for the end-effector are set to 20 N/m and 100 N/m, respectively. And the desired mass m_d is 0.1 kg for the impedance control case. The desired impedance parameters m_d, b_d, and k_d are set to the same values for the three strategies so that the same impedance appears at low frequencies. Gains c_3, c_4 are both set as 500. The actuator bandwidth is set as 150 rad/s and the sampling time is chosen as $T = 0.001s$, which is achievable in a typical digital implementation.

Fig. 3.35 shows the closed-loop impedance of each control strategy. Fig. 3.36 analyzes the effective impedances component by component as the so-called effective impedances, presented in [78]. At low frequencies up to the bandwidth $\sqrt{\frac{k_e}{m_e}}$, where k_e, m_e denote the effective programmed stiffness and effective end-effector mass, respectively, the virtual desired stiffness is predominant in all strategies. After its system bandwidth, the impedance control strategy begins showing the system mass but the desired mass that is replaced with the system mass seems to be in effect under

the actuator bandwidth limit. In the position control case, the real end-effector mass appears after its closed-loop bandwidth. The impedance plot demonstrates that SEA systems benefit from decoupling of the load from the proximal device in aspect of impedance. As shown in Fig. 3.36(c), in the impedance control of the system without series elasticity, the summed mass of the load and proximal device becomes apparent at high frequencies. In contrast to this case, the SEA system has the lower upper limit of impedance in mass. That is, SEA systems are advantageous in that only the load mass is apparent in the frequency range beyond control. As predicted, the combination of an SEA with impedance control further lowers the driving-point impedance. This results in the fact that the desired mass is substituted for the real load mass in impedance control as long as the actuator allows it. Accordingly, SEA impedance control gives higher closed-loop bandwidth than SEA position control.

3.3.3 Robust impedance controller development

It is generally difficult to precisely identify a system model. Uncertainties including the system inertia, unknown nonlinearities, and unforeseen disturbances invariably degrade control performance. In particular, control of pneumatic systems suffers from a substantial difficulty due to the nonlinearity resulting from fluid compressibility. The technique of time delay estimation (TDE) provides a simple tool that makes it possible to estimate the actual system dynamics being controlled [12, 14, 46, 52, 55, 56, 62, 72]. The control input naturally gives rise to a certain system output, going through the system dynamics and uncertainties including disturbances. Using this fact, the TDE technique estimates the current system dynamics and uncertainties with the latest past system dynamics and uncertainties, which are estimated from the previous control input and its accompanying consequence. In this section, a robust and model-free impedance controller incorporated with the TDE technique for fluidic systems is presented. The target system to be controlled is an exoskeleton with pneumatic circuits, as depicted in Fig. 3.37. Assume that the master cylinder is powered by a motor, as in Fig. 3.6, and the end-effector is actuated through the rotary transmission designed in Section 3.2.1. The driving part is translational, while the driven part is rotational.

With the translational and rotational stiffnesses resulting from fluidic compressibility lumped as k_x, k_θ, the system model can be developed as

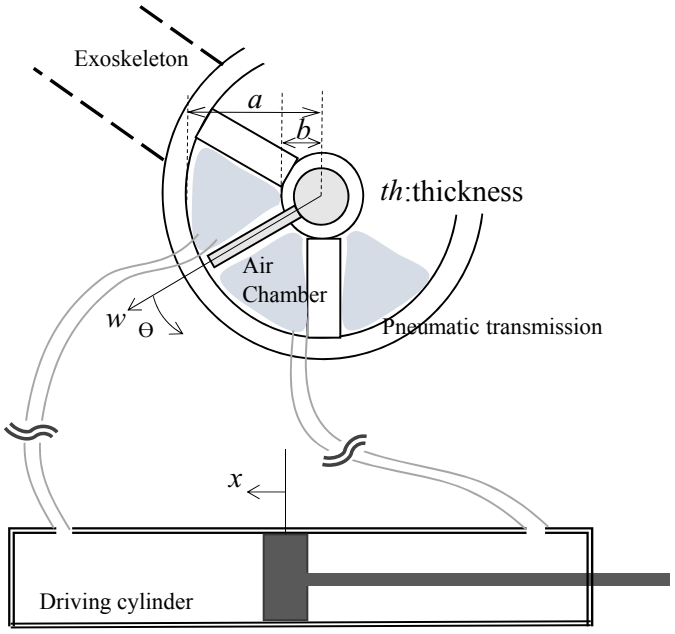

Figure 3.37: Schematic of a pneumatic exoskeleton system.

$$
\begin{aligned}
I\ddot{\theta} &= k_\theta(x/r - \theta) - mgl\sin\theta + f_1 + d_1 + F_e, \\
B\ddot{x} + k_x(x - r\theta) &= f_2 + d_2 + F_m,
\end{aligned} \tag{3.95}
$$

where I, m denote the inertias of the driven part including the exoskeleton; g the gravitational constant; l the distance between the joint and the center of mass of the driven part; B the inertia of the driving part; f_1, f_2 friction forces; d_1, d_2 bounded disturbances; r the ratio between translational motion and rotational motion.

The stiffnesses k_x, k_θ can be obtained using the ideal gas law $PV = mRT$. To express stiffness k_x, I first denote F_p as the resultant force exerted on the driving piston. The pneumatic system consists of two separate fluidic circuits: one entraps air in front of the driving piston, the other one in back of the driving piston. I express the first circuit with subscript 1 and the second circuit with subscript 2. It is assumed that the air chambers are made of an inelastic material.

$$
F_p = -P_1A_1 + P_2A_2 = -\frac{m_1RT}{V_1}A_1 + \frac{m_2RT}{V_2}A_2, \tag{3.96}
$$

where P, V, m with subscript 1 and 2 denote the pressure, volume and mass of the air

entrapped in each circuit, A_1 is the front side area of the piston and A_2 is the back side area of the piston considering the area of the rod.

The volumes of the air entrapped in each circuit V_1, V_2 are obtained as

$$V_1 = V_{10} - A_1 x + \frac{3th(a^2 - b^2)\theta}{2}, \tag{3.97}$$

$$V_2 = V_{20} + A_2 x - \frac{3th(a^2 - b^2)\theta}{2}, \tag{3.98}$$

where V with subscript 0 indicates the initial volume, and th, a, b denote the dimensions of the air chambers in the rotary pneumatic transmission, weight 3 is multiplied because three air chambers form one fluidic circuit.

Then stiffness k_x is given as

$$\begin{aligned} k_x \triangleq & -\frac{\partial F_p}{\partial x} = -\frac{m_1 RT}{V_1^2} V_1' A_1 + \frac{m_2 RT}{V_2^2} V_2' A_2 = \frac{m_1 RT}{V_1^2} A_1^2 + \frac{m_2 RT}{V_2^2} A_2^2 \\ = & \frac{m_1 RT}{\left(V_{10} - A_1 x + \frac{3th(a^2-b^2)\theta}{2}\right)^2} A_1^2 + \frac{m_2 RT}{\left(V_{20} + A_2 x - \frac{3th(a^2-b^2)\theta}{2}\right)^2} A_2^2. \end{aligned} \tag{3.99}$$

Next, the stiffness k_θ can be obtained in a similar way.

The torque τ_t that is transferred to the exoskeleton in the transmission by fluid can be expressed as the product of the force by the air pressure and the distance of it from the the origin along the w axis:

$$\tau_t = 3P_1 th \int_b^a w dw + 3P_2 th \int_b^a w dw. \tag{3.100}$$

Then stiffness k_θ is written as

$$k_\theta = \frac{\partial \tau_t}{\partial \theta} = \frac{3th(a^2 - b^2)}{2} \left(\frac{\partial P_1}{\partial \theta} - \frac{\partial P_2}{\partial \theta}\right) = \left(\frac{3th(a^2 - b^2)}{2}\right)^2 \left(\frac{m_1 RT}{V_1^2} + \frac{m_2 RT}{V_2^2}\right). \tag{3.101}$$

With Eqs. (3.97) and (3.98), Eq. (3.101) can be rewritten as

$$k_\theta = \left(\frac{3th(a^2 - b^2)}{2}\right)^2 \left(\frac{m_1 RT}{\left(V_{10} - A_1 x + \frac{3th(a^2-b^2)\theta}{2}\right)^2} + \frac{m_2 RT}{\left(V_{20} + A_2 x - \frac{3th(a^2-b^2)\theta}{2}\right)^2}\right). \tag{3.102}$$

The ratio r can be derived from the following relationship:

$$\frac{3th(a^2-b^2)}{2}d\theta = A_1 dx. \tag{3.103}$$

From this relationship, ratio r is defined as

$$r \triangleq \frac{dx}{d\theta} = \frac{3th(a^2-b^2)}{2A_1}. \tag{3.104}$$

Note that SEA systems, which are equivalent to flexible-joint systems, are feedback linearizable [108]. With the state variables denoted as $x_1 = \theta, x_2 = \dot{\theta}, x_3 = x$, and $x_4 = \dot{x}$, the equations of motion (3.95) are expressed in state-space form:

$$\begin{aligned}
\dot{x}_1 &= x_2, \\
\dot{x}_2 &= (k_\theta(x_3/r - x_1) + G + f_1 + d_1 + F_e)/I, \\
\dot{x}_3 &= x_4, \\
\dot{x}_4 &= (-k_x(x_3 - rx_1) + f_2 + d_2 + F_m)/B,
\end{aligned} \tag{3.105}$$

where $G \triangleq -mgl\sin x_1$.

Under the following nonlinear state coordinate transformation

$$\begin{aligned}
z_1 &= x_1, \\
z_2 &= x_2, \\
z_3 &= (k_\theta(x_3/r - x_1) + G + f_1 + d_1 + F_e)/I, \\
z_4 &= (k_\theta(x_4/r - x_2) + \dot{G} + \dot{f}_1 + \dot{d}_1 + \dot{F}_e)/I,
\end{aligned} \tag{3.106}$$

the model (3.105) can be written in terms of the new coordinates as

$$\begin{aligned}
\dot{z}_1 &= z_2, \\
\dot{z}_2 &= z_3, \\
\dot{z}_3 &= z_4, \\
\dot{z}_4 &= \alpha(z) + \beta F_m,
\end{aligned} \tag{3.107}$$

where

$$\alpha(z) = -\frac{k_\theta}{I}z_3 - \frac{k_x}{B}z_3 + \frac{1}{I}(\ddot{G} + \ddot{f}_1 + \ddot{d}_1 + \ddot{F}_e) + \frac{k_x}{IB}(G + f_1 + d_1 + F_e) + \frac{k_\theta}{rIB}(f_2 + d_2), \tag{3.108}$$

$$\beta = \frac{k_\theta}{rIB}. \tag{3.109}$$

The feedback linearizing control (FLC) $F_m = (-\alpha(z) + \nu)/\beta$ is one of the candidates for stabilizing and tracking. This control law contains two main functions: cancelling out the system dynamics ($\alpha(z)$) and injecting the desired dynamics through the new input ν. But this control is in need of a precise system model. Also, it cannot deal with uncertainties including disturbances and friction. But, a robust controller can be created with the TDE technique.

Before elaborating the design of the robust controller, it is noted that a continuous-time plant is generally controlled in digital implementation. A controller is discretized and implemented with sample and hold devices. Hence, I develop the controller in a sample-data environment.

Assuming that the state variables of the system are measured at sampling instants $\cdots, t_{k-1}, t_k, t_{k+1}, \cdots$, a discrete-time controller is designed as

$$F_m(t) = F_m(t_k), t \in [t_k, t_{k+1}). \tag{3.110}$$

With an input delay approach [36], we re-express

$$F_m(t_k) = F_m(t - d(t)), t \in [t_k, t_{k+1}), \tag{3.111}$$

where t_k denotes the sampling instant and $d(t)(= t - t_k \leq d_{max} = L(\text{sampling interval}))$ denotes a time-varying delay that is continuous with $\dot{d}(t) \leq l < 1$.

Let us consider and reexpress the last line of Eq. (3.107) as follows:

$$\dot{z}_4 = z_1^{(4)} = \alpha(z) + \beta F_m - \overline{\beta}F_m(t-d) + \overline{\beta}F_m(t-d) = h + \overline{\beta}F_m(t-d), \tag{3.112}$$

where $\overline{\beta}$ is a constant and h contains the system dynamics and all uncertainties.

The term h can be estimated with the previous-step control input and its corre-

sponding measured output as aforementioned.

$$\begin{aligned} &h(t) \approx h(t-d), \\ &\widehat{h}(t) \triangleq h(t-d) = -z_1^{(4)}(t-d) + \overline{\beta} F_m(t-d-L). \end{aligned} \tag{3.113}$$

Utilizing this approach, the control law is constructed as

$$F_m(t-d) = \frac{1}{\overline{\beta}}(-h(t-L)+\nu) = F_m(t-d-L) + \frac{1}{\overline{\beta}}(-z_1^{(4)}(t-d)+\nu). \tag{3.114}$$

The new control input, denoted as ν, determines the error dynamics of the system. We can design ν for position control as

$$\nu = z_d^{(4)}(t-d) + c_1 \dddot{e}(t-d) + c_2 \ddot{e}(t-d) + c_3 \dot{e}(t-d) + c_4 e(t-d), \tag{3.115}$$

where $e(t) \triangleq z_d(t) - z(t)_1$ and $c_1, \cdots, c_4$ are design parameters.

For impedance control, the error dynamics needs to be related with the external force through the new control input ν. The error dynamics interacting with the external force F_e for the driving part is defined as Ω:

$$\Omega \triangleq I_d \ddot{e} + b_d \dot{e} + k_d e + F_e. \tag{3.116}$$

Adjusting Eq. (3.116) to error dynamics of a 4^{th} order system leads to

$$\ddot{\Omega} + p\dot{\Omega} + q\Omega = 0, \tag{3.117}$$

where p, q are constants that shape the convergence of Ω.

With states measured at time $t-d$, the control input ν for achieving the desired error dynamics (3.117) can be designed as

$$\begin{aligned} \nu = {} & z_d^{(4)}(t-d) + (b_d + pI_d)/I_d \dddot{e}(t-d) + (k_d + pb_d + qI_d)/I_d \ddot{e}(t-d) \\ & + (pk_d + qb_d)/I_d \dot{e}(t-d) + qk_d/I_d e(t-d) + \big(\ddot{F}_e(t-d) + p\dot{F}_e(t-d) + qF_e(t-d)\big)/I_d. \end{aligned} \tag{3.118}$$

However, TDE error, an estimation error, arises from estimating the current value by the value obtained from the sampling. The TDE error is involved in the convergence of the error dynamics. With TDE error defined as

$$\varepsilon(t) \triangleq \widehat{h}(t-d) - h(t) = \nu - z_1^{(4)}(t), \tag{3.119}$$

I have the error dynamics of the proposed controller including TDE error by substituting Eq. (3.115) into Eq. (3.119) as follows (position control):

$$\varepsilon(t) = z_d^{(4)}(t-d) - z_1^{(4)}(t) + c_1 \dddot{e}(t-d) + c_2 \ddot{e}(t-d) + c_3 \dot{e}(t-d) + c_4 e(t-d). \tag{3.120}$$

Note that $\varepsilon(t)$ causes the system output to deviate from the desired trajectory. As mentioned in the Introduction, the existence of TDE error influences the stability and performance of the closed-loop system. In an effort to reduce the effect of $\varepsilon(t)$ on the error dynamics and guarantee system stability, I employ a learning algorithm, which has been employed in various adaptive controllers [2, 57]. The learning law to counteract the combined TDE error $\varepsilon(t)$ is

$$\widehat{\varepsilon}(t-d) = \widehat{\varepsilon}(t-d-L) - a\xi(t-d), \tag{3.121}$$

where a is a learning factor.

The tracking error is defined as

$$\xi(t-d) \triangleq k_1 e^{(4)}(t-d) + k_2 \dddot{e}(t-d) + k_3 \ddot{e}(t-d) + k_4 \dot{e}(t-d) + k_5 e(t-d), \tag{3.122}$$

where k_i $(i = 1, \cdots, 5)$ are parameters.

Applying the counteracting term $\widehat{\varepsilon}(t-d)$ to the actual control input (3.114), I have

$$F_m(t-d) = F_m(t-d-L) + \overline{\beta}^{-1}\big[z_1^{(4)}(t-d) + v + \widehat{\varepsilon}(t-d)\big]. \tag{3.123}$$

The proof of the stability of the overall closed-loop system is presented in the end of the chapter.

Gain selection

The gains I_d, b_d, and k_d determine the desired impedance of the end-effector. The constants p, q do not affect the desired impedance, rather determine how fast the desired impedance against the interaction force is achieved. As for $\overline{\beta}$, it can be determined by tuning without knowledge of the target system model. One recommendable way is to begin with a high positive value and then decrease the value until a better performance is achieved.

Derivatives of states

The proposed control requires derivatives of states. Simple numerical differentiation (backward differencing) or using an observer [61] would be a good candidate

to obtain these derivatives. However, these candidates are sensitive to measurement noise. Here, I present a recommendable method to calculate derivatives, which was proposed in [73]. The separation principle is fulfilled for the method, therefore, it could be used in almost any feedback control [73].

Assuming that $z^{(4)} \leq M$, the estimates of the derivatives of states required for control can be the following equations: This estimation can be applied to obtain the derivatives of external force F_e as well.

$$|\dot{\hat{z}}_1| = v_1, \quad v_1 = -5M^{1/4}|\hat{z}_1 - z_1|^{3/4}\text{sign}(\hat{z}_1 - z_1) + \hat{z}_1, \tag{3.124}$$

$$\ddot{\hat{z}}_1 = v_2, \quad v_2 = -3M^{1/3}|\dot{\hat{z}}_1 - v_1|^{2/3}\text{sign}(\dot{\hat{z}}_1 - v_1) + \dot{\hat{z}}_1, \tag{3.125}$$

$$\dddot{\hat{z}}_1 = v_3, \quad v_3 = -1.5M^{1/2}|\ddot{\hat{z}}_1 - v_2|^{1/2}\text{sign}(\ddot{\hat{z}}_1 - v_1) + \ddot{\hat{z}}_1, \tag{3.126}$$

$$\hat{z}_1^{(4)} = -1.1M\text{sign}(\dddot{\hat{z}}_1 - v_3). \tag{3.127}$$

The larger M, which can be tuned, leads to the faster the convergence but the higher sensitivity to measurement noise and the sampling step.

3.3.4 Numerical validation

I conduct a simulation study of the proposed control with the pneumatic system (Fig. 3.37). The system parameters are presented in Table 3.2. I first examine the robustness of the proposed control to unstructured uncertainties through a comparison with Spong's FLC ($F_m = (-\alpha(z) + \nu)/\beta$ with α and β in Eq. (3.109)). And the effect of TDE error compensation is examined with the learning factor a varying. This examination is performed in free space. Next, the proposed impedance control is investigated in interaction with an environment.

Parameter	Symbol	Value	Unit
Driven part inertia	I	0.04	kgm^2
Gravitational torque	mgl	2	Nm
Driving part inertia	B	1.5	kg
Driving cylinder bore	$A_1, A, 2$	0.0011, 0.0009	m^2
Universal gas constant	R	287	J/kgK
Temperature	T	293	K
Initial volume	V_{10}, V_{20}	0.0003	m^3
Air mass	m_1, m_2	3.6123×10^{-04}	kg
Air chamber thickness	th	0.03	m
Air chamber outer diameter	a	0.04	m
Air chamber inner diameter	b	0.02	m

Table 3.2: Parameters of the pneumatic system.

The mismatched disturbance d_1 and matched disturbance d_2 are imposed as $2\sin(2t)$ Nm and $10\cos(5t)$ N, respectively. Friction f_1 is given as $0.2\dot{q}_1$ Nm while f_2 as $2\dot{q}_2 + 2\text{sgn}(\dot{q}_2)$ N. The sampling time L is 0.001 s. And $d(t)$ is assumed to 0 in

this simulation. The 4^{th} order Runge-Kutta method is adopted to solve the system dynamics with step size 0.00001 s. The primary objective of this simulation study is to evaluate the performance of the proposed control. The derivatives of the states for control are obtained simply by numerical differentiation (backward differencing), assuming that no measurement noise is involved.

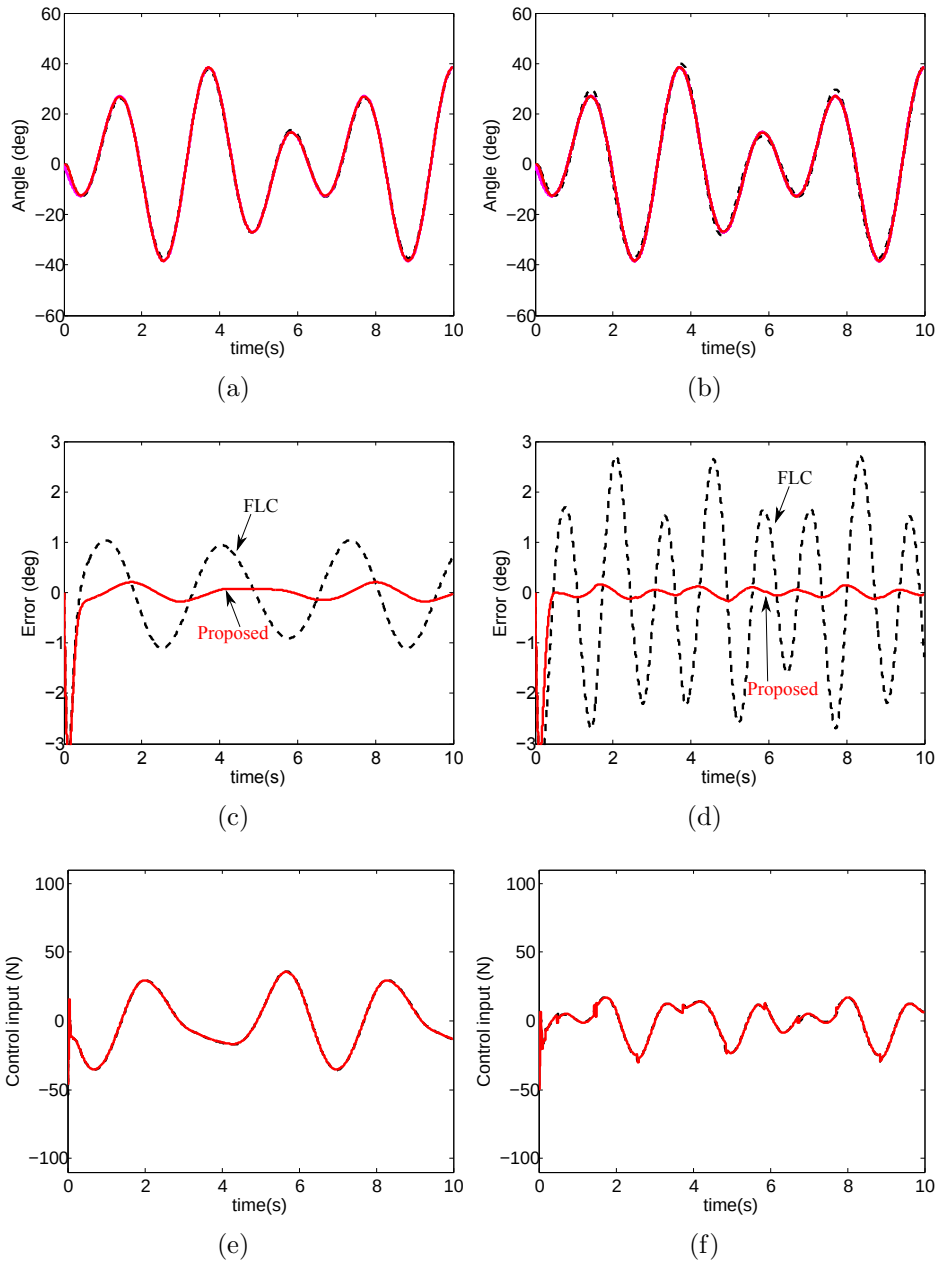

Figure 3.38: Comparisons of the proposed control with the feedback linearizing control (FLC) under mismatched and matched uncertainties: (a), (b) position (two curves overlap), (c), (d) position error, and (e), (f) control input (two curves overlap).

Robustness to uncertainties

To investigate the robustness of the proposed control to mismatched uncertainties as well as matched uncertainties, I select Spong's FLC as a comparison target. To focus on unstructured uncertainties, I provide his FLC with exact values of the system parameters in α and β (3.109) to eliminate structured uncertainties. The same new input ν (3.115) is injected into the proposed control and FLC with the control gains c_1, c_2, c_3, and c_4 in Eq. (3.123) set to 80, 2400, 32000, and 160000, respectively, to achieve critical damping. The gain $\overline{\beta}$ of the proposed control is tuned to 800. TDE counteraction is turned off through the proposed control and FLC.

Fig. 3.38 shows the results of the comparisons between the two controllers. The figures on the left column are under mismatched uncertainties (while $d_2 = 0$ and $f_2 = 0$), whereas the figures on the left column are under matched uncertainties (while $d_1 = 0$ and $f_1 = 0$). The proposed control exhibits notably reduced tracking error in the presence of matched and mismatched unstructured uncertainties, in comparison with FLC. This indicates that TDE efficiently deals with uncertainties. But note that no notable corresponding increase in control input is shown.

Effect of TDE error compensation

The effect of TDE error compensation using a learning algorithm is examined with 4 different values of learning factor a: 0, 0.01, 0.05, and 0.1. The gains k_1, k_2, k_3, k_4, and k_5 in Eq. (3.122) are selected as 1, 80, 2400, 32000, and 160000, respectively. All structured uncertainties are imposed.

Fig. 3.39 shows that a greater value of a provides more accuracy in tracking. This suggests that the term $\widehat{\varepsilon}$ in the control law that is introduced to counteract TDE error plays a role in cancelling out the TDE error that influences the convergence of the error dynamics. This accordingly leads to reduced position error. Counteracting the TDE error does not require a significant increase in control input.

Impedance control

Next, I validate the proposed control in constrained space. The simulation scenario is to rotate the exoskeleton 30 degrees. At the location of the angle θ_e of 20 degrees of the exoskeleton, a wall is installed, which is mathematically modeled as $F_e = 100(\theta_e - \theta)$. The control gains are set as: $I_d = 0.01, b_d = 2, k_d = 25, p = 10$, and $q = 25$. $\overline{\beta}$ is tuned to 8500. I use a 9^{th} order polynomial trajectory: $\theta_d = -0.0037t^9 + 0.057t^8 - 0.273t^7 + 0.7544t^6 - 1.0863t^5 + 0.6789t^4$. All structured uncertainties are imposed.

Fig. 3.40 shows the result of the proposed impedance control of the fluidic exoskeleton. With no interaction, the end-effector follows the desired trajectory satisfactorily.

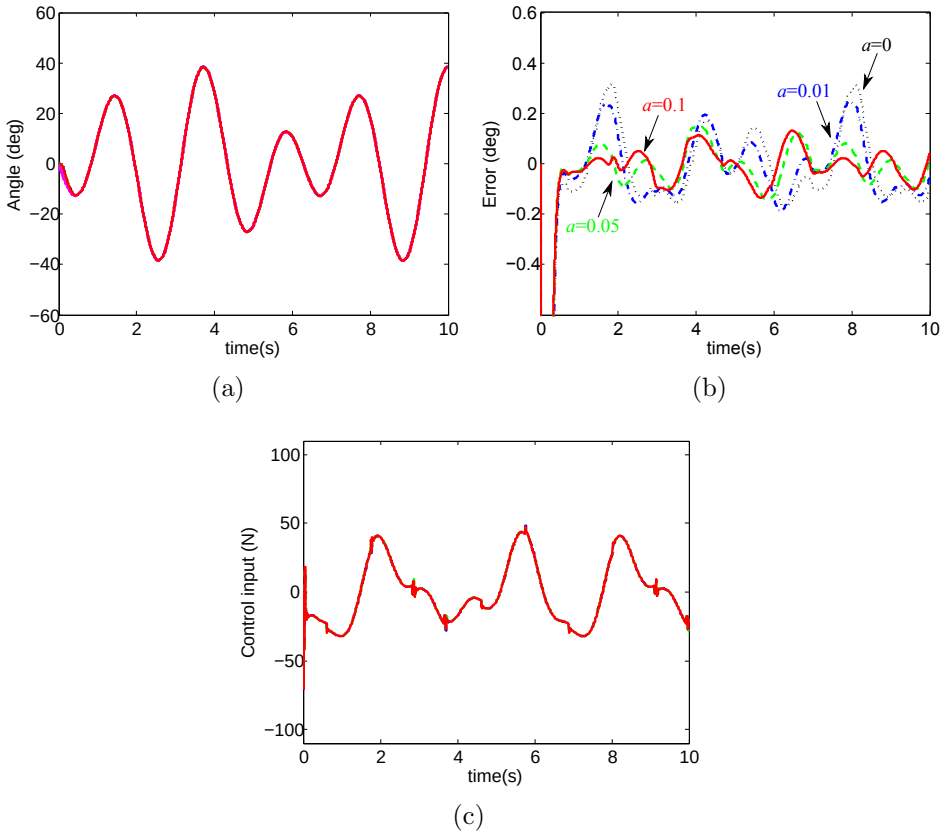

Figure 3.39: Performance of the proposed control with different values of learning factor a: (a) position (four curves overlap), (b) position error, and(c) control input (four curves overlap).

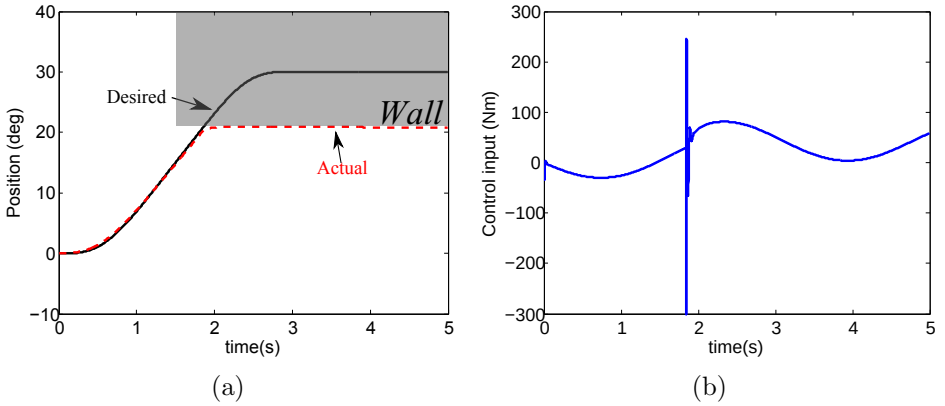

Figure 3.40: Simulation results of impedance control of the pneumatic exoskeleton system: (a) the end-effector position and (b) control input.

With interaction, the controller causes the end-effector to follow the desired trajectory with the desired impedance, not penetrating the wall thoroughly. At the moment of collision with the wall, a fluctuation is exhibited in control input. This phenomenon

results from sudden increases in the derivatives of the robot states and external force F_e at that moment.

3.3.5 Stability analysis

The proposed control law is designed for sampled-data systems in digital implementation. The system is modeled as a continuous-time system with the delayed control input. Moreover, our controller uses time delay estimation (TDE), which results in TDE error that could break the closed-loop stability. The learning counteraction to TDE error guarantees stability. In this section, I prove that the closed-loop system is globally asymptotically stable. The stability analysis of the time-delay system is conducted based on [36]. By applying the control input (3.123) to the target system (3.112), the closed-loop system including TDE error and its compensation can be expressed as follows. I assume that $z_d^{(4)}(t) \approx z_d^{(4)}(t-d)$. The external force F_e is not considered in the stability analysis (F_e is assumed to be bounded).

$$\begin{aligned} e^{(4)}(t) = &- c_1 \dddot{e}(t-d) - c_2 \ddot{e}(t-d) - c_3 \dot{e}(t-d) \\ &- c_4 e(t-d) + \varepsilon(t) - \widehat{\varepsilon}(t-d). \end{aligned} \tag{3.128}$$

The closed-loop dynamics can be expressed in a matrix form as

$$\dot{\mathbf{e}}(t) = A_0 \mathbf{e}(t) + A_1 \mathbf{e}(t-d) + \mathbf{E}(t), \tag{3.129}$$

where

$$A_0 = \begin{bmatrix} 0 & 1 & 0 & 0 \\ 0 & 0 & 1 & 0 \\ 0 & 0 & 0 & 1 \\ 0 & 0 & 0 & 0 \end{bmatrix}, \tag{3.130}$$

$$A_1 = \begin{bmatrix} 0 & 0 & 0 & 0 \\ 0 & 0 & 0 & 0 \\ 0 & 0 & 0 & 0 \\ -c_1 & -c_2 & -c_3 & -c_4 \end{bmatrix}, \tag{3.131}$$

$$\mathbf{e}(t) = [e(t) \quad \dot{e}(t) \quad \ddot{e}(t) \quad \dddot{e}(t)]^T, \tag{3.132}$$

$$\mathbf{E}(t) = [0 \quad 0 \quad 0 \quad \widetilde{\varepsilon}]^T, \tag{3.133}$$

$$\widetilde{\varepsilon}(t) \triangleq \varepsilon(t) - \widehat{\varepsilon}(t-d). \tag{3.134}$$

I express Eq. (3.129) in an equivalent descriptor form as follows:

$$\dot{\mathbf{e}}(t) = \mathbf{y}(t), \tag{3.135}$$

$$0 = -\mathbf{y}(t) + (A_0 + A_1)\mathbf{e}(t) - A_1 \int_{t-d}^{t} \mathbf{y}(s)ds + \mathbf{E}(t). \tag{3.136}$$

Again, Eq. (3.129) can be written in an extended form as

$$F\dot{\bar{\mathbf{e}}}(t) = \begin{bmatrix} \dot{\mathbf{e}}(t) \\ \mathbf{0} \end{bmatrix} \tag{3.137}$$

$$= \begin{bmatrix} \mathbf{0} & I \\ A_0 + A_1 & -I \end{bmatrix} \bar{\mathbf{e}}(t) - \begin{bmatrix} \mathbf{0} \\ A_1 \end{bmatrix} \int_{t-d}^{t} \mathbf{y}(s)ds + \begin{bmatrix} \mathbf{0} \\ \mathbf{E}(t) \end{bmatrix}, \tag{3.138}$$

where $\bar{\mathbf{e}}(t) = [\mathbf{e}(t), \mathbf{y}(t)]^T$ and $F = diag[I, 0]$.

Next, I consider the following Lyapunov-Krasovskii functional. From here, I assume that $n \times n$ matrices $P_1, P_2, P_3, S, U_1, U_2, Z_1, Z_2, Z_3, R$, and N are all positive.

$$W_1(t) \triangleq \bar{\mathbf{e}}^T(t)FP\bar{\mathbf{e}}(t) + \int_{t-d}^{t} \mathbf{e}^T(s)S\mathbf{e}(s)ds$$
$$+ \int_{-L}^{0}\int_{t+\sigma}^{t} \mathbf{y}^T(s)R\mathbf{y}(s)dsd\sigma + \frac{1}{a}\int_{-L}^{0}\int_{t+\sigma}^{t} |\dot{\varepsilon}(s)||\widetilde{\varepsilon}(t)|dsd\sigma$$
$$+ \frac{1}{a}\int_{-d}^{0}\int_{t+\sigma}^{t} |\dot{\xi}(s)||\widetilde{\varepsilon}(t)|dsd\sigma \tag{3.139}$$

where

$$P \triangleq \begin{bmatrix} P_1 & 0 \\ P_2 & P_3 \end{bmatrix}, \quad FP = P^T F \geq 0.$$

And another Lyapunov functional is taken into account:

$$W_2(t) \triangleq \int_{t-L}^{t} \frac{1}{2a}\widetilde{\varepsilon}^2(s)ds. \tag{3.140}$$

Differentiating W_1 along the trajectories of Eq. (3.129) leads to

$$\begin{aligned} \dot{W}_1(t) \leq & \bar{\mathbf{e}}^T(t)\bar{\Gamma}\bar{\mathbf{e}}(t) - (1-\dot{d})\mathbf{e}^T(t-d)S\mathbf{e}(t-d) \\ & - \int_{t-L}^{t} \mathbf{y}^T(\sigma)R\mathbf{y}(\sigma)d\sigma - \frac{1}{a}\int_{t-L}^{t} |\dot{\varepsilon}(\sigma)||\widetilde{\varepsilon}(t)|d\sigma \\ & - \frac{1}{a}\int_{t-d}^{t} |\dot{\xi}(\sigma)||\widetilde{\varepsilon}(t)|d\sigma + \eta_1 + \eta_2, \end{aligned} \tag{3.141}$$

where, $\bar{\Gamma}$ is obtained as

$$\begin{aligned} \bar{\Gamma} \triangleq & P^T \begin{bmatrix} \mathbf{0} & I \\ A_0 + A_1 & -I \end{bmatrix} + \begin{bmatrix} \mathbf{0} & A_0 + A_1 \\ I & -I \end{bmatrix} P \\ & + \begin{bmatrix} S & 0 \\ 0 & LR \end{bmatrix}, \end{aligned} \tag{3.142}$$

$$\eta_1 \triangleq -2\int_{t-d}^{t} \bar{\mathbf{e}}^T(t)P^T\mathbf{y}(s)ds, \tag{3.143}$$

$$\eta_2 \triangleq 2\bar{\mathbf{e}}^T(t)P^T \begin{bmatrix} \mathbf{0} \\ \mathbf{E}(t) \end{bmatrix} \tag{3.144}$$

Under the following condition [36]

$$\begin{bmatrix} R & U \\ U^T & Z \end{bmatrix} \geq 0, \tag{3.145}$$

where $U = [U_1, \quad U_2]$.

η_1 can be rearranged as

$$\eta_1 \leq \int_{t-L}^{t} \mathbf{y}^T(s)R\mathbf{y}(s)ds + 2\mathbf{e}^T(t)\big(U - [\mathbf{0} \quad A_1^T]P\big)\bar{\mathbf{e}}(t) - 2\mathbf{e}^T(t-d)\big(U - [\mathbf{0} \quad A_1^T]P\big)\bar{\mathbf{e}}(t) + L\bar{\mathbf{e}}^T(t)Z\bar{\mathbf{e}}(t), \tag{3.146}$$

with matrix Z defined as

$$Z \triangleq \begin{bmatrix} Z_1 & Z_2 \\ * & Z_3 \end{bmatrix}. \tag{3.147}$$

On the other hand, differentiating W_2 along the trajectories of Eq. (3.129) gives

$$\begin{aligned} \dot{W}_2(t) &= \frac{1}{2a}(\widetilde{\varepsilon}^2(t) - \widetilde{\varepsilon}^2(t-L)) \\ &= \frac{1}{2a}(\widetilde{\varepsilon}(t) - \widetilde{\varepsilon}(t-L))(\widetilde{\varepsilon}(t) + \widetilde{\varepsilon}(t-L)) \\ &= \frac{1}{2a}\bar{\varepsilon}(t)(2\widetilde{\varepsilon}(t) - \bar{\varepsilon}(t)) \\ &= \frac{1}{a}\bar{\varepsilon}(t)\widetilde{\varepsilon}(t) - \frac{1}{2a}\bar{\varepsilon}^2(t), \end{aligned} \tag{3.148}$$

where $\bar{\varepsilon}(t) \triangleq \widetilde{\varepsilon}(t) - \widetilde{\varepsilon}(t-L)$.
I further work on W_2 as, with the definition $\xi(t-d) \triangleq \widehat{\varepsilon}(t-d) - \widehat{\varepsilon}(t-d-L)$,

$$\begin{aligned} \dot{W}_2(t) &\leq \frac{1}{a}\bar{\varepsilon}(t)\widetilde{\varepsilon}(t) \\ &= \frac{1}{a}((\varepsilon(t) - \varepsilon(t-L)) - (\widehat{\varepsilon}(t-d) - \widehat{\varepsilon}(t-d-L)))\widetilde{\varepsilon}(t) \\ &= \frac{1}{a}((\varepsilon(t) - \varepsilon(t-L)) - \xi(t)\widetilde{\varepsilon}(t) + (\xi(t)\widetilde{\varepsilon}(t) - \xi(t-d)\widetilde{\varepsilon}(t)) \\ &= \frac{1}{a}(\int_{t-L}^{t} \dot{\varepsilon}(\sigma)\widetilde{\varepsilon}(t)d\sigma - \xi(t)\widetilde{\varepsilon}(t) + \int_{t-d}^{t} \dot{\xi}(\sigma)\widetilde{\varepsilon}(t)d\sigma) \\ &\leq \frac{1}{a}(\int_{t-L}^{t} |\dot{\varepsilon}(\sigma)||\widetilde{\varepsilon}(t)|d\sigma - \xi(t)\widetilde{\varepsilon}(t) + \int_{t-d}^{t} |\dot{\xi}(\sigma)||\widetilde{\varepsilon}(t)|d\sigma). \end{aligned} \tag{3.149}$$

The summation of the above two Lyapunov functionals ($W \triangleq W_1 + W_2$) can be

reduced to

$$\begin{aligned}\dot{W}(t) \leq\ & \bar{\mathbf{e}}^T(t)\bar{\Gamma}\bar{\mathbf{e}}(t) - (1-\dot{d})\mathbf{e}^T(t-d)S\mathbf{e}(t-d) \\ & + 2\mathbf{e}^T(t)\big(U - [\mathbf{0} \quad A_1^T]P\big)\bar{\mathbf{e}}(t) \\ & - 2\mathbf{e}^T(t-d)\big(U - [\mathbf{0} \quad A_1^T]P\big)\bar{\mathbf{e}}(t) \\ & + L\bar{\mathbf{e}}^T(t)Z\bar{\mathbf{e}}(t) + 2\bar{\mathbf{e}}^T(t)P^T \begin{bmatrix} \mathbf{0} \\ \mathbf{E}(t) \end{bmatrix} - \frac{1}{a}\xi(t)\widetilde{\varepsilon}(t). \end{aligned} \tag{3.150}$$

Letting $J = [\mathbf{e}(t) \quad \mathbf{y}(t) \quad \mathbf{e}(t-d)]^T$, I rewrite Eq. (3.150) as

$$\begin{aligned}\dot{W}(t) \leq & J^T\Gamma J + 2\bar{\mathbf{e}}^T(t)P^T \begin{bmatrix} \mathbf{0} \\ \mathbf{E}(t) \end{bmatrix} - \frac{1}{a}\xi(t)\widetilde{\varepsilon}(t), \end{aligned} \tag{3.151}$$

where Γ is a $3n \times 3n$ matrix, obtained as

$$\Gamma = \begin{bmatrix} \phi & P^T \begin{bmatrix} \mathbf{0} \\ A_1 \end{bmatrix} - U \\ * & -(1-l)S \end{bmatrix}, \tag{3.152}$$

where

$$\begin{aligned}\phi \triangleq & P^T \begin{bmatrix} \mathbf{0} & I \\ A_0 & -I \end{bmatrix} + \begin{bmatrix} \mathbf{0} & I \\ A_0 & -I \end{bmatrix}^T P + LZ \\ & + \begin{bmatrix} S & \mathbf{0} \\ \mathbf{0} & LZ \end{bmatrix} + \begin{bmatrix} U \\ \mathbf{0} \end{bmatrix} + \begin{bmatrix} U \\ \mathbf{0} \end{bmatrix}.^T \end{aligned} \tag{3.153}$$

According to [36], matrix Γ is negative when $U = [\mathbf{0} \quad A_1^T]P$. I rearrange the middle term on the right-hand side of Eq. (3.151) as

$$2\bar{\mathbf{e}}^T(t)P^T \begin{bmatrix} \mathbf{0} \\ \mathbf{E}(t) \end{bmatrix} = 2\bar{\mathbf{e}}^T(t) \begin{bmatrix} P_2^T\mathbf{E}(t) \\ P_3^T\mathbf{E}(t) \end{bmatrix} = 2\bar{\mathbf{e}}^T(t)D\widetilde{\varepsilon}(t), \tag{3.154}$$

with matrix D defined as

$$\begin{aligned} & D \triangleq \\ & [P_2^{1,4} \quad P_2^{2,4} \quad P_2^{3,4} \quad P_2^{4,4} \quad P_3^{1,4} \quad P_3^{2,4} \quad P_3^{3,4} \quad P_3^{4,4}]^T, \end{aligned} \tag{3.155}$$

where $P_2^{i,j}, P_3^{i,j}$ denote the (i,j)th element of P_2, P_3, respectively.

If I design $\xi(t)$ such that

$$\xi(t) = 2a\bar{\mathbf{e}}^T(t)D, \tag{3.156}$$

as long as matrices P_2, P_3 remain positive, Eq. (3.151) is reduced to

$$\dot{W}(t) \leq J^T \Gamma J. \tag{3.157}$$

As $\Gamma < 0$, I have $\dot{W}(t) < 0$. Therefore, the closed-loop system is globally asymptotically stable.

CHAPTER IV

Computational Model of Human Motor Control

Humans are endowed with a remarkable ability to execute limb movements even in the presence of changing loads arising from interaction with the environment or variation in properties of one's sensorimotor system. For example, humans are able to move a box from one place to another even if the weight and inertial properties of the box and contents are unknown. Even when the arm is perturbed gradually or abruptly during the task, a corrective force will be generated to compensate for the perturbation and the box will be placed at the goal position in the end.

To explain these motor abilities, the so-called internal model has been proposed in the field of human motor behavior. The internal model is a hypothesized controller residing in the motor cortex and/or cerebellum. Internal models are constructed on the basis of accumulated past experience interacting with the environment and are used to produce anticipatory control (feedforward control) actions. The internal model has been represented in computational formulations and these can be run in simulation to produce movement that matches human behavior, including behavior under perturbations. These include behaviors that cannot be described by the so-called equilibrium-point hypothesis.

According to the equilibrium point hypothesis, movements are generated by setting desired muscle equilibrium lengths and response to perturbation is governed by a feedback response that uses the muscle equilibrium as a reference. However, humans and animals with impaired feedback loops are still able to produce intended movements. Also, several pieces of empirical evidence demonstrate that stiffness of the limb during movement is much lower than that predicted by equilibrium-point control [41, 109]. Moreover, substantial delays exist in feedback loops, which calls into question the ability of feedback mechanisms to explain human motor behavior. With these substantial delays, equilibrium-point control cannot describe fast movements [66, 99, 102]. Alternative explanations involving complex trajectories of the

equilibrium point to produce rapid movements seem unlikely [6, 70, 90]. McIntyre and Bizzi (1993) and De Lussanet et al. (2002) proposed extensions of equilibrium-point control by considering contraction velocity trajectories that promote stability and lower the required stiffness [21, 77]. But these extended schemes still failed to reproduce fast movements [102]. Kistemaker et al. (2006) attempted to capture fast movements with equilibrium-point control in an intermittent way using a realistic musculoskeletal model of the human arm [64]. But they used a short delay value (25 ms).

Internal models are thought to participate in motor control in two forms: inverse models and forward models. An inverse model can be used to compute an appropriate motor command that, through the physical dynamics of the environment, would produce a desired movement. A forward model is useful for predicting sensory feedback that can be expected as a consequence of a given motor command. Such expected sensory feedback may be compared to incoming sensory feedback to make excursions from expectation immediately available to the brain.

However, it remains an open question as to how the brain acquires internal models. Does the brain identify models of the musculoskeletal system and each environment with which one interacts? In experiments in [25], participants were asked to familiarize themselves through practice with the dynamics of a mass-spring system attached to their hand. In a catch trial, a different mass and a different stiffness were presented. By showing that behaviors of participants in the catch trial were predicted by a model-based controller while feedback control alone failed to predict them, the authors suggested that the participants identified the mass and stiffness of the interacting system and could even predict the mass trajectory. But identifying the structure and parameters of dynamical systems and external perturbations during movements may impose highly demanding practice and computational loads.

A study by Shadmehr and Mussa-Ivaldi (1994) and several follow-up studies showed that hypothetical internal models can be formed or adapted to new external loads but many trials are required (near 250 trials) [7, 53, 65, 100, 105]. However, such trials might not be necessary to build an internal model. Even without practice, humans possess the ability to reach a target position even under perturbations during fast movements [30, 98]. The so-called equifinality property, defined as the ability of a system to reach a target position under transient mechanical perturbations, was exhibited in movements perturbed within short time periods (under 70 ms) within a given trial [102].

Also, in an experimental study of [68] that imposed an inertia change on a

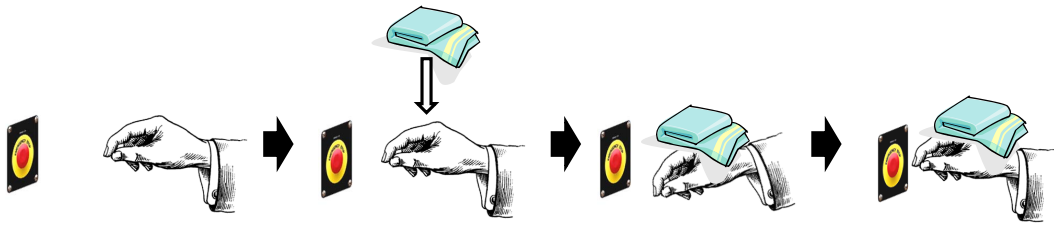

Figure 4.1: Equifinality: the ability of a system to reach a target position even under transient mechanical perturbations.

subjects limb during a reaching task, it was revealed that the participants did show savings toward only a change in the inertia property they experienced most recently. Even if subjects adapted to an effective inertia on their arm, the adaptation on the inertia disappeared if they experienced another inertia property afterward. In another reaching study conducted by [101], stochastic perturbations were varied from trial to trial. This study suggests that neural structures were modified with only a short-term memory, that is, only a memory obtained in the previous trial.

Several researchers have attempted to construct the relationship between past and current behaviors using linear models [27,29,101,110,121]. Most of these studies found that the current movement is influenced by only the most recent previous movement.

A motor command to a given limb and that limb's position (and its derivatives) are in a certain input-output relationship; the input acts on the neuromuscular system and any environment in contact with the limb, while the output reflects the dynamic response. Although it is difficult to identify the properties of the system and environments with only the input and output available, the quantitative relationship between the input and output can be used as a clue to estimate the dynamics of the neuromuscular system for the purpose of formulating subsequent control actions. With an estimate of the limb and environment dynamics made at the previous step, the musculoskeletal system and environment dynamics in the current step could be compensated. In other words, the estimate can be used in place of a system model.

In fact, time delay control (TDC) utilizes just that mechanism [125]; the relationship between input and output signals are used to estimate the dynamics of the system under control. Time delay control is generally accepted as a simple and powerful control architecture in the robotics area. The system dynamics and injected perturbations are estimated using a motor command and its sensed consequence at the previous sample in a digital implementation, assuming that the sampling time is sufficiently small. System dynamics and perturbations are immediately compensated based on the recent movement consequence. Thus TDC is able to cancel nonlinear

dynamics and disturbances even when a system model is not available. The control system can cancel nonlinear dynamics without the use of high gain control.

In this thesis, I address the possibility that human motor control produces movement in a manner similar to the operation of TDC. It would be possible that an estimate from the input-output relationship enables the brain to control a limb without having a precise model of the limb available. If so, this mechanism could provide a good explanation as to human capability for rapid movements regardless of whether and how much external loads are involved. A substantial learning process is not required.

However, biological systems have substantial delays on feedback loops, which are at least 30 ms [69]. With such long sensory delays, estimating the current dynamics and perturbations using a copy of a motor command and its output delayed on sensory feedback would be inaccurate. It may be required to resolve this sensory delay issue. In 1993, Miall and colleagues proposed a computational model of human control mechanisms based on the Smith predictor [79]. They borrowed the Smith predictor from control engineering to describe behaviors of biological systems. The Smith predictor is a control scheme that had been devised more than 3 decades earlier for factory processes with substantial feedback delays. In essence, the Smith predictor explains how biological systems might overcome delays on feedback loops. However, the Smith predictor has inverse and forward model components. Thus the Smith predictor is a model-based controller; it requires a system model. In this study, I design a control scheme that has a close relationship to the Smith predictor in its ability to handle delays, but is free of system models. The proposed control could be described as a model-free version of the Smith predictor.

Simulation studies are conducted to check the feasibility of the proposed control for predicting fast movements. It is considered difficult to describe fast movements using feedback control alone due to the inherent neurobiological delay in the human control system. Anticipatory control needs to be involved to make an appropriate action before sensory information is available. Also, dynamics compensation is required in quick movement with low muscle stiffness. Fast movements would pronounce the functioning of inverse and forward models in biological control systems.

4.1 Development of computational model

In the section, I present a brief explanation on time delay control (TDC) first. Then I design a human control model based on the principle of TDC. To accommodate

substantial delays of the biological sensory system, the proposed model takes the form of the Smith predictor.

Time delay control

Fig. 4.2 describes how TDC-type control works in moving a rigid body in comparison with PD-type control and model-based control. Assume that we try to move the rigid body to a desired angle. While PD-type control attaches a spring and damper the ends of which are anchored at the desired angle to the rigid body, model-based control, with a system model, converts the rigid body to a massless and frictionless one, eliminating the system dynamics. And the control includes a spring and damper between the converted rigid body and the desired angle. In a similar way, TDC-type control first converts the rigid body to a unit-mass and frictionless one, and then includes a spring and damper between the converted rigid body and the desired angle in addition to a pushing torque $\ddot{\theta}_d$. But TDC-type control cancels out the system dynamics using information from a previous motor command and its output (state).

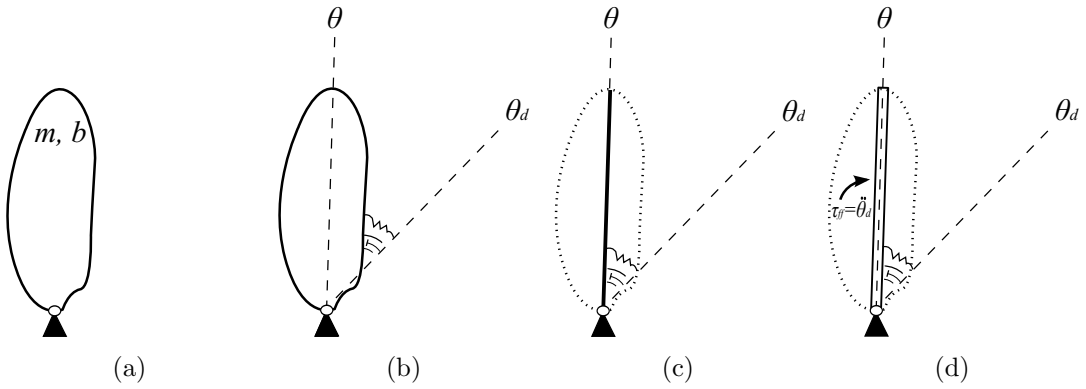

Figure 4.2: Schematics of (a) a rigid body, and (b) PD-type control, (c) model-based control, and TDC-type control on the rigid body.

To elaborate TDC-type control mathematically, I take the 1 degree of freedom (DOF) rigid body for example, which is depicted in Fig. 4.2(a). With $I(m), b$ defined as the inertia and friction coefficient, respectively, the equation of motion of the model is expressed as

$$I\ddot{\theta} + b\dot{\theta} + mglcos\theta = \tau + d. \tag{4.1}$$

Symbol θ denotes the angle; g the gravitational constant; l the length between the center of mass and the joint; d a disturbance; τ the torque exerted on the limb.

The system dynamics plus disturbance d that need to be identified for control are grouped into one term, introducing a parameter $\bar{m}$, as follows:

$$\bar{m}\ddot{\theta} + (-\bar{m}\ddot{\theta} + I\ddot{\theta} + b\dot{\theta} + mglcos\theta - d) = \bar{m}\ddot{\theta} + h = \tau, \tag{4.2}$$

where

$$h \triangleq -\bar{m}\ddot{\theta} + I\ddot{\theta} + b\dot{\theta} + mghlcos\theta - d. \tag{4.3}$$

It is acceptable to assume that the term h is piece-wise continuous if disturbance d is bounded. This implies that the value of the term h at a time point can be approximated by its value at another time point. The closer the gap between the two time points, the more accurate the approximation can be made. An estimate of the value of the term h can be obtained in this way:

$$\begin{aligned} &h \approx h_{-1}, \\ &\hat{h} = h_{-1} = \tau_{-1} - \bar{m}\ddot{\theta}_{-1}, \end{aligned} \tag{4.4}$$

where subscript -1 indicates a value at the previous sample.

If the value of $(\tau_{-1} - \bar{m}\ddot{\theta}_{-1})$ is included in the motor command to the system, the system becomes a unitmass in the ideal case, as exhibited in Fig. 4.2(d). Next, the unit-mass limb requires additional torques to follow the desired angle. The control injects feedforward torque $(\ddot{\theta}_d)$ and restoring torque that can be realized by placing a spring and damper between the limb and the desired angle.

Then, the control law is expressed as

$$\tau = \tau_{-1} - \bar{m}\ddot{\theta}_{-1} + \bar{m}\ddot{\theta}_d + D(\dot{\theta}_d - \dot{\theta}) + K(\theta_d - \theta), \tag{4.5}$$

where D, K are viscosity and stiffness, respectively.

The control law consists of three components: cancellation of system dynamics, feedforward, and feedback. I have elaborated cancellation of system dynamics above. As for the feedforward component, it should be proportional to the acceleration of the desired trajectory $(\ddot{\theta}_d)$, because the controlled system is an acceleration control system [54]. The feedforward control utilizes the inverse dynamics of the system; the torque component is created by the acceleration of the desired trajectory, which is programmed according to an intended movement. In the case that the initial condition of the arm is quiescent and no uncertainties exist, the actual position of the

arm converges to the desired one [54]. The third component, feedback control, plays a role in diminishing the error between the desired trajectory and actual trajectory measured by the sensory systems.

If the estimation error ϵ is defined as

$$\epsilon \triangleq \bar{M}^{-1}(h - \hat{h}), \tag{4.6}$$

the closed-loop dynamics can be expressed as follows:

$$\ddot{e} + D\dot{e} + Ke = \epsilon, \tag{4.7}$$

where $e \triangleq \theta_d - \theta$.

The control gains K and D shape the error dynamics; they determine under, critical, and over damping at convergence. Also, these gains are related to how fast the error is suppressed. From the closed-loop dynamics (4.7), we know that a smaller estimation error leads to more accurate tracking of the limb relative to the planned trajectory.

Gain $\bar{m}$ determines how accurately dynamics estimation is made; the gain affects the difference between h and $\hat{h}$, which eventually affects the tracking error [52].

First, I re-express the system (4.1) as

$$\tau = m\ddot{\theta} + f, \tag{4.8}$$

with the definitions $m \triangleq I, f \triangleq b\dot{\theta} + mglcos\theta - d$.

The closed-loop dynamics in the aspect of the estimation error ϵ can be described as

$$\epsilon = (m^{-1}\bar{m} - 1)\epsilon_{-1} - \eta_{-1} - (m^{-1}\bar{m} - 1)\zeta_{-1}, \tag{4.9}$$

where

$$\eta_{-1} \triangleq (m^{-1}m_{-1} - 1)\ddot{\theta}_{-1} + f_{-1} - f, \tag{4.10}$$

$$\zeta_{-1} \triangleq v - v_{-1}, \tag{4.11}$$

$$v \triangleq \ddot{\theta}_d - D\dot{e} - Ke. \tag{4.12}$$

From the viewpoint of the estimation error ϵ, the terms η, ζ in Eq. (4.9) are regarded as forcing functions that are bounded in the case of a sufficiently small

sampling period. The coefficient $(m^{-1}\bar{m} - 1)$, in particular, the tuning gain $\bar{m}$, determines the convergence rate of ϵ, which eventually affects the tracking error, as seen in (4.7).

Smith predictor

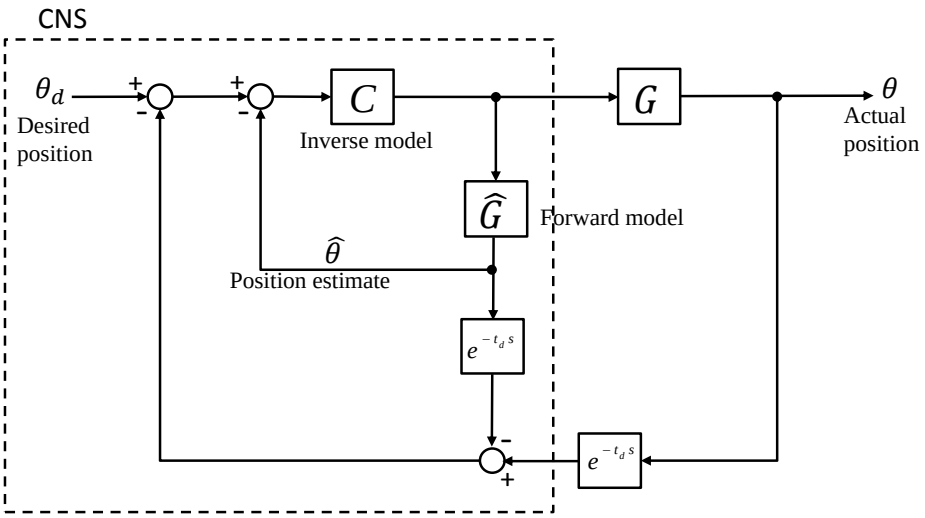

Figure 4.3: Smith predictor.

The Smith predictor, proposed by Smith in 1959 [106], is a form of controller for systems with delays, as shown in Fig. 4.3. The outer control loop feeds back the actual state of the system G, but due to the delay on feedback loop, use of the outer loop alone would not provide satisfactory control performance and alone lead to instability in the worst case. So, the inner loop is added to send the (estimated) current state to the controller C. The current state is estimated using a system model $\hat{G}$ that is supposed to be simulated with a copy of the control input. And the Smith predictor delays the estimated state as long as the actual state is delayed so that the delayed actual state and delayed estimated state cancel one another. If the perfect match between these two delayed states is made, the controller C can show control performance with no influence of delay on the outer feedback loop. Miall and his colleagues employed this Smith predictor in human control modelling to describe good performance even in the face of sensory delays [79]. They matched controller C and a system model $\widehat{G}$ with the inverse model and forward model in the cerebellum, respectively.

Proposed control

TDC is tolerant to modeling error (it does not require a precise system model), but it is tolerant to sensory delays. The Smith predictor is tolerant to sensory delays, but it is vulnerable to modeling error. I take the form of the Smith predictor to

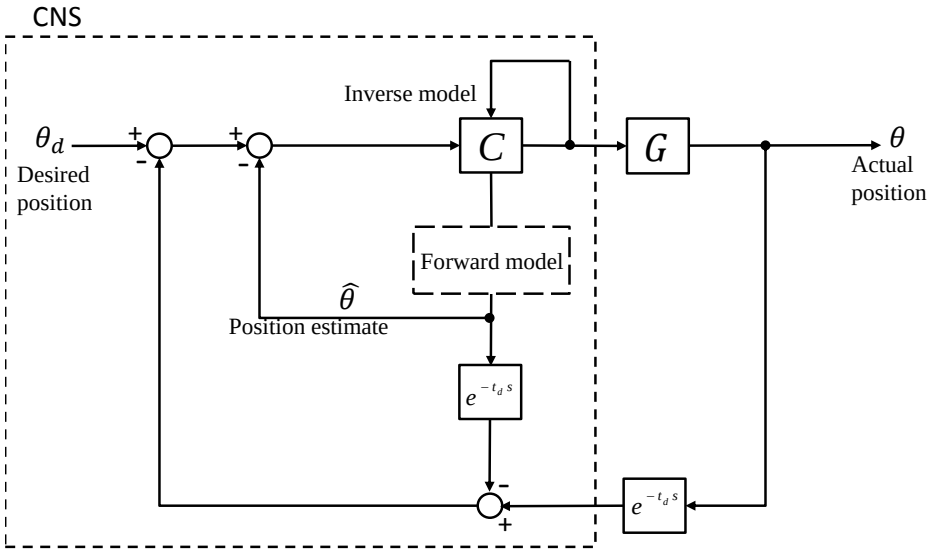

Figure 4.4: Proposed human control model.

liberate TDC from the sensory delay issue.

For performing the function of inverse model, the TDC control law can be placed in controller C in the Smith predictor (Fig. 4.3). For performing the function of forward model to estimate the current state of the system, it is possible to construct estimating computation grounded on the characteristic of TDC. That is, TDC pushes the controlled system to behave according to desired dynamics. Assuming that the estimation error ϵ =0, the closed-loop dynamics becomes

$$\ddot{e} + D\dot{e} + Ke = \ddot{\theta}_d - \ddot{\theta} + D(\dot{\theta}_d - \dot{\theta}) + K(\theta_d - \theta) = 0. \tag{4.13}$$

From the dynamics, it is possible to obtain estimates of states $\theta, \dot{\theta}$ and $\ddot{\theta}$.

$$\begin{bmatrix} \widehat{\theta} \\ \dot{\widehat{\theta}} \end{bmatrix} = e^{At} \begin{bmatrix} \widehat{\theta}_0 \\ \dot{\widehat{\theta}}_0 \end{bmatrix} + \int_0^t e^{At'} \begin{bmatrix} 0 \\ 1 \end{bmatrix} p(t - t')dt', \tag{4.14}$$

$$\ddot{\widehat{\theta}} = - D\dot{\widehat{\theta}}(t) - K\widehat{\theta}(t) + p(t), \tag{4.15}$$

where

$$A = \begin{bmatrix} 0 & 1 \\ -K & -D \end{bmatrix}, \tag{4.16}$$

$$p(t) = \ddot{\theta}_d(t) + D\dot{\theta}_d(t) + K\theta_d(t). \tag{4.17}$$

The initial values of estimates $\widehat{\theta}, \dot{\widehat{\theta}}$ can be assumed to be the same as those of the actual states $\theta, \dot{\theta}$.

With the proposed forward model, the current states are estimated and fedback to the controller. Note that this forward model is model-free. If the forward model is plugged into the place of $\widehat{G}$ in the Smith predictor, the block diagram of the control model can be converted into that shown in Fig. 4.4. As in the Smith predictor, the estimates $\widehat{\theta}, \dot{\widehat{\theta}}$ from the forward model are intentionally delayed to compensate for the actual states that are delayed on the sensory feedback loop.

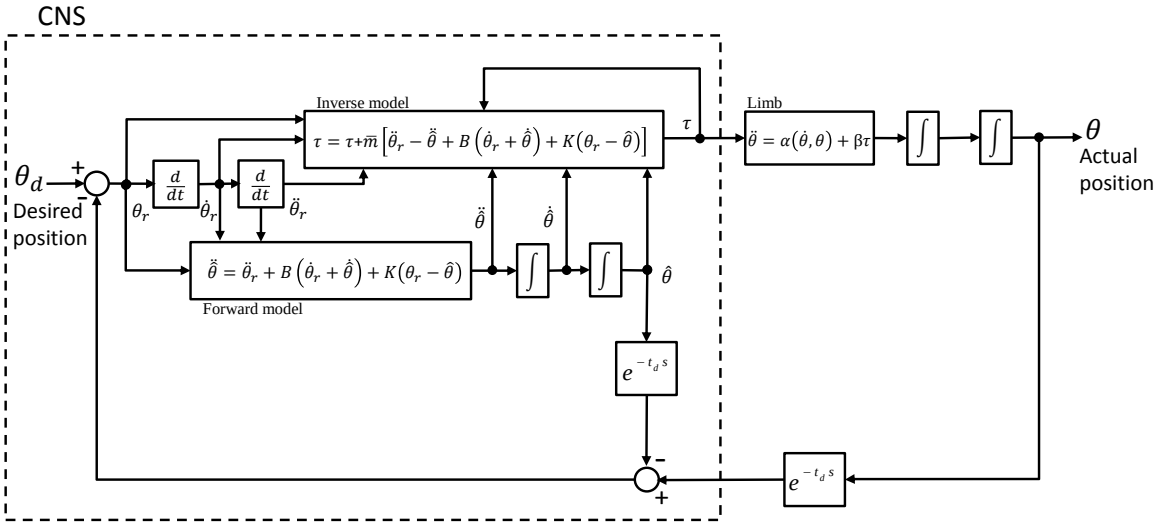

Figure 4.5: Proposed human control model (detailed version).

In the proposed control, the delayed actual position and delayed estimates are compared. The difference between them is compared with the desired position. These differences can be expressed as θ_r:

$$\theta_r(t) \triangleq \theta_d(t) - (\theta(t - t_d) - \widehat{\theta}(t - \widehat{t}_d)), \tag{4.18}$$

where t_d denotes the time delay on the feedback loop and $\widehat{t}_d$ is an estimate of t_d.

Then, the controller forces the controlled system to follow θ_r, reflecting that the controller receives the current state estimated by the forward model. The control law of the proposed model is designed as

$$\tau = \tau_{-1} - \bar{m}\ddot{\theta}_{-1} + \bar{m}\ddot{\theta}_r + D(\dot{\theta}_r - \dot{\widehat{\theta}}) + K(\theta_r - \widehat{\theta}). \tag{4.19}$$

According to the closed-loop dynamics that the controller pursues, one of the

formulations for the forward model (4.20) needs to be modified:

$$p(t) = \ddot{\theta}_r(t) + D\dot{\theta}_r(t) + K\theta_r(t). \tag{4.20}$$

Fig. 4.5 presents a detailed version of block diagram of the proposed control.

4.2 Model validation

In this section, I validate the TDC-inspired human control model through a series of simulation studies, in aspects of fast movements of a single joint and multi joints. As the first step, I try to check if the proposed computational model follows empirical outputs obtained from human subject experiments.

4.2.1 Arm model implementation

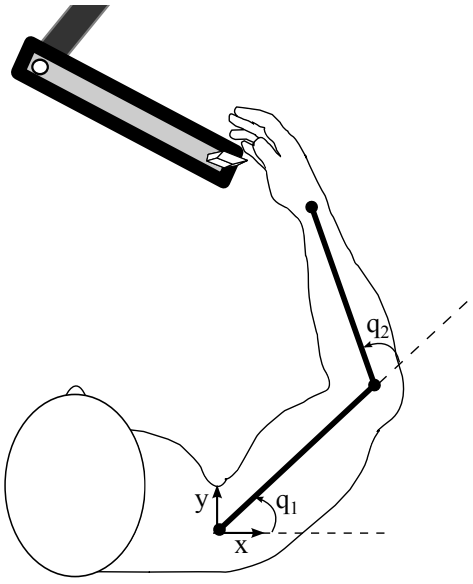

Figure 4.6: Schematic of reaching experiments

The experimental data I revisit in this study were produced by horizontal arm movements, neglecting the gravitational force. The arm movement is modeled with a 2 degree-of-freedom (DOF) robot system, as presented in Fig. 4.6. With $\mathbf{q}(t)$, and τ_E denoting the joint angle trajectories and the torque from environments, respectively, the model of limb movements can be described as follows

$$\mathbf{H}(\mathbf{q})\ddot{\mathbf{q}} + \mathbf{C}(\mathbf{q}, \dot{\mathbf{q}})\dot{\mathbf{q}} = \tau(t) + \tau_E(t), \tag{4.21}$$

where

$$\mathbf{H}(\mathbf{q}) = \begin{bmatrix} H_{11} & H_{12} \\ H_{21} & H_{22} \end{bmatrix}, \tag{4.22}$$

$$\begin{aligned} H_{11} \triangleq & J_1 + J_2 + M_1 l_{m1}^2 + M_2(l_1^2 + l_{m2}^2 + 2 l_1 l_{m2} \cos q_2) \\ H_{12} = & H_{21} \triangleq J_2 + M_2(l_{m2}^2 + l_1 l_{m2} \cos q_2) \\ H_{22} \triangleq & J_2 + M_2 l_{m2}^2, \end{aligned}$$

and

$$\mathbf{C}(\mathbf{q}, \dot{\mathbf{q}})\dot{\mathbf{q}} \triangleq \begin{bmatrix} -M_2 l_1 l_{m2} \sin q_2 (2\dot{q}_1 + \dot{q}_2)\dot{q}_2 \\ M_2 l_1 l_{m2} \sin q_2 \dot{q}_1^2 \end{bmatrix}. \tag{4.23}$$

The parameters of the arm are adopted from [11]; for the upper arm, $J_1 = 0.0141$ (kgm^2), $M_1 = 1.93$ (kg), $l_1 = 0.31$ (m), $l_{m1} = 0.165$ (m), for the upper arm, $J_2 = 0.0188$ (kgm^2), $M_2 = 1.52$ (kg), $l_2 = 0.34$ (m), $l_{m2} = 0.19$ (m). The lengths l_{m1} and l_{m2} denote the distances between the center of mass and the proximal joint.

I assume that human subjects try to track their hand to a minimal-jerk planned trajectory in joint space and Cartesian space according to the given task. From [34], the desired (planned) trajectory is designed as

$$q_d(t) = q_0 + (q_f - q_0)(6t'^6 - 15t'^5 + 10t'^4), \quad t' = \frac{t}{T}, \tag{4.24}$$

where q_0, q_f denote the initial and final positions of the hand, T denotes the duration of the movement.

I consider feedback signals as an amalgam of all achievable sources of sensory information about limb movements including proprioceptive and visual feedback. The sensory delay t_d is set as 65 ms. And it is assumed that the CNS estimates the sensory delay so $\widehat{t_d}$ is set to 65 ms (the main purpose of simulations in this study is to see the effect of dynamics compensation of the proposed control on movements). Simulations are conducted in Matlab using ODE45. I utilize the optimization toolbox in Matlab to obtain control gains that give the best fit between simulated trajectory and empirically observed trajectory.

4.2.2 Movements to be reproduced

Fast movement of a single joint

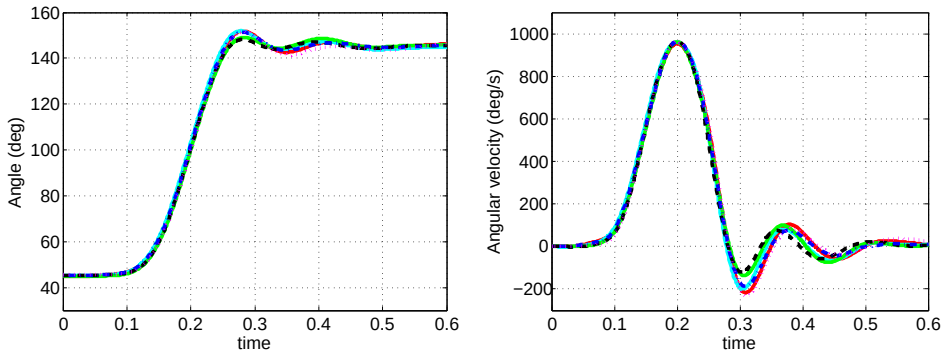

(a) (b)

Figure 4.7: Fast single-joint movement-experimental results provided by [64]: (a) arm position and (b) velocity.

Kistemaker et al. (2006) investigated fast single joint (elbow) movements [64]. Participants were asked to direct their hand from the marked middle of one block to the marked middle of another block as fast as possible, once an auditory cue was presented. Participants practiced until they could move quickly to the target with minimal overshoot.

For simulation, I lock the shoulder joint of the 2 DOF model (4.21) to reproduce the fast single joint movements by participants. The values of K and D are selected as 100 and 20, respectively. The value of gain $\bar{m}$ is arbitrarily set to 0.015. For a comparative study, the Smith predictor [79] and an equilibrium-point controller [77] are simulated. For the Smith predictor, I provide it with the perfect system model and delay model. The delay on the feedback loop is set to 65 ms. PD control is adopted as the inverse model, with the P gain set as 92 and the D gain set as 38. For the equilibrium-point controller, I put a delay of 65 ms onto the position feedback loop while a delay of 25 ms is imposed on the velocity feedback loop. The P gain and D gain are tuned to 0 and 0.76, respectively (the velocity feedback loop is faster that the position feedback loop). Note that the control gains are tuned by the optimization toolbox until the best match with the planed trajectory is achieved. These gains, with a reasonable range, gives the minimum deviation from the desired trajectory between 0.1 s and 0.3 s

Fast movement of multi joints

Also, I attempt to reproduce a fast movement with multi joints. Different from single-joint movements, multi-joint movements involve interaction torques including inertia torques from movements of other joints, centripetal torques and Coriolis torques. These interaction torques need to be compensated to make movements, in

particular, rapid movements [102]. I check whether the proposed control compensates for interaction torques by reproducing a fast movement presented in [66]. Koike and Kawato (1995) asked participants to to move their hand ahead of their body in different directions on a desk for 500 ms 750 ms using the shoulder and elbow joints [66]. Among these five movement paths, I select a transverse one (from point(-0.2 m, 0.5 m) to point(0.35 m, 0.25 m)) that produces more significant deviation from the desired path. For simulation, the movement duration is set to 500 ms.

Simulation for this task is made in Cartesian space. The Jacobian matrix of the 2 DOF arm model is given as

$$\mathbf{J}(\mathbf{q}) \triangleq \begin{bmatrix} -l_1 \sin q_1 - l_2 \sin(q_1 + q_2) & -l_2 \sin(q_1 + q_2) \\ l_1 \cos q_1 + l_2 \cos(q_1 + q_2) & l_2 \cos(q_1 + q_2) \end{bmatrix}, \tag{4.25}$$

The desired trajectory is designed in Cartesian space as a minimum-jerk trajectory and converted to the desired trajectory of each joint using the inverse kinematics of the 2 DOF arm. The control input (4.19) is applied to the shoulder joint and elbow joint. The values of gain $\bar{m}$ for the shoulder joint and elbow joint are arbitrarily set to 0.27 and 0.06, respectively. And the optimization toolbox tunes the control gains: the P gain and D gain for the shoulder joint are 271 and 180, respectively, and the P gain and D gain for the elbow joint are 270 and 2.3, respectively. Also, simulation with the equilibrium-point control proposed in [77] follows. The P gain and D gain are set to 2.5 and 0.6, respectively , for both the shoulder and elbow joints. These values give the best fit in terms of deviation and smoothness, as in [102]. A delay of 65 ms is put onto the position feedback loop while a delay of 25 ms on the velocity feedback loop.

4.3 Simulation results

Fast movement of a single joint

Fig. 4.8 presents the simulation results of the fast single-joint movement by the Smith predictor, equilibrium-point control and proposed control. I first focus on the results of the Smith predictor and equilibrium-point control. The Smith predictor outputs a minimum-jerk trajectory, whereas equilibrium-point does not. Equilibrium-point control shows bell-shaped trajectory but it is not of the minimum jerk. Given that biological systems make minimum-jerk movements, Equilibrium-point control that does not have a device to deal with sensory delays is unable to capture biological systems. This would support the existence of forward model that estimates the

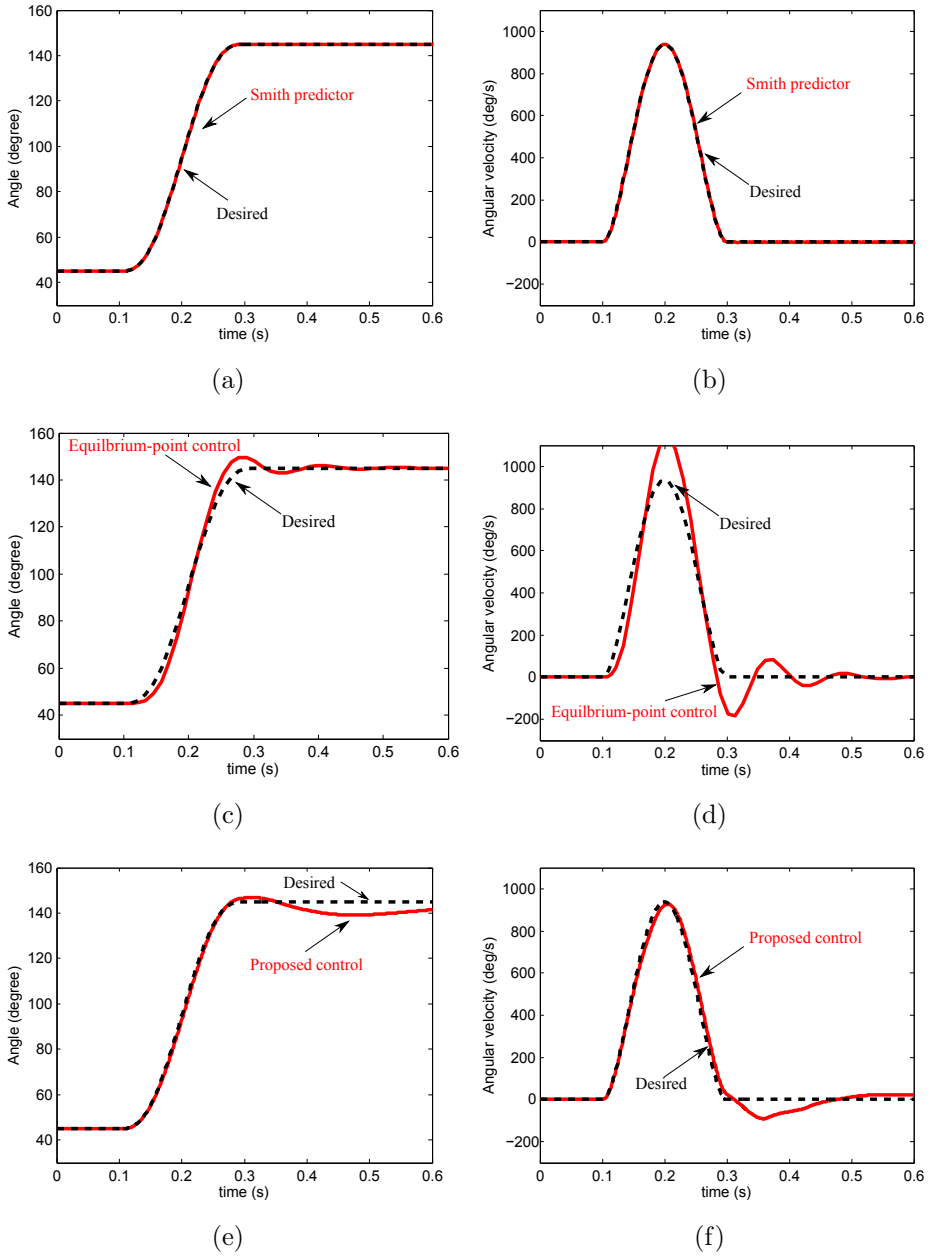

Figure 4.8: Fast single-joint movement-simulation results (position and velocity) by (a), (b) the Smith predictor, (c), (d) the equilibrium-point control, and (g), (f) the proposed control.

current state corresponding to a motor command. The simulation results show that the proposed control produces a minimum-jerk movement. This at least implies that the forward model works in the presence of the delay on sensory feedback. In the empirical results, oscillations around the end of movement are exhibited (see Fig. 4.7). It is likely that these fast movements are at least partially stopped using

co-contraction of muscles near the end of the movement. The oscillations would result from the nonlinear activation dependent viscoelasticity of muscles. As stiffness and viscosity are assumed constant in the simulation, I do leave the existence or nonexistence of oscillations in the simulation results out of consideration.

Fast movement of multi joints

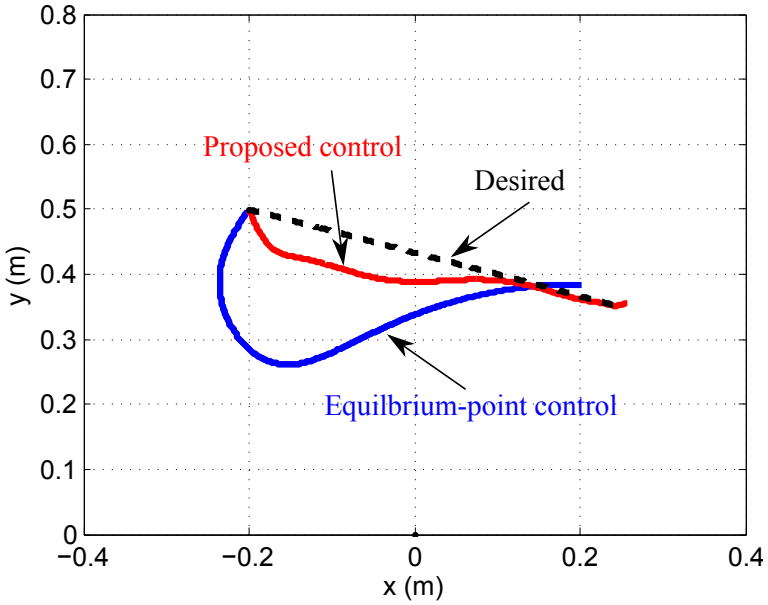

Figure 4.9: Fast multi-joint movement-simulation results (position) by equilibrium-point control and the proposed control for 500 ms from movement start.

As mentioned above, multi-joint movements involve interaction torques that are dependent in a nonlinear fashion on motions at adjacent joints including inertia torques, centripetal torques and Coriolis torques. As movements get faster, the interaction toques increase gradually. These torques may need to be compensated so that an intended movement can be achieved. Fig. 4.9 shows the simulation results of a fast multi-joint movement. Equilibrium-point control exhibits a larger deviation from the desired trajectory. This indicates that enough dynamics compensation is not performed. Meanwhile, the proposed control shows a far smaller deviation in comparison with equilibrium-point control. This would suggest that the proposed control efficiently reduces the effect of the interaction torques through dynamics compensation, even without a system model.

4.4 Discussion

Time delay control (TDC) shows robust performance to model uncertainties, even not requiring substantial computational load. Using a motor command and its result at the previous sample, TDC estimates the controlled system dynamics interacting with environments. With no need of high stiffness and damping gains, TDC achieves accurate and robust tracking tasks. Humans show a remarkable ability to execute limb movements even in the presence of changes in environments as well as in the properties of the sensorimotor system. Even in the case that our arm is perturbed gradually or abruptly during the task, corrective torques will be generated to compensate for the perturbation and the arm will be positioned as planned in the end, even without high stiffness. These common points trigger a question regarding whether humans control their limbs in a similar way to TDC. In this study, we proposed a computational model of human control based on the TDC principles and evaluated the possibility that the model captures empirical phenomena.

4.4.1 Model of human control

The proposed computational model consists of inverse model and forward model as in usual computation models that support the existence of internal models in the brain [37, 79, 104, 111, 123, 124].

The inverse model of the proposed computation calculates a motor command that moves the controlled limb to a desired state. The inputs to the inverse model include an efferent copy of motor command and the position, velocity and acceleration values of the desired limb state and (estimated) actual limb state. A copy of descending command and its estimated corresponding acceleration of the limb cancels out the dynamics of the limb and environment, and desired dynamics is replaced that is formed by a combination of the position, velocity and acceleration of the limb with muscle viscoelasticity. I emphasize that a precise system model is not required in the inverse model.

The forward model estimates the actual limb state that is substantially delayed during signal transmission on feedback loops. As well, a precise system model is not required in the forward model. The forward model supposes that the inverse model realizes the desired dynamics during movements. The actual limb state is extracted from the desired dynamics.

How can this computation be realized in a real biological system?

The cerebellum receives afferents carrying sensory information on the limb and

reafferents carrying copies of motor command and information required for movements including a desired trajectory from the primary motor, somatosensory and parietal cortex. Efferent copies of descending motor commands could be transmitted by motor neurons. Brodmann area 5 in the parietal cortex would be thought as a desired trajectory composed of position, velocity and acceleration values [59, 102]. Kalaska et al. (1990) showed that excitations of Brodmann area 5 cells were correlated with position, velocity and acceleration [59]. Muscle length and velocity are measured through muscle spindles and mossy fibers [115]. The measured actual limb state ascends to the cerebral cortex and is inputted to the forward model after comparisons. As for the states dealt with by the forward model, mossy fibers as well as area 5 cells are thought to transmit the acceleration component in addition to the position and velocity components [114].

4.4.2 Fast movement

I checked the feasibility of the proposed control for fast movements. During fast movements of which duration is nearly as short as the delay on feedback loops involves in sensorimotor processing, the roles of inverse and forward model are pronounced. Those movements would be completed before sensory information affects. Even during movements while which sensory information gives an influence, online correction that depends only on sensory feedback could lead to instability.

In the simulation of a single-joint movement, I observed that while the Smith predictor reproduces the minimum-jerk trajectory perfectly, equilibrium-point control that does not contain any forward model cannot describe the fast movement with a duration of 0.2 s as in [66,99,102]. The simulation results between the Smith predictor and equilibrium-point control support the existence of forward model [5, 23]. The proposed control reproduces the minimum-jerk trajectory as well. This indicates that the proposed forward model in the form of the Smith predictor efficiently estimates the current states of the limb and feeds them back to the inverse model.

In the simulation of a multi-joint movement, I checked whether the proposed control compensates for system dynamics in multi-joint movements involving simultaneous motion at the shoulder and elbow. Interaction torques that arise at one joint (e.g., the shoulder) because of motion of limb segments about other joints (e.g., the elbow), which include inertia torques from movements of other joints, centripetal torques and Coriolis torques, disturb achieving planned movements. That is, these interaction forces act as disturbances that need to be compensated. In Fig. 4.6, equilibrium-point control shows a larger deviation from the desired trajectory than a

biological system exhibited [66]. Equilibrium-point control well describes a relatively slow movement with the same planed path but as the duration of movement gets short, the deviation from the planed path increases [102]. This means that equilibrium-point control with feedback control alone is not able to sufficiently compensate for the interaction torques that increase according to movement speed. Also, this result supports the role of inverse model in human movement. The proposed control shows a far smaller deviation. This suggests that the inverse model of the proposed control efficiently carries out dynamics compensation. Note that identifying interaction torques requires an explicit system model including the inertia and length of each segment of the limb (see Eq. (4.21)). But the proposed control does not require a system model. The proposed control builds inverse models using the relationship between the motor command and its responses. Through the compensation of the system dynamics and sensory delay, the proposed control capture the human's voluntary movements, which is in agreement with a study presented in [44].

CHAPTER V

Conclusion and Future Work

5.1 Conclusion

In this thesis I have addressed three rather distinct bodies of work. The common theme has been the analysis of mechanical interaction between the human and machine. I pay particular attention to the mechanical interaction of both the human and environment.

The contributions documented include:

1. Effect of Haptic Cues on the Human Motor System

- Demonstrates implicit learning with haptic cues applied to fingertips
- Shows error rates are improved with haptic cues over visual cues, suggesting motor learning rather than perceptual learning.

2. Design and Control of Backdriveable Actuators

- Shows parallels between SEA and fluidic actuators, including options for control.
- Designs and demonstrates a new actuator that minimizes storage of elastic energy and harnesses singularity to advantage
- Develops controllers that promote backdriveability

3. Computational Model of Human Motor Control

- Proposes a computational model that the relationship between the motor command and its responses in place of internal models
- Demonstrates the reproducibility of the proposed model in the human's fast movements

5.2 Future Work

The best robot is the human. Robots have been being developed to mimic the human.It has been continuing and endlessly needs to continue to discover the secret of the human's musculoskeletal system, sensory system, and control system. Through human-like robots, exchange of power and information is maximized This is entirely for recovering and promoting the human's motor skill, motor function and well-being.

BIBLIOGRAPHY

BIBLIOGRAPHY

[1] E. L. Abrahamse, R. H. Van Der Lubbe, and W. B. Verwey, "Asymmetrical learning between a tactile and visual serial rt task," *The Quarterly Journal of Experimental Psychology*, vol. 61, no. 2, pp. 210–217, 2008.

[2] A. Albu-Schäffer, C. Ott, and G. Hirzinger, "A unified passivity-based control framework for position, torque and impedance control of flexible joint robots," *The International Journal of Robotics Research*, vol. 26, no. 1, pp. 23–39, 2007.

[3] T. R. Armstrong, "Training for the production of memorized movement patterns," 1970.

[4] R. S. Bapi, K. Doya, and A. M. Harner, "Evidence for effector independent and dependent representations and their differential time course of acquisition during motor sequence learning," *Experimental Brain Research*, vol. 132, no. 2, pp. 149–162, 2000.

[5] A. J. Bastian, "Learning to predict the future: the cerebellum adapts feedforward movement control," *Current opinion in neurobiology*, vol. 16, no. 6, pp. 645–649, 2006.

[6] A. Bellomo and G. Inbar, "Examination of the λ equilibrium point hypothesis when applied to single degree of freedom movements performed with different inertial loads," *Biological cybernetics*, vol. 76, no. 1, pp. 63–72, 1997.

[7] N. Bhushan and R. Shadmehr, "Computational nature of human adaptive control during learning of reaching movements in force fields," *Biological cybernetics*, vol. 81, no. 1, pp. 39–60, 1999.

[8] A. Bischoff-Grethe, K. M. Goedert, D. T. Willingham, and S. T. Grafton, "Neural substrates of response-based sequence learning using fmri," *Journal of cognitive neuroscience*, vol. 16, no. 1, pp. 127–138, 2004.

[9] J. Bishop-Moser, G. Krishnan, C. Kim, and S. Kota, "Design of soft robotic actuators using fluid-filled fiber-reinforced elastomeric enclosures in parallel combinations," in *Intelligent Robots and Systems (IROS), 2012 IEEE/RSJ International Conference on*. IEEE, 2012, pp. 4264–4269.

[10] H. Brunner and R. M. Richardson, "Effects of keyboard design and typing skill on user keyboard preferences and throughput performance," in *Proceedings of the Human Factors and Ergonomics Society Annual Meeting*, vol. 28, no. 3. SAGE Publications, 1984, pp. 267–271.

[11] E. Burdet, K. P. Tee, I. Mareels, T. E. Milner, C.-M. Chew, D. W. Franklin, R. Osu, and M. Kawato, "Stability and motor adaptation in human arm movements," *Biological cybernetics*, vol. 94, no. 1, pp. 20–32, 2006.

[12] P. H. Chang and J. W. Jeong, "Enhanced operational space formulation for multiple tasks by using time-delay estimation," *Robotics, IEEE Transactions on*, vol. 28, no. 4, pp. 773–786, 2012.

[13] Z. Chen, N. Y. Lii, T. Wimboeck, S. Fan, M. Jin, C. H. Borst, and H. Liu, "Experimental study on impedance control for the five-finger dexterous robot hand dlr-hit ii," in *Intelligent Robots and Systems (IROS), 2010 IEEE/RSJ International Conference on*. IEEE, 2010, pp. 5867–5874.

[14] G. R. Cho, P. H. Chang, S. H. Park, and M. Jin, "Robust tracking under nonlinear friction using time-delay control with internal model," *Control Systems Technology, IEEE Transactions on*, vol. 17, no. 6, pp. 1406–1414, 2009.

[15] K.-S. Choi and K.-H. Lo, "A hand rehabilitation system with force feedback for children with cerebral palsy: two case studies," *Disability and rehabilitation*, vol. 33, no. 17-18, pp. 1704–1714, 2011.

[16] A. Cleeremans, *Mechanisms of implicit learning: Connectionist models of sequence processing*. MIT press, 1993.

[17] A. Cohen and R. Shoup, "Perceptual dimensional constraints in response selection processes," *Cognitive Psychology*, vol. 32, no. 2, pp. 128–181, 1997.

[18] N. Colonnese, S. M. Sketch, and A. M. Okamura, "Closed-loop stiffness and damping accuracy of impedance-type haptic displays," in *Haptics Symposium (HAPTICS), 2014 IEEE*. IEEE, 2014, pp. 97–102.

[19] R. Connelly, I. Sabitov, and A. Walz, "The bellows conjecture," *Beitr. Algebra Geom*, vol. 38, no. 1, pp. 1–10, 1997.

[20] L. M. Crespo and D. J. Reinkensmeyer, "Haptic guidance can enhance motor learning of a steering task," *Journal of motor behavior*, vol. 40, no. 6, pp. 545–557, 2008.

[21] M. H. de Lussanet, J. B. Smeets, and E. Brenner, "Relative damping improves linear mass-spring models of goal-directed movements," *Human movement science*, vol. 21, no. 1, pp. 85–100, 2002.

[22] N. Deroost, I. Zeeuws, and E. Soetens, "Effector-dependent and response location learning of probabilistic sequences in serial reaction time tasks," *Experimental Brain Research*, vol. 171, no. 4, pp. 469–480, 2006.

[23] M. Desmurget and S. Grafton, "Forward modeling allows feedback control for fast reaching movements," *Trends in cognitive sciences*, vol. 4, no. 11, pp. 423–431, 2000.

[24] A. Destrebecqz and A. Cleeremans, "Can sequence learning be implicit? new evidence with the process dissociation procedure," *Psychonomic bulletin & review*, vol. 8, no. 2, pp. 343–350, 2001.

[25] J. B. Dingwell, C. D. Mah, and F. A. Mussa-Ivaldi, "Manipulating objects with internal degrees of freedom: evidence for model-based control," *Journal of Neurophysiology*, vol. 88, no. 1, pp. 222–235, 2002.

[26] L. M. S. do Amaral, B. Jardim, and A. A. G. Siqueira, "Robust force and impedance control of series elastic actuators," 2012.

[27] O. Donchin, J. T. Francis, and R. Shadmehr, "Quantifying generalization from trial-by-trial behavior of adaptive systems that learn with basis functions: theory and experiments in human motor control," *The Journal of neuroscience*, vol. 23, no. 27, pp. 9032–9045, 2003.

[28] P. Engel, *Folding the Universe: Origami from Angelfish to Zen*. Vintage Books, 1989.

[29] J. Falmagne, S. P. Cohen, and A. Dwivedi, "Two-choice reactions as an ordered memory scanning process," *Attention and performance V*, pp. 296–344, 1975.

[30] A. G. Feldman and M. F. Levin, "The origin and use of positional frames of reference in motor control," *Behavioral and Brain Sciences*, vol. 18, no. 04, pp. 723–744, 1995.

[31] D. W. Fendrich, A. F. Healy, and L. E. Bourne, "Long-term repetition effects for motoric and perceptual procedures." *Journal of Experimental Psychology: Learning, Memory, and Cognition*, vol. 17, no. 1, p. 137, 1991.

[32] D. Feygin, M. Keehner, and F. Tendick, "Haptic guidance: Experimental evaluation of a haptic training method for a perceptual motor skill," in *Haptic Interfaces for Virtual Environment and Teleoperator Systems, 2002. HAPTICS 2002. Proceedings. 10th Symposium on*. IEEE, 2002, pp. 40–47.

[33] P. M. Fitts and M. I. Posner, "Human performance." 1967.

[34] T. Flash and N. Hogan, "The coordination of arm movements: an experimentally confirmed mathematical model," *The journal of Neuroscience*, vol. 5, no. 7, pp. 1688–1703, 1985.

[35] D. Fredlund, "Density and compressibility characteristics of air-water mixtures," *Canadian Geotechnical Journal*, vol. 13, no. 4, pp. 386–396, 1976.

[36] E. Fridman and U. Shaked, "An improved stabilization method for linear time-delay systems," *Automatic Control, IEEE Transactions on*, vol. 47, no. 11, pp. 1931–1937, 2002.

[37] K. Friston, "What is optimal about motor control?" *Neuron*, vol. 72, no. 3, pp. 488–498, 2011.

[38] R. Ghazali, Y. Sam, M. Rahmat, W. Hashim, and Z. Zulfatman, "Sliding mode control with pid sliding surface of an electro-hydraulic servo system for position tracking control," *Australian Journal of Basic and Applied Sciences*, vol. 4, no. 10, pp. 4749–4759, 2010.

[39] F. Gheysen, W. Gevers, E. De Schutter, H. Van Waelvelde, and W. Fias, "Disentangling perceptual from motor implicit sequence learning with a serial color-matching task," *Experimental brain research*, vol. 197, no. 2, pp. 163–174, 2009.

[40] R. B. Gillespie, M. OModhrain, P. Tang, D. Zaretzky, and C. Pham, "The virtual teacher," in *Proceedings of the ASME Dynamic Systems and Control Division*, vol. 64. American Society of Mechanical Engineers, 1998, pp. 171–178.

[41] H. Gomi and M. Kawato, "Equilibrium-point control hypothesis examined by measured arm stiffness during multijoint movement," *Science*, vol. 272, no. 5258, pp. 117–120, 1996.

[42] T. Goschke and A. Bolte, "On the modularity of implicit sequence learning: Independent acquisition of spatial, symbolic, and manual sequences," *Cognitive psychology*, vol. 65, no. 2, pp. 284–320, 2012.

[43] G. Grindlay, "Haptic guidance benefits musical motor learning," in *Haptic interfaces for virtual environment and teleoperator systems, 2008. haptics 2008. symposium on*. IEEE, 2008, pp. 397–404.

[44] V. Gritsenko, S. Yakovenko, and J. F. Kalaska, "Integration of predictive feedforward and sensory feedback signals for online control of visually guided movement," *Journal of Neurophysiology*, vol. 102, no. 2, pp. 914–930, 2009.

[45] E. Hallgató, D. Győri-Dani, J. Pekár, K. Janacsek, and D. Nemeth, "The differential consolidation of perceptual and motor learning in skill acquisition," *Cortex*, vol. 49, no. 4, pp. 1073–1081, 2013.

[46] D. K. Han and P.-h. Chang, "Robust tracking of robot manipulator with nonlinear friction using time delay control with gradient estimator," *Journal of mechanical science and technology*, vol. 24, no. 8, pp. 1743–1752, 2010.

[47] O. Hikosaka, H. Nakahara, M. K. Rand, K. Sakai, X. Lu, K. Nakamura, S. Miyachi, and K. Doya, "Parallel neural networks for learning sequential procedures," *Trends in neurosciences*, vol. 22, no. 10, pp. 464–471, 1999.

[48] J. Hoffmann, C. Martin, and A. Schilling, "Unique transitions between stimuli and responses in srt tasks: Evidence for the primacy of response predictions," *Psychological Research*, vol. 67, no. 3, pp. 160–173, 2003.

[49] J. Hoffmann and A. Sebald, "Reiz-und reaktionsmuster in seriellen wahlreaktionen." *Zeitschrift fÃ1/4r Experimentelle Psychologie*, 1996.

[50] N. Hogan, "Impedance control: An approach to manipulation part i: Theory; part ii: Implementation; part iii: Applications," *Journal of dynamic systems, measurement, and control*, vol. 107, no. 1, pp. 1–24, 1985.

[51] J. H. Howard, S. A. Mutter, and D. V. Howard, "Serial pattern learning by event observation." *Journal of Experimental Psychology: Learning, Memory, and Cognition*, vol. 18, no. 5, p. 1029, 1992.

[52] T. S. Hsia, T. Lasky, and Z. Guo, "Robust independent joint controller design for industrial robot manipulators," *Industrial Electronics, IEEE Transactions on*, vol. 38, no. 1, pp. 21–25, 1991.

[53] E. J. Hwang, M. A. Smith, and R. Shadmehr, "Adaptation and generalization in acceleration-dependent force fields," *Experimental brain research*, vol. 169, no. 4, pp. 496–506, 2006.

[54] R. J. Jagacinski and J. M. Flach, *Control theory for humans: Quantitative approaches to modeling performance*. CRC Press, 2002.

[55] M. Jin, Y. Jin, P. H. Chang, and C. Choi, "High-accuracy trajectory tracking of industrial robot manipulators using time delay estimation and terminal sliding mode," in *Industrial Electronics, 2009. IECON'09. 35th Annual Conference of IEEE*. IEEE, 2009, pp. 3095–3099.

[56] M. Jin, S. H. Kang, and P. H. Chang, "Robust compliant motion control of robot with nonlinear friction using time-delay estimation," *Industrial Electronics, IEEE Transactions on*, vol. 55, no. 1, pp. 258–269, 2008.

[57] S. Jung, T. Hsia, and R. G. Bonitz, "Force tracking impedance control of robot manipulators under unknown environment," *Control Systems Technology, IEEE Transactions on*, vol. 12, no. 3, pp. 474–483, 2004.

[58] L. E. Kahn, P. S. Lum, W. Z. Rymer, and D. J. Reinkensmeyer, "Robot-assisted movement training for the stroke-impaired arm: Does it matter what the robot does?" *Journal of rehabilitation research and development*, vol. 43, no. 5, p. 619, 2006.

[59] J. Kalaska, D. Cohen, M. Prud'Homme, and M. Hyde, "Parietal area 5 neuronal activity encodes movement kinematics, not movement dynamics," *Experimental Brain Research*, vol. 80, no. 2, pp. 351–364, 1990.

[60] S. W. Keele, R. Ivry, U. Mayr, E. Hazeltine, and H. Heuer, "The cognitive and neural architecture of sequence representation." *Psychological review*, vol. 110, no. 2, p. 316, 2003.

[61] D. Kim, "Compliant motion control for a compliant rehabilitation system," in *Rehabilitation Robotics (ICORR), 2015 IEEE International Conference on*. IEEE, 2015, pp. 422–427.

[62] D. Kim, R. B. Gillespie, and P. H. Chang, "Simple, robust control and synchronization of the lorenz system," *Nonlinear Dynamics*, pp. 1–10, 2013.

[63] S. Kim, C. Laschi, and B. Trimmer, "Soft robotics: a bioinspired evolution in robotics," *Trends in biotechnology*, vol. 31, no. 5, pp. 287–294, 2013.

[64] D. A. Kistemaker, A. K. J. Van Soest, and M. F. Bobbert, "Is equilibrium point control feasible for fast goal-directed single-joint movements?" *Journal of Neurophysiology*, vol. 95, no. 5, pp. 2898–2912, 2006.

[65] J. Kluzik, J. Diedrichsen, R. Shadmehr, and A. J. Bastian, "Reach adaptation: what determines whether we learn an internal model of the tool or adapt the model of our arm?" *Journal of neurophysiology*, vol. 100, no. 3, pp. 1455–1464, 2008.

[66] Y. Koike and M. Kawato, "Estimation of dynamic joint torques and trajectory formation from surface electromyography signals using a neural network model," *Biological cybernetics*, vol. 73, no. 4, pp. 291–300, 1995.

[67] S. Kota, "Shape-shifting things to come," *Scientific American*, vol. 310, no. 5, pp. 58–65, 2014.

[68] J. W. Krakauer, M.-F. Ghilardi, and C. Ghez, "Independent learning of internal models for kinematic and dynamic control of reaching," *Nature neuroscience*, vol. 2, no. 11, pp. 1026–1031, 1999.

[69] F. Lacquaniti and J. Soechting, "Emg responses to load perturbations of the upper limb: effect of dynamic coupling between shoulder and elbow motion," *Experimental brain research*, vol. 61, no. 3, pp. 482–496, 1986.

[70] M. Latash and G. Gottlieb, "Reconstruction of shifting elbow joint compliant characteristics during fast and slow movements," *Neuroscience*, vol. 43, no. 2, pp. 697–712, 1991.

[71] J. Lee and S. Choi, "Effects of haptic guidance and disturbance on motor learning: Potential advantage of haptic disturbance," in *Haptics Symposium, 2010 IEEE*. IEEE, 2010, pp. 335–342.

[72] J. Lee, P. Chang, and R. S. Jamisola, "Relative impedance control for dual-arm robots performing asymmetric bimanual tasks," *Industrial Electronics, IEEE Transactions on*, 2013.

[73] A. Levant, "Higher-order sliding modes, differentiation and output-feedback control," *International journal of Control*, vol. 76, no. 9-10, pp. 924–941, 2003.

[74] J. Liu, S. Cramer, and D. Reinkensmeyer, "Learning to perform a new movement with robotic assistance: comparison of haptic guidance and visual demonstration," *Journal of neuroengineering and rehabilitation*, vol. 3, p. 20, 2006.

[75] R. V. Martinez, C. R. Fish, X. Chen, and G. M. Whitesides, "Elastomeric origami: Programmable paper-elastomer composites as pneumatic actuators," *Advanced Functional Materials*, vol. 22, no. 7, pp. 1376–1384, 2012.

[76] U. Mayr, "Spatial attention and implicit sequence learning: Evidence for independent learning of spatial and nonspatial sequences." *Journal of Experimental Psychology: Learning, Memory, and Cognition*, vol. 22, no. 2, p. 350, 1996.

[77] J. McIntyre and E. Bizzi, "Servo hypotheses for the biological control of movement," *Journal of motor behavior*, vol. 25, no. 3, pp. 193–202, 1993.

[78] J. S. Mehling, J. E. Colgate, and M. A. Peshkin, "Increasing the impedance range of a haptic display by adding electrical damping," in *Eurohaptics Conference, 2005 and Symposium on Haptic Interfaces for Virtual Environment and Teleoperator Systems, 2005. World Haptics 2005. First Joint.* IEEE, 2005, pp. 257–262.

[79] R. Miall, D. Weir, D. M. Wolpert, and J. Stein, "Is the cerebellum a smith predictor?" *Journal of motor behavior*, vol. 25, no. 3, pp. 203–216, 1993.

[80] D. Mitrovic, S. Klanke, and S. Vijayakumar, "Learning impedance control of antagonistic systems based on stochastic optimization principles," *The International Journal of Robotics Research*, vol. 30, no. 5, pp. 556–573, 2011.

[81] R. Morales, F. J. Badesa, N. García-Aracil, J. M. Sabater, and C. Pérez-Vidal, "Pneumatic robotic systems for upper limb rehabilitation," *Medical & biological engineering & computing*, vol. 49, no. 10, pp. 1145–1156, 2011.

[82] B. Mosadegh, P. Polygerinos, C. Keplinger, S. Wennstedt, R. F. Shepherd, U. Gupta, J. Shim, K. Bertoldi, C. J. Walsh, and G. M. Whitesides, "Pneumatic networks for soft robotics that actuate rapidly," *Advanced Functional Materials*, vol. 24, no. 15, pp. 2163–2170, 2014.

[83] D. Nattkemper and W. Prinz, "Stimulus and response anticipation in a serial reaction task," *Psychological Research*, vol. 60, no. 1-2, pp. 98–112, 1997.

[84] D. Nemeth, E. Hallgató, K. Janacsek, T. Sándor, and Z. Londe, "Perceptual and motor factors of implicit skill learning," *Neuroreport*, vol. 20, no. 18, pp. 1654–1658, 2009.

[85] Y. Nishioka, M. Uesu, H. Tsuboi, and S. Kawamura, "Proposal of an extremely lightweight soft actuator using plastic films with a pleated structure," in *Mechatronics and Machine Vision in Practice (M2VIP), 2012 19th International Conference*. IEEE, 2012, pp. 474–479.

[86] M. J. Nissen and P. Bullemer, "Attentional requirements of learning: Evidence from performance measures," *Cognitive psychology*, vol. 19, no. 1, pp. 1–32, 1987.

[87] M. K. O'Malley and A. Gupta, "Passive and active assistance for human performance of a simulated underactuated dynamic task," in *Haptic Interfaces for Virtual Environment and Teleoperator Systems, 2003. HAPTICS 2003. Proceedings. 11th Symposium on*. IEEE, 2003, pp. 348–355.

[88] J.-H. Park and C. H. Shea, "Sequence learning: Response structure and effector transfer," *The Quarterly Journal of Experimental Psychology Section A*, vol. 58, no. 3, pp. 387–419, 2005.

[89] P. Polygerinos, Z. Wang, K. C. Galloway, R. J. Wood, and C. J. Walsh, "Soft robotic glove for combined assistance and at-home rehabilitation," *Robotics and Autonomous Systems*, 2014.

[90] F. Popescu, J. M. Hidler, and W. Z. Rymer, "Elbow impedance during goal-directed movements," *Experimental brain research*, vol. 152, no. 1, pp. 17–28, 2003.

[91] G. A. Pratt and M. M. Williamson, "Series elastic actuators," in *Intelligent Robots and Systems 95.'Human Robot Interaction and Cooperative Robots', Proceedings. 1995 IEEE/RSJ International Conference on*, vol. 1. IEEE, 1995, pp. 399–406.

[92] G. A. Pratt, P. Willisson, C. Bolton, and A. Hofman, "Late motor processing in low-impedance robots: Impedance control of series-elastic actuators," in *American Control Conference, 2004. Proceedings of the 2004*, vol. 4. IEEE, 2004, pp. 3245–3251.

[93] A. S. Reber, "Implicit learning and tacit knowledge." *Journal of experimental psychology: General*, vol. 118, no. 3, p. 219, 1989.

[94] J. Reed and P. Johnson, "Assessing implicit learning with indirect tests: determining what is learned about sequence structure." *Journal of Experimental Psychology: Learning, Memory, and Cognition*, vol. 20, no. 3, p. 585, 1994.

[95] G. Remillard, "Pure perceptual-based sequence learning." *Journal of Experimental Psychology: Learning, Memory, and Cognition*, vol. 29, no. 4, p. 581, 2003.

[96] D. W. Robinson, "Design and analysis of series elasticity in closed-loop actuator force control," Ph.D. dissertation, Massachusetts Institute of Technology, 2000.

[97] L. B. Rosenberg, "The use of virtual fixtures as perceptual overlays to enhance operator performance in remote environments." DTIC Document, Tech. Rep., 1992.

[98] J. Rothwell, M. Traub, and C. Marsden, "Automatic and voluntaryresponses compensating for disturbances of human thumb movements," *Brain research*, vol. 248, no. 1, pp. 33–41, 1982.

[99] S. Schaal, "Arm and hand movement control," *The handbook of brain theory and neural networks,*, pp. 110–113, 2002.

[100] R. A. Scheidt, M. A. Conditt, E. L. Secco, and F. A. Mussa-Ivaldi, "Interaction of visual and proprioceptive feedback during adaptation of human reaching movements," *Journal of Neurophysiology*, vol. 93, no. 6, pp. 3200–3213, 2005.

[101] R. A. Scheidt, J. B. Dingwell, and F. A. Mussa-Ivaldi, "Learning to move amid uncertainty," *Journal of neurophysiology*, vol. 86, no. 2, pp. 971–985, 2001.

[102] N. Schweighofer, M. A. Arbib, and M. Kawato, "Role of the cerebellum in reaching movements in humans. i. distributed inverse dynamics control," *European Journal of Neuroscience*, vol. 10, no. 1, pp. 86–94, 1998.

[103] R. Seidler, P. Tuite, and J. Ashe, "Selective impairments in implicit learning in parkinson's disease," *Brain research*, vol. 1137, pp. 104–110, 2007.

[104] R. Shadmehr and J. W. Krakauer, "A computational neuroanatomy for motor control," *Experimental Brain Research*, vol. 185, no. 3, pp. 359–381, 2008.

[105] R. Shadmehr and F. A. Mussa-Ivaldi, "Adaptive representation of dynamics during learning of a motor task," *The Journal of Neuroscience*, vol. 14, no. 5, pp. 3208–3224, 1994.

[106] O. J. Smith, "A controller to overcome dead time," *ISA Journal*, vol. 6, no. 2, pp. 28–33, 1959.

[107] Y. S. Song, Y. Sun, R. Van Den Brand, J. Von Zitzewitz, S. Micera, G. Courtine, and J. Paik, "Soft robot for gait rehabilitation of spinalized rodents," in *Intelligent Robots and Systems (IROS), 2013 IEEE/RSJ International Conference on.* Ieee, 2013, pp. 971–976.

[108] M. W. Spong, S. Hutchinson, and M. Vidyasagar, *Robot modeling and control*. John Wiley & Sons New York, First Edition.

[109] K. A. Thoroughman and R. Shadmehr, "Electromyographic correlates of learning an internal model of reaching movements," *The Journal of Neuroscience*, vol. 19, no. 19, pp. 8573–8588, 1999.

[110] ——, "Learning of action through adaptive combination of motor primitives," *Nature*, vol. 407, no. 6805, pp. 742–747, 2000.

[111] E. Todorov and M. I. Jordan, "Optimal feedback control as a theory of motor coordination," *Nature neuroscience*, vol. 5, no. 11, pp. 1226–1235, 2002.

[112] S. Tsutsui and K. Imanaka, "Effect of manual guidance on acquiring a new bimanual coordination pattern," *Research quarterly for exercise and sport*, vol. 74, no. 1, pp. 104–109, 2003.

[113] H. Vallery, J. Veneman, E. Van Asseldonk, R. Ekkelenkamp, M. Buss, and H. Van Der Kooij, "Compliant actuation of rehabilitation robots," *Robotics & Automation Magazine, IEEE*, vol. 15, no. 3, pp. 60–69, 2008.

[114] P. L. Van Kan, A. R. Gibson, and J. C. Houk, "Movement-related inputs to intermediate cerebellum of the monkey," *Journal of neurophysiology*, vol. 69, no. 1, pp. 74–94, 1993.

[115] P. L. Van Kan, J. C. Houk, and A. R. Gibson, "Output organization of intermediate cerebellum of the monkey," *Journal of neurophysiology*, vol. 69, no. 1, pp. 57–73, 1993.

[116] W. B. Verwey and B. A. Clegg, "Effector dependent sequence learning in the serial rt task," *Psychological research*, vol. 69, no. 4, pp. 242–251, 2005.

[117] W. B. Verwey and D. L. Wright, "Effector-independent and effector-dependent learning in the discrete sequence production task," *Psychological Research*, vol. 68, no. 1, pp. 64–70, 2004.

[118] D. B. Willingham, "Implicit motor sequence learning is not purely perceptual," *Memory & Cognition*, vol. 27, no. 3, pp. 561–572, 1999.

[119] D. B. Willingham, M. J. Nissen, and P. Bullemer, "On the development of procedural knowledge." *Journal of experimental psychology: learning, memory, and cognition*, vol. 15, no. 6, p. 1047, 1989.

[120] D. B. Willingham, L. A. Wells, J. M. Farrell, and M. E. Stemwedel, "Implicit motor sequence learning is represented in response locations," *Memory & Cognition*, vol. 28, no. 3, pp. 366–375, 2000.

[121] A. G. Witney, P. Vetter, and D. M. Wolpert, "The influence of previous experience on predictive motor control," *Neuroreport*, vol. 12, no. 4, pp. 649–653, 2001.

[122] J. K. Witt and D. T. Willingham, "Evidence for separate representations for action and location in implicit motor sequencing," *Psychonomic bulletin & review*, vol. 13, no. 5, pp. 902–907, 2006.

[123] D. M. Wolpert and Z. Ghahramani, "Computational principles of movement neuroscience," *nature neuroscience*, vol. 3, pp. 1212–1217, 2000.

[124] D. M. Wolpert, R. C. Miall, and M. Kawato, "Internal models in the cerebellum," *Trends in cognitive sciences*, vol. 2, no. 9, pp. 338–347, 1998.

[125] K. Youcef-Toumi and O. Ito, "A time delay controller for systems with unknown dynamics," *Journal of dynamic systems, measurement, and control*, vol. 112, no. 1, pp. 133–142, 1990.

[126] P. Zhuang, C. Toro, J. Grafman, P. Manganotti, L. Leocani, and M. Hallett, "Event-related desynchronization (erd) in the alpha frequency during development of implicit and explicit learning," *Electroencephalography and clinical neurophysiology*, vol. 102, no. 4, pp. 374–381, 1997.